INFORMATION TO USERS

This manuscript has been reproduced from the microfilm master. UMI films the text directly from the original or copy submitted. Thus, some thesis and dissertation copies are in typewriter face, while others may be from any type of computer printer.

The quality of this reproduction is dependent upon the quality of the copy submitted. Broken or indistinct print, colored or poor quality illustrations and photographs, print bleedthrough, substandard margins, and improper alignment can adversely affect reproduction.

In the unlikely event that the author did not send UMI a complete manuscript and there are missing pages, these will be noted. Also, if unauthorized copyright material had to be removed, a note will indicate the deletion.

Oversize materials (e.g., maps, drawings, charts) are reproduced by sectioning the original, beginning at the upper left-hand corner and continuing from left to right in equal sections with small overlaps. Each original is also photographed in one exposure and is included in reduced form at the back of the book.

Photographs included in the original manuscript have been reproduced xerographically in this copy. Higher quality 6" x 9" black and white photographic prints are available for any photographs or illustrations appearing in this copy for an additional charge. Contact UMI directly to order.

UMI

A Bell & Howell Information Company
300 North Zeeb Road, Ann Arbor MI 48106-1346 USA
313/761-4700 800/521-0600

3D UNDERWATER MONOCULAR MACHINE VISION FROM 2D IMAGES IN AN ATTENUATING MEDIUM

by

Charles James Randell
B. Eng., Lakehead University, 1988
M. A. Sc., University of Victoria, 1992

A Dissertation Submitted in Partial Fulfillment of the
Requirements for the Degree of

DOCTOR OF PHILOSOPHY

in the Department of Electrical and Computer Engineering

We accept this dissertation as conforming
to the required standard

Dr. J. S. Collins, Supervisor (Dept. of Electrical and Computer Engineering)

Dr. W-S. Lu, Co-Supervisor (Dept. of Electrical and Computer Engineering)

Dr. R. L. Kirlin, Departmental Member (Dept. of Electrical and Computer Engineering)

Dr. M. Nahon, Outside Member (Dept. of Mechanical Engineering)

Dr. R. Gosine, External Examiner (Faculty of Engineering and Applied Science, Memorial University of Newfoundland)

Supervisors: Dr. J. S. Collins
Dr. W-S. Lu

ABSTRACT

This dissertation presents a novel underwater machine vision technique which uses the optical properties of water to extract range information from colour images. By exploiting the fact that the attenuation of light in water is a function of frequency, an intensity–range transformation is developed and implemented to provide monocular vision systems with a three-dimensional scene reconstruction capability. The technique can also be used with images that have no salient, contrasting features and there are no restrictions on surface shapes.

From a generalized reflectance map based on the optical properties of water, the closed form intensity–range transformation is derived to convert intensity images from various spectral bands into a range map wherein the value of each "pixel" is the range to the imaged surface. The technique is computationally efficient enough to be performed in real time and does not require specialized illumination or similar restrictive conditions. A calibration procedure is developed which enables the transformation to be practically implemented. An alternate approach to estimating range from multispectral data based on expanding the medium's transfer function and using these terms as elements in sensitivity vectors is also presented and analyzed.

Mathematical analysis of the intensity–range transformation and associated developments is provided in terms of its performance in noise and sensitivity to various system parameters. Its performance as a function of light scattering is studied with the aid of computer simulation. Results from transforming actual underwater images are also presented. The results of this analysis and the demonstrated performance of the intensity–range transformation endorse it as a practical enhancement to underwater machine vision systems.

Examiners:

Dr. J. S. Collins, Supervisor (Dept. of Electrical and Computer Engineering)

Dr. W-S. Lu, Co-Supervisor (Dept. of Electrical and Computer Engineering)

Dr. R. L. Kirlin, Departmental Member (Dept. of Electrical and Computer Engineering)

Dr. M. Nahon, Outside Member (Dept. of Mechanical Engineering)

Dr. R. Gosine, External Examiner (Faculty of Engineering and Applied Science, Memorial University of Newfoundland)

Contents

List of Tables

List of Figures

ACKNOWLEDGMENTS

I begin this section with an apology for not explicitly naming the many, many people who have supported and assisted me in the endeavor represented by this dissertation. I am indebted to many.

I must begin with my loving and supportive wife, Deborah who believed not only that I *could* do this, but also that I *should* do it. Any motivation, discipline or sacrifice that went into completing this work was given (happily) at least as much by her as by me. Her support never faded, her faith never faltered. We are partners in this degree.

I am exceedingly indebted to Dr. Jack Clark and C-CORE both for revealing to me, my capacity to attain a Ph.D. and for providing the support to make it possible. Without Dr. Clark informing me that I could do it, I may never have entered university the first time. His continued support and encouragement has now guided me through three degrees. I am extremely fortunate to know him and to be part of C-CORE; my very deep gratitude cannot be understated. I am also thankful to Ms. Judith Whittick and others at C-CORE for their help and encouragement.

My Supervisor, Dr. James Collins was exceptional. In addition to providing insight and guidance, his patience and persistence came in just the right proportions to keep me going and see this work to successful completion. For the numerous times that both he and his wife, Dr. Faith Collins went above and beyond "the call of duty" to help me in completing this work, I am extremely grateful.

I also acknowledge with thanks the support of International Submarine Engineering Research Ltd., and the insights provided by Mr. James Ferguson and Mr. Landy Shupe. Finally, I wish to thank the Government of Newfoundland and Labrador, and the Government of British Columbia for financial support.

To Deborah:
again with much love and thanks
"If you believe ..."

Chapter 1

Introduction

1.0 Introduction

With 70% of our earth covered by water, there is in many sectors a growing trend to develop the wealth of resources locked beneath the surface of the world's oceans. These resources are not restricted merely to commercially valuable commodities such as precious metals, food, and hydrocarbon deposits; there is a plethora of information and knowledge on biological and geophysical processes to be gained from studying what lies within the oceans. The ability of marine species to exist in this environment, particularly at great depths, in toxic regions, and in very cold areas is providing scientists with insights that may be adapted for human use. Potential geophysical knowledge ranges from clues to the origin and evolution of the planet, which may be gleaned from studies of tectonic spreading centres, to the earth's current health and prognosis for the future which may be forecast from the ocean's cause and effect response to climate change [1]. The ability to probe and observe below the ocean's surface is also of strategic military importance and drives much of the subsea scientific and engineering research in the world [2]. It follows naturally that sensor development for subsea monitoring and intervention is also an active research area.

Presented in this dissertation is a new underwater machine vision technique which exploits the optical properties of water to extract range information from colour images. Light is attenuated by water, hence light intensity is inversely proportional to distance traveled. Furthermore, attenuation of light underwater is a function of frequency. In viewing underwater scenes at various ranges one will note that light in the "red" region of the colour spectrum is usually lost first, followed usually by yellows then violets, with blue or green light being attenuated last.[1] In this thesis we exploit that characteristic and effectively work backwards. Newer CCD cameras are available with three separate CCD arrays to measure light radiance received in three spectral bands. Using these data it is possible to determine how far the light has traveled from the source to the surface(s) being imaged and back to the camera. This intensity-to-range transformation provides three dimensional mapping of the environment or objects of interest. A method of optical ranging where attenuation information substitutes for binocular information (as in animal vision) has several advantages. For example, it does not rely on contrasting features within the image as is the case with stereo and optical flow type approaches. This is important since many underwater scenes are devoid of such features. As will be demonstrated, this approach is insensitive to geometrical parameters such as angles of incidence and shapes of objects, and it provides a closed form solution for range that can be computed in real-time.

In an iterative process, increased observation and understanding of the world's oceans promotes safer (both to humans and the environment) and efficient exploitation of its resources. Human access to the subsea is risky and expensive so we prefer to rely on remotely sensed data or *in situ* sensors and their associated delivery platforms. The growing trend toward subsea exploration and exploitation is assisted, at least in part by

---

[1] As discussed in Chapter 2, this order of attenuation changes depending on water composition and suspended particulate.

ever more competent vehicles with increasingly capable sensor suites. "Subsea technology will be critical to (offshore) oil and gas developments ... the next development project will likely see the introduction of subsea technology in a major way." [3] Subsea robotic vehicles can "stand alone" to monitor and acquire data, or they can take investigators via tele-presence to probe deeper, for longer duration, and beneath ice covers without subjecting them to the extreme hazards of that environment. Subsea robotic vehicles range from remotely operated vehicles (ROVs) which are usually tethered with a human "in the loop" controlling the vehicle directly, to autonomous underwater vehicles (AUVs) which are highly competent platforms capable of independently making decisions toward achievement of a specified goal. The results of this thesis are initially intended for application to subsea robotic vehicles.

Many experts agree that a key area for research and development to increase the applicability of underwater vehicles, and our subsea capabilities in general, is underwater sensing [4, 5]. The underwater domain is a complex and challenging environment and as our understanding of subsea processes broadens, our questions become more subtle, and our desires more ambitious – the limitations of "traditional" sensors become more apparent. It is doubtful that any single sensor, or even single sensing mode (e.g. acoustic, optic, tactile) will become the "standard" for subsea activity. A number of integrated sensors for different ranges and resolutions are required [6]. However, accurate, high resolution data is obtained most readily using imaging techniques [7] based on optical cameras [8, 9].

Still or video cameras are a standard fixture on or in practically all subsea vehicles. One company even markets a Hyball™, or what has become known in the industry as the "swimming eyeball". Despite the opacity and scattering encountered in the subsea environment, optical sensing provides, in various ways unique and desirable data.

- Colour images contain surface hue, and texture information not available from any other sensor;

- Optical images are extremely high resolution and can be acquired at rates exceeding 200 M bps thereby facilitating reactions requiring precise, real-time data;
- A wide variety of CCD cameras are readily available and relatively inexpensive. A mid-range 3-chip RGB CCD camera and an associated full video rate RGB frame grabber can be purchased for less than $10,000. This combination provides over 750,000 individual optical sensors and associated data acquisition hardware.
- Passive, near range sensing makes optical sensors the natural choice for a variety of activities.

Though not limited to the following application, the work in this dissertation is directed primarily towards enhancing subsea optical systems or machine vision for two modes of application: for monitoring tasks including inspection, surveillance, mapping, and 3D modelling; and for robotic tasks including navigation, docking, manipulation, and obstacle detection and avoidance.

Understandably, underwater optical imaging has been a very active research subject and numerous advances have been made [10, 11]. The use of automated machine vision has provided a dramatic enhancement to close range subsea capabilities and is expected to be a vital part of next generation teleoperated and autonomous underwater vehicle systems [12]. A review of developments in underwater imaging and other related technologies is provided in the next section.

1.1 Underwater Optical Imaging Technologies

Vision is our most complex and arguably most powerful sensing mechanism. It has evolved to enable us to efficiently function in unstructured environments and it is a logical extension therefore, that we work to imbue robotic devices with this most powerful sense. One "frame" of optical data captured in less than 0.1 seconds can provide information that, if it is available at all, might take minutes or even hours to acquire by other means. Machine vision, as defined by the Machine Vision Association

of the Society of Manufacturing Engineers is *the use of devices for optical non-contact sensing to automatically receive and interpret an image of a real scene in order to obtain information and/or control machines or processes.* This dissertation focuses on three dimensional underwater machine vision.

There exists a tremendous body of work on machine vision in a non-ocean environment. It has been the subject of substantial research that has generated significant results over the past decade, including the realization of three dimensional vision from inherently two dimensional devices (cameras). There are numerous applications for this technology; inspection, process control, guidance, materials handling, etc. Automated robotic machines on land, often equipped with optical sensors, are increasingly relieving us of tedious and repetitive industrial tasks. In the ocean, especially the deep ocean, safety and cost dictate that robotic vehicles are the only practical means of undertaking long duration activities. However, attempts to apply techniques developed for application "in air" directly to the underwater environment have not been exceedingly successful.[2] The optical characteristics of water are less favourable than air and standard machine vision techniques ported to underwater use are often inappropriate or intolerant. Some techniques work but few, if any, provide new features which have capitalized on the unique properties of water in the manner of this dissertation.

Many vision algorithms exploit the presence of scene features such as edges and color changes. Light underwater is attenuated and scattered resulting in non-uniform scene radiance and lack of contrast, and undersea objects are often rounded with no contrasting features [13, 14, 15]. Also underwater, there is frequently movement within the medium itself, movement of the camera and source (particularly if it is vehicle carried), and movement of the target. The salient differences faced in underwater imaging are

---

[2] Notwithstanding this, there has been some significant accomplishments in underwater machine vision over the past decade. These will be reviewed shortly.

summarized in Table 1.1. Figure 1.1 is a series of photographs taken over a span of less than one minute during an attempt to map the subsurface profile of an iceberg. Note that with the exceptionally calm sea, one would anticipate a stable environment.

Air	Deep Ocean
Illumination	
stationary uniform time-invariant	moving non-uniform time-varying
Medium	
non-absorbing non-scattering	absorbing scattering
Environment	
structured	unstructured
Objects	
objects with features and strong texture natural	objects with few or no features

Table 1.1: Optical sensing comparison of typical senario for controlled environment "in-air" versus underwater (from [13])

Although research which includes water properties to enhance underwater machine vision is limited, the properties themselves have been the subject of substantial investigation over the past several decades and the topic of many books (such as [16, 17, 18, 19, 20]). One of the earliest accurate reports of the variation in light attenuation of water as a function of wavelength was given by James and Birge [21] followed shortly by Clerke [22]. Nils Jerlov [16, 18], considered by many to be "the father of ocean optics", made significant contributions to our understanding of the subject and instituted a

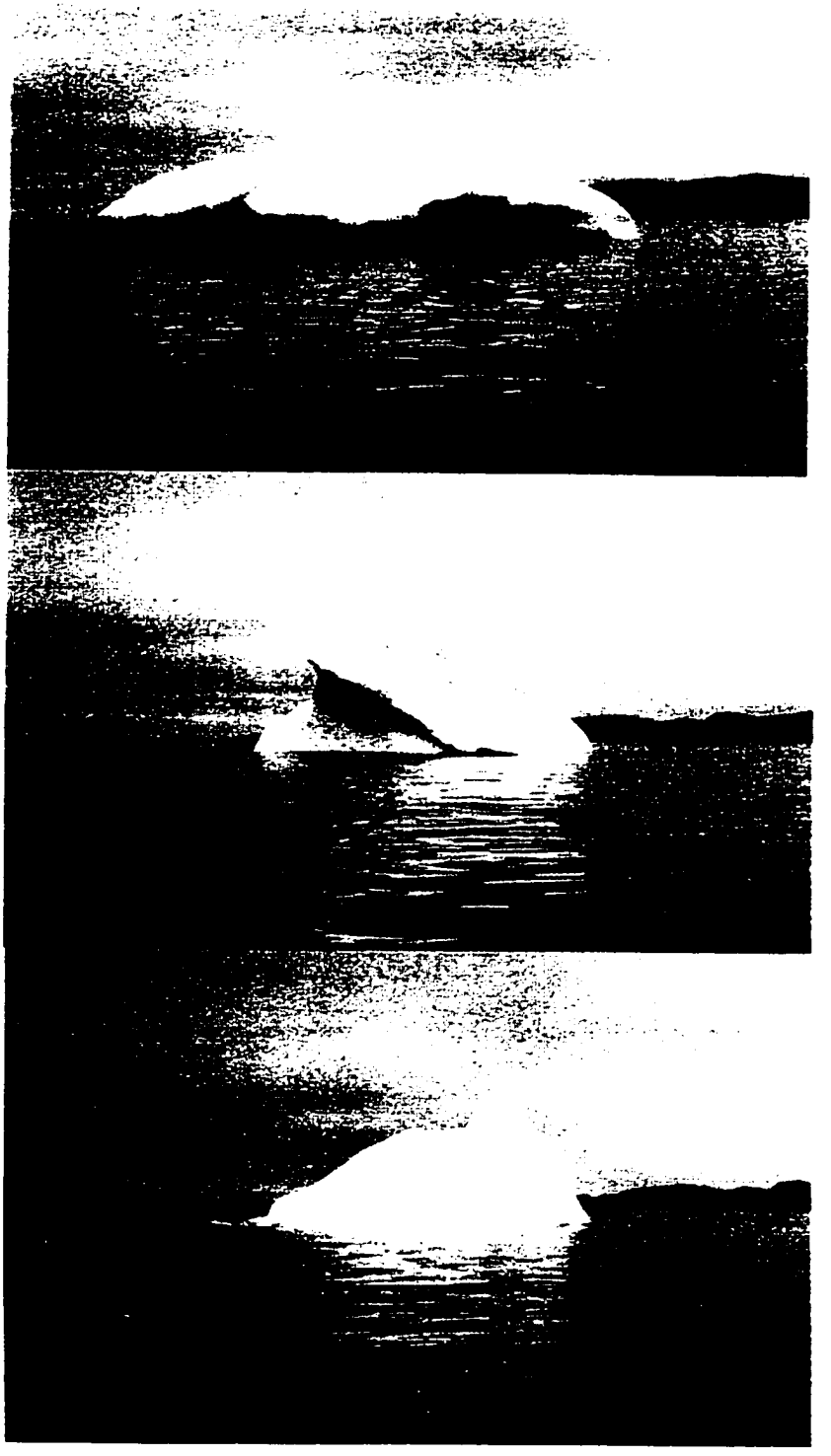

Figure 1.1: Sequence illustrating dynamic marine environment

classification standard for water based on optical spectral properties [23]. Seibert Duntley also dedicated his life to studying the optical properties of water and compiled most of his findings in a much cited 1963 publication [24] considered by many to be the quintessential paper on optical oceanography.

Duntley and his contemporaries explained that, being electromagnetic radiation, light propagating through the ocean interacts with the water and other particulate absorbed or suspended in it. The effects of this interaction - absorption, fluorescence and scattering, are all functions of light wavelength and all but fluorescence cause attenuation in light intensity[3]. Hence attenuation of electromagnetic energy in water is a function of frequency, and minimum attenuation is found in the visible light spectrum [25]. The theory and models developed in the cited works (and others) are inherent in the discussion on optical properties of the sea in the next chapter of this thesis.

When all the parameters known to affect the propagation of light in water are considered, particularly multiple scattering [24, 26], the model becomes mathematically untractable and simulation methods are required for advanced study [20, 24, 27, 28, 29 30]. Development of suitable simulation approaches and algorithms was slow until the late 1960s, in part because of limited computational power but primarily because multiple order scattering models were (and are) based on empirical data and the hardware did not exists to measure very small angle ($<1^{o}$) scattering [26, 31, 32]. A breakthrough came in 1969 when Willard Wells showed that a transformation existed between the volume scattering function of water and its modulation transfer function [33].[4] This permitted a valid, closed form solution to the problem of modelling image formation in a scattering medium by dividing the medium into "slabs". Further detail on this is provided in

---

[3] Forward scattering may actually increase intensity as explained in Section 2.

[4] The volume scattering function and modulation transfer function will be defined in subsequent chapters.

Chapter 5. The validity of this approach was subsequently confirmed by others [34, 35, 36].

From that work, McGlamery developed a computer model that incorporated the inherent optical properties[5] for light in water [37, 38]. This model has been extensively used as a research tool and to simulate the effects of various lighting and camera configurations on the formation of underwater images [39]. Researchers at Woods Hole Oceanographic Institute subsequently used the model in a commercial software package called UNCLES [40]. The model's ability to predict radiance values has been repeatedly confirmed [38, 41, 42] and it is currently used by the US Navy, Scripps Institute of Oceanography, Woods Hole Oceanographic Institute and others. It has also been employed on such high profile projects as designing the imaging system for the ARGO vehicle on its exploration of the TITANIC [43].

In 1990 McGlamery's computer model was extended to predict multi-spectral irradiance [44]. It is interesting to note that although it was straight forward to expand the model for colour simulation, it was not done for 15 years. This reflects a theme that from the literature appears prevalent in the design of underwater imaging systems – namely that since colour is "lost" at such short ranges underwater, little is gained from the use of colour imaging systems.

Understanding the physics of light in water coupled with reliable simulation tools, developments in sources and sensors, and new signal processing methodologies, have led to significant advancements in underwater imaging applications and technologies. By minimizing the common volume of illuminated water between the source and the sensor (thereby minimizing backscatter), laser-based systems have achieved image formation at distances in excess of five attenuation lengths[6]. Anglebeck proposed an underwater laser

---

[5] absorption, scattering, and their scalar sum, attenuation.

[6] An attenuation length is the reciprocal of the attenuation coefficient and will be discussed further in Chapter 2.

scanning imaging system as early as 1966 [45] but the inefficient lasers of the time were impractical. Since then, advances in laser technology have increased efficiency and reduced the size and price in addition to offering a variety of output frequencies. Although pulse repetition frequencies suited to the production of video-rate images are difficult to achieve [46] this technology has tremendous potential for long range static laser line scanning (LLS) and synchronous scanning (SS) [47] where a vehicle or towed platform provides the other degree of motion to create a surface map or obtain range data in two dimensions [10]. In the recent (1996) search for wreckage from TWA flight 800, a LLS proved again that optical vision systems can also be used to advantage underwater [48].

Notwithstanding advances in laser imaging, "commercially available cameras continue to be the mainstay of underwater imaging, in all fields of underwater activity, with the most significant technology improvement in the past ten years being the advent and maturing of CCD imaging devices" [8]. Indeed conventional imaging using still or video cameras has continued to receive considerable attention and advancement [49]. Light intensifiers such as the ISIT (intensified silicon intensifier target) or ICCD (intensified charge coupled device) provide outstanding performance in low light conditions [50]. The advantage of low light cameras is that they are readily adapted without the need for special purpose scanners or detectors [46]. With high speed CCD switching, range gating to exploit the fact that light scattered back from the medium arrives at the camera before light reflected from the surface of interest is also possible to reduce the backscatter received by the camera. This typically requires *a priori* knowledge of range to the surface being imaged, but has also been used for coarse range finding by storing sequences of gated images [51].

A hybrid underwater imaging system consisting of a low light camera as a detector and a LSS to scan an underwater scene was developed and reported in [52]. By range

gating the camera to avoid receiving backscatter the combination has produced 2-D intensity images at 5-6 attenuation lengths [53, 54].[7]

Other hybrid systems employ structured lighting to extract shape from apparently featureless subsea images. Moiré contourography is a technique whereby a light grating or grid is projected onto a surface to produce a spatial frequency pattern. Elevation changes modulate the Moiré pattern allowing depth estimates to be computed based on the modulation pattern [55]. Moiré contourography has been successfully used in air and has the significant advantage of allowing a range "snapshot" of the scene without resorting to mechanical scanning techniques such as those described above [56]. It has been used with some success underwater but only for very short ranges (typically <1m). At longer ranges the turbidity of the medium distorts or destroys the coherence of the signal [57, 58].

Enhancements in the ability to quantify underwater image data are being exploited by the underwater robotics community both for environment perception and as a real time sensor in a host vehicle's control loop. Underwater navigation via optical means is still in its infancy [10] but is a very active research area, particularly for close range navigation such as, docking, station keeping, and maneuvering within cluttered regions (see for example [59, 60, 61, 62, 63, 64]). Of course the purpose of the vehicle is to provide data on, or interact with, the underwater environment or objects contained in it. The very high resolution and real time characteristics of machine vision makes it ideal for telemanipulation [61, 65,] and inspection [66, 67]. However, underwater scenes often exhibit nearly identical reflectance over large areas making the task of detecting and interpreting depth cues very arduous [14, 15, 68, 69].

---

[7] This imaging range was achieved with range gating which requires the approximate distance between the luminaire, target, and camera.

Yu, et. al. developed an underwater machine vision technique that computed the orientation of surfaces based solely on intensity gradient, thereby mitigating many of the problems encountered when underwater images are devoid of salient features. *That research is likely the most comparable to the work presented in this thesis.* In his Ph.D. thesis [70] and associated publications by Yu, Negahdaripour, and associates [71, 72, 73, 74, 75, 76, 77], Yu extends the "shape-from-shading" approach to 3-D vision to the problem of computing orientation of an underwater Lambertian planar surface. It is stated to be the only research on "...applying machine vision techniques in light attenuating media such as clear sea waters...". Assuming a perfectly planar surface, fully illuminated by a non-distorted point light source, Yu employed computer simulation to demonstrate how surface orientation can be computed from the irradiance intensity gradient. The work is significant in that it confirms the validity of using underwater optical properties to extract information about a scene and provides another tool for underwater image interpretation. It also has severe limitations. Application is restricted to planar surfaces with moderate slopes and, because it cannot tolerate shadows or other illumination variations it requires a single, point light source (which is never available underwater because of scattering). Perhaps most importantly, the approach has never been demonstrated to work in a scattering medium. A new approach to underwater imaging proposed in this thesis alleviates all of those restrictions and provides significantly more information (such as range) with less computation.

All of the techniques and technologies discussed thus far for underwater machine vision consider only monochromatic image analysis. When colour images are acquired, information based on the colour content is typically not extracted. One explanation found in the literature for not using colour information is that the associated "inclusion complicated image processing and analysis techniques is difficult because of real-time data handling constraints" [67].

A recent literature review confirms that for underwater machine vision "the majority of research involves methods applied to gray scale images while color characteristics have not drawn enough attention" [78]. This is not the case in remote sensing. Spectral analysis of images acquired by satellite and airborne multispectral scanners (MSS) is relatively common for detection and classification of resources such as vegetation and minerals. Attempts have also been made to use multispectral analysis for classification of seabed substrate based on bottom reflectance. This has been of limited success since interpretation of data is complicated by variations in the spectral attenuation of the water cover resulting from variations in water depth. Subsequent to starting this thesis it was discovered that, in trying to correct for color distortion caused by water cover, researchers appreciated the possibility that multispectral analysis of spaceborne and airborne data could potentially yield water depth information. This is a remote sensing problem with data received by a passive system and an initial source of unknown (solar) spectral irradiance. It is further complicated by reflections from the sea surface and internal reflections within the water column. The latter is termed the *albedo* of the water body, defined as the ratio of *upwelling* to *downwelling* irradiance and is a function of wavelength and depth. Upwelling irradiance is the radiant power density propagating *up* from a horizontally homogeneous[8] water body. Similarly, downwelling irradiance is the radiant energy per unit time and area propagating *down*.

Both of the above parameters are a function of surface conditions that may not be stationary within a scene. Within the region covered by a single satellite image, changes in bottom substrate are also a near certainty. The goal was not to measure water depth but rather develop algorithms which infer depth changes so that appropriate adjustments could be made in image hue or substrate classification boundaries. Unfortunately such

---

[8] In this case upwelling and downwelling irradiance is a function of depth and wavelength. If the water were not horizontally homogeneous, measured irradiance would also be a function of position in the horizontal plane. This quantity is *spectral upward/downward plane irradiance.*

algorithms are rare [79] and no techniques were found which did not require *in situ* measurements taken by a second instrument. Still there are some notable approaches to the problem.

Lyzenga [80] measured radiance from N spectral bands and noted that for remotely sensed data and a constant bottom reflectance, the natural logarithm of radiance measured in one spectral band over a changing depth plotted against the natural logarithm of radiance measured in another spectral band is (in the absence of noise) a straight line (unfortunately this is not the case for a self-contained underwater vision system). If substrate reflectance changes, data points then fall on a parallel line. An $N \diamond N$ transformation rotates the coordinate system resulting in N-1 depth invariant variables which are functions of bottom reflectance only. These variables are then used to classify bottom substrate. An N^{th} variable is depth dependent and the possibility of inferring depth data was investigated but found to be very computationally intensive and requiring *a priori* information about bottom composition which had to be co-registered with the satellite image. Subsequent literature deals only with substrate classification from the N-1 variables [81, 82] and no further work on depth estimation has been found.

Jupp offers a robust and computationally efficient approach to determining water depth from the depth of penetration of each spectral band [83]. When radiance measured in a given band approximates that measured from "deep" water it is assumed that all light energy received in that band is reflected from the sea surface. Water depth is determined to be within a given range band with the number of range bands being equivalent to the number of spectral bands having a unique maximum depth of penetration. Although the quantization intervals are quite large this technique has been successfully employed and found to be very useful.

Nordman *et al* also demonstrated the utility of using multispectral analysis for determining substrate classification and water depth [84]. The use of satellite imagery again required numerous "control points" of known depth and bottom reflectance to be

included in the image. Based on these points, regression analysis determined scene coefficients for interpolation of the remaining pixels in the image. Although coefficients and water depths are determined separately for various predetermined categories of substrate, substrate mis-classification and variation have introduced depth errors. A mean error of 0.09 m is reported for water depths to 2.76 m. For depths from 3.26 m to 6.10 m, the mean error reported error is 0.31 m, These results are somewhat ambiguous since each pixel represents an area of 625 m^2 side and a definition of "actual depth" is not provided.

The most recent development found in the literature on multispectral analysis of satellite ocean images is work by Bierwierth et al [79]. In this work, substrate reflectance and a representative number for depth are derived from the same algorithm. Deep water irradiance (i.e. upwelling through the sea/air boundary and light reflected from the surface) is subtracted from measured irradiance to account for surface reflections and the images are further corrected to account for atmospheric effects, instrument gain, and presumed solar irradiance. Light energy reflecting from the seabed is assumed to be constant at some arbitrary value permitting calculation of a depth estimate. It is recognized that such an estimate is erroneous, however under certain presumed conditions the error is relatively constant and intra-pixel changes in the depth estimate is indicative of changes in actual depth. From this estimate substrate hue can be preserved regardless of depth variations and, since those researchers are interested in bottom classification, that is the enhancement they sought to achieve.

A recent work by Paschos and Valavanis [85] is one example found in the literature using a multi-spectral approach to underwater machine vision. The researchers use colour to segment underwater images, primarily for fish stock analysis. The result is complementary to the work in this thesis in that by using that algorithm, surfaces of different coloured areas may be segmented for generation of individual range images.

1.2 A Novel Approach

As exploration and commercial exploitation of the underwater domain increases, so does our requirement for a myriad of subsea technologies, not the least of which is diverse and reliable technologies for subsea sensing. This thesis develops an underwater machine vision system that converts multi-spectral *intensity* images into *range* images for three dimensional scene reconstruction.

Instead of the usual "top-down" approach to underwater machine vision and working despite the medium to adapt existing algorithms, the approach for this thesis was to study the distinctive optical properties of the medium and discern what additional information is contained in light underwater that is not present in light in air. This triggered the natural progression of questions: assuming there is additional information, how can it be used, how accurate is the information; how susceptible to error is it; and what are the instrumentation and computational implications? Using this approach, the intensity–range transformation system was developed. As far as we know, this is the first underwater machine vision development which exploits characteristic spectral variations in water to extract quantitative three-dimensional information from two-dimensional images.[9]

The developments contained herein are certainly not presented as the solution to all subsea image and ranging applications. They do however, fill an important niche not currently addressed by other available sensors – that of an optical imager that can provide high resolution three dimensional data at video rates in a compact unit for a reasonable cost. Other sensors exist that in various measures outperform the sensor developed herein. For example, the ultimate in high resolution, long range imaging and 10^{-3} m

---

[9] Possibly because cameras capable of acquiring optical data in the correct format are a fairly recent development; three and four (vidicon) tube cameras were available but would have been extremely impractical.

range resolution is provided by emerging LSS and SS laser systems. They cost on the order of $600,000 (US) [86] and do not provide the surface hue information that is so important in many applications, such as environmental monitoring [87]. Nor can they acquire "instantaneous" area data for a moving scene or camera.

For many applications the work here offers several important advantages over existing techniques for obtaining three dimensional data. The more significant of these are:

- it does not require salient features such as edges or light gradients for visual cues to interpret an image;
- it requires magnitude data only and is very computationally efficient;
- it does not require prior scene information, but if such data are available it can be used to enhance interpretation;
- it simultaneously computes range for every pixel within an image;
- it requires only minor changes to readily available hardware;
- the sensor is a single camera with a single lens, there is no mechanical scanning or stereo imagery required;
- it acquires all data within a field of view in tenths to thousandths of a second, hence is highly motion insensitive;
- it is insensitive to most system variations and geometries. It does not require assumptions between illumination source and camera such as coincident or coaxial location.
- it generates a closed form solution;
- it "opens the door" for new underwater image processing techniques based on spectral differencing.

These characteristics permit this vision method to succeed in situations where it is extremely difficult to acquire accurate three dimensional data with other techniques.

The work presented herein was primarily motivated by the sensor requirements for subsea robotic vehicles, both autonomous and remotely operated working in deep water

(> 50 m); nonetheless, the developments can be extended to diver carried cameras and cameras deployed by other methods, and "stand-alone" systems. The first anticipated utilization will be for assessment and modelling of pipelines on the seabed and deep underwater profiles of icebergs. Subsea technology is becoming very important to oil and gas companies preparing for production off Canada's East Coast [88] and there is a strong desire to have untethered underwater vehicles (UUVs) with the inspection capabilities described [89]. A typical operational area is shown in Figure 1.2. When in one piece, the mass of the iceberg shown exceeded 2,000,000 tons. Attempts to map its subsurface profile using acoustic techniques were unsuccessful but a dive in a manned submersible visually confirmed that it was grounded in over 200 m of water. Subsurface profiles are important for ice management so that the maximum depth for potential scour (and subsequent damage to hardware on the seabed) can be computed. As opposed to just the draft, the iceberg profile is required because of their instability. Computing iceberg profiles is an optically well formed problem since its surface characteristics can be predetermined with a high level of probability and are nearly constant across the visible light spectrum.

There are many other potential civilian and military uses for a vision system with an intensity–range transformation capability. In discussing this work with others, interest has been expressed in using it for:

- mapping the underside of sea ice. The present approach is to use an upward looking sonar but the resolution (pixel size) is inadequate. There is also a desire to have actual images registered with the range data. This has not been possible with the sonar data whereas the vision system operates on the actual image yielding precise registration.

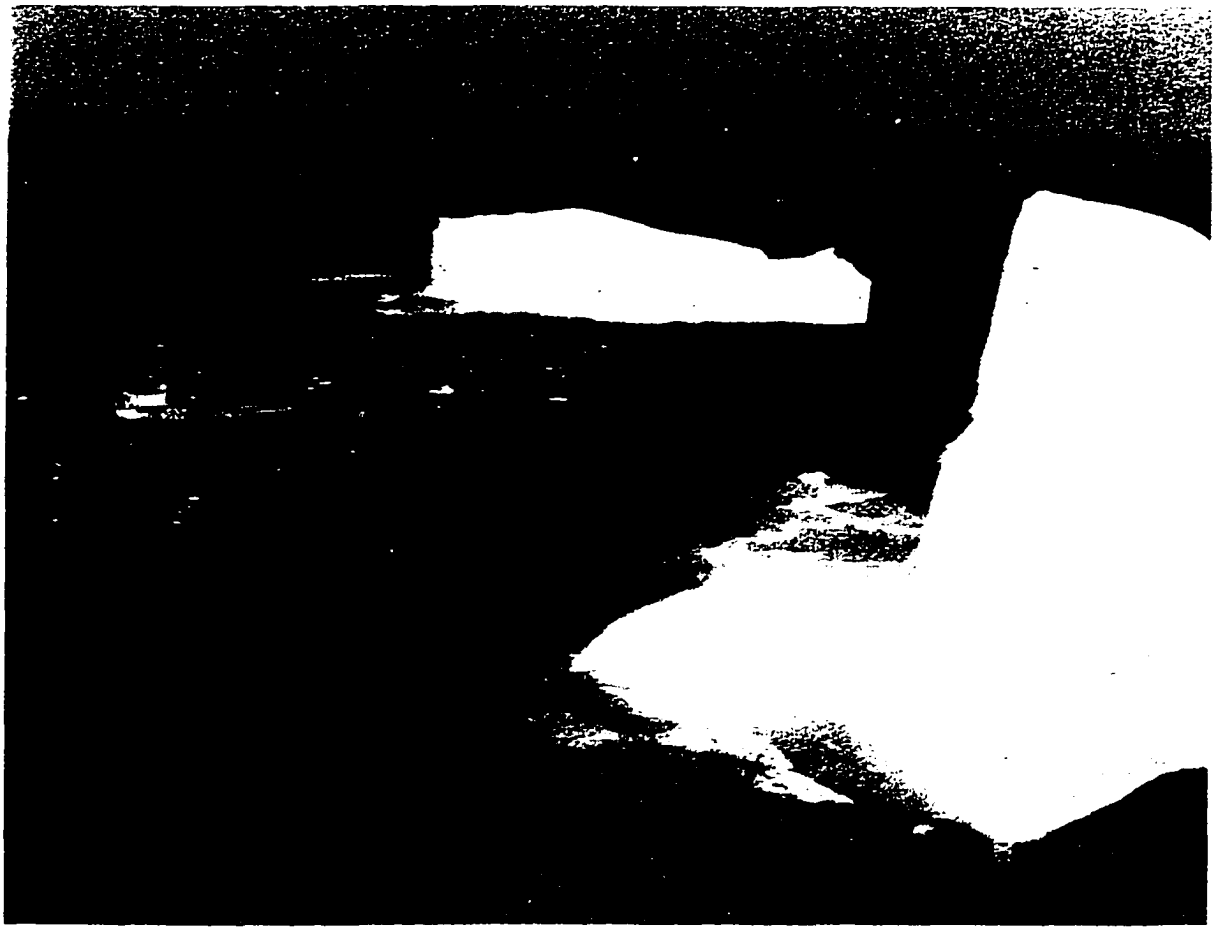

Figure 1.2: Typical scenario where a vehicle mounted machine vision system could obtain valuable 3D profile data

- mapping the disposition of sand on the seabed and the changes in "ripples" due to storms. A custom narrow beam scanning sonar is currently used but problems have been encountered with shadow zones and inadequate resolution. This is an ill formed vision problem of determining range to an apparently featureless surfaces with unknown optical properties. Such surfaces, common in underwater scenes, appear to contain no distinct features such as edges. Even under artificial light when viewed from above, the deep seafloor often appears as an expanse of gray-brown silt making it very difficult to estimate elevation changes. This effect is not limited to extreme

depths. Experience shows that tracking submarine cables blanketed in silt (which is usually the case) is nearly impossible because of difficulties in visually detecting the overlying ridge without moving the center of projection close to the seabed. That in turn stirs silt and reduces visibility. This is an common problem that can be addressed by the work herein.

- guiding a device used to inspect the integrity of welds underwater. This is presently a robotic manipulation problem where a specially designed sensor must track along welds on subsea structures. Stereo vision has been repeatedly tried but is too slow and often doesn't work at all because the entire structure is painted the same color (or has discoloured to the same hue). Other sensing strategies have been tried but are either too slow, lack the required accuracy, or interfere with the integrity sensor.
- autonomous vehicle docking. The work for this thesis was conducted in collaboration with a subsea vehicle manufacturer for its potential use in vehicle docking and station keeping.

It is hoped that the work presented herein will form the basis for further applied research towards these and other applications.

1.3 Document Layout

The work presented in this thesis is derived from the unique properties of water as a medium for the propagation of light. Chapter 2 presents the theory of light propagation in water in terms of *inherent optical properties* (attenuation, scattering and absorption). Spectral variability of these properties is illustrated for various water types and the physics and effects of scattering are presented.

Chapter 3 presents a "standard" reflectance map which is further generalized. From this, the intensity–range transformation is derived. Issues related to its implementation are identified and a calibration procedure is developed to mitigate these problems. A

means of seperating the two portions of light propagation, from the source to the scene and the scene to the camera is derived such that camera to scene range can be explicitly computed for general imaging geometries. The Chapter provides a numeric example which illustrates implementation of the calibration procedure and execution of the transformation. It confirms that a closed form solution for range is possible but does not consider noise and scattering effects. This is studied in Chapters 4 and 5. Chapter 3 concludes with actual images taken underwater and the three dimensional range maps generated from the intensity–range transformation.

As discussed previously, when scattering of light by water is included in the model of light propagation, the model becomes mathematically intractable. By omitting scattering effects, further understanding can be achieved from analytic analysis of the intensity–range transformation, its sensitivities, and the effect of image noise. Chapter 4 conducts a probability analysis of the transformation and through a sensitivity analysis, insight is gained into preferred implementation modes for the system. Also considered in Chapter 4 is the use of multiple spectral channels in estimating range, and a technique developed by Kirlin [90] is presented.

Chapter 5 evaluates the performance of the machine vision system under various conditions. First under the assumption of no scattering, its performance is compared with the theoretical analysis in Chapter 4. To realistically study performance of the system, a simulated environment is developed where the optical properties of the water can be varied and various degrees and types of scattering introduced. Since many of these parameters have little intuitive "feel", images generated under the various conditions are presented with the results from the vision system.

Chapter 6 presents conclusions from this work and recommendations for future research and applications development.

Chapter 2

Optical Properties of Water

2.0 Introduction

Electromagnetic energy propagating through water interacts with the medium yielding absorption, scattering, and fluorescence effects. The effect a body of water has on the transmission of light, termed the water's *inherent optical properties*[10] (IOP) is reviewed in this Chapter. First, the attenuation of light in water is examined and found to be the cumulative effects of absorption and scattering. Although neither of these phenomena is elementary, absorption is a scalar quantity and can be satisfactorily presented within the attenuation section. The contribution of light scattering on the IOPs of water and the formation of underwater images is more complex and appropriately presented in a separate section.

Considered first is light traveling in a collimated beam. This is a very special case but useful for demonstrative purposes and is the standard approach to begin the study of light in water. Attention is subsequently shifted to broader beam but still directional light sources of the type normally used in underwater imaging systems.

---

[10] as opposed to apparent optical properties such as upwelling and downwelling radiance

2.1 Attenuation of Light in Water

Attenuation of light results from two independent physical processes; absorption and scattering. Water absorbs light through the conversion of light energy to heat energy while scattering is a spatial redistribution of light energy. While both these processes may be a function of frequency, the spectral variation in attenuation is due almost entirely to absorption [29]. The spatially varying scattering *function* is a complicated variable to model and is discussed separately in Section 2.2. This section considers the scalar scattering *coefficient*, the absorption coefficient, and the associated attenuation.

2.1.1 Attenuation of Monochromatic Light

Within the infrared portion of the electromagnetic spectrum the conversion of light to heat energy is due to *molecular* resonance, while at the ultraviolet end it results from *electronic* resonance. Water molecules are electrically polarized so resonance (consequently absorption) is particularly high on the low (infrared) side of the frequency spectrum. Further, resonance in liquids is generally broadband and continues into the visible light spectrum. Since the wavelength of same-frequency light is different in air than in water, it is more informative to describe these phenomena with reference to wavelength. Minimum absorption for sea water typically occurs around the 475 nm (blue-green) wavelength [28], but suspended particulate called "yellow substance" common in coastal water shifts this null toward longer wavelengths. Yellow substance is in highest concentration in coastal, estuarial, and lake waters causing these bodies to appear greenish compared to ocean water. Figure 2.1 plots spectral attenuation for various water types. In the plot, the effect of yellow substance is evident in the Chesapeake Bay data. For reference, Figure 2.2 is a plot of the colour spectrum as a function of wavelength.

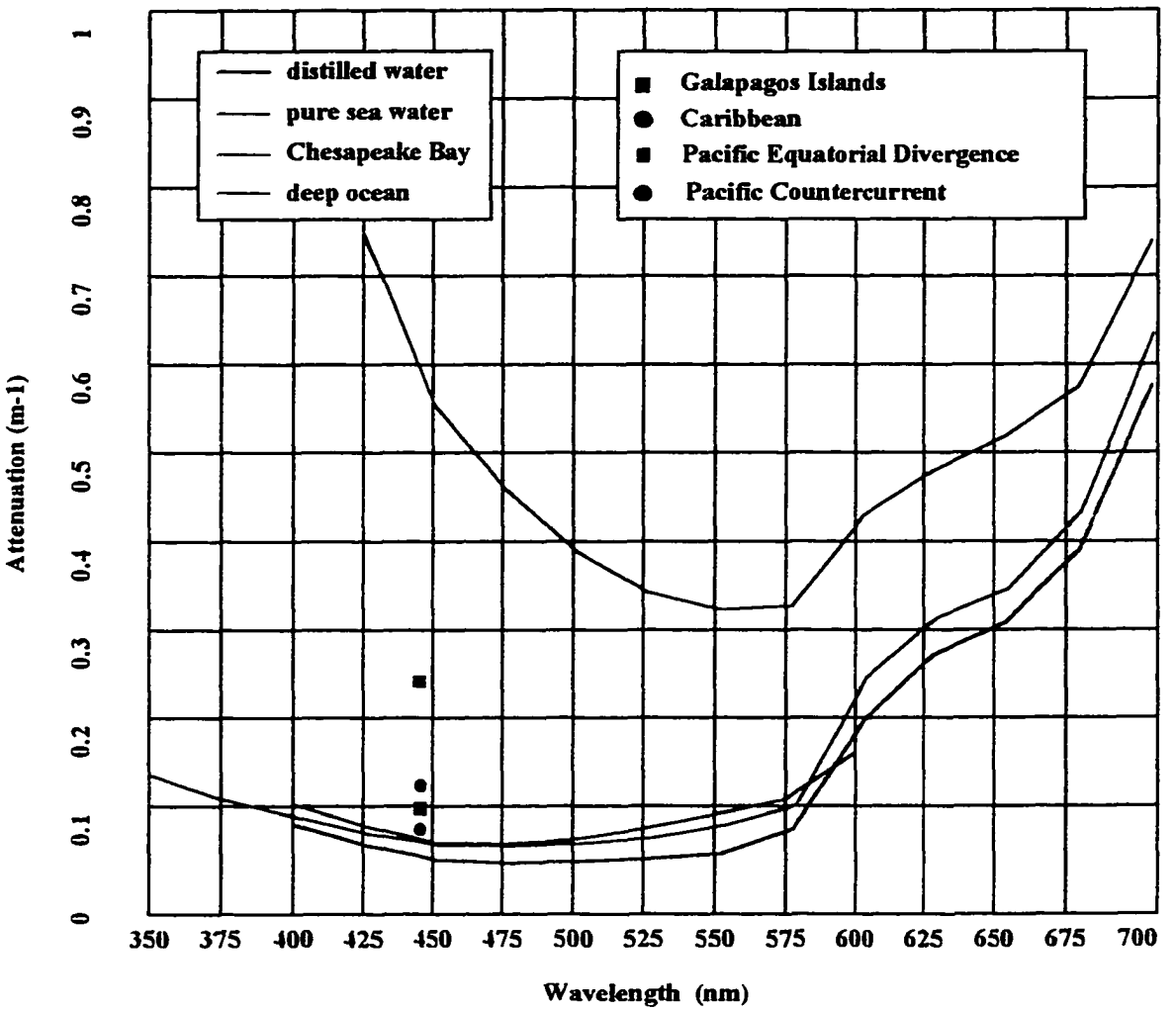

Figure 2.1: Spectral attenuation of light for various waters [3, 4, 91, 92]

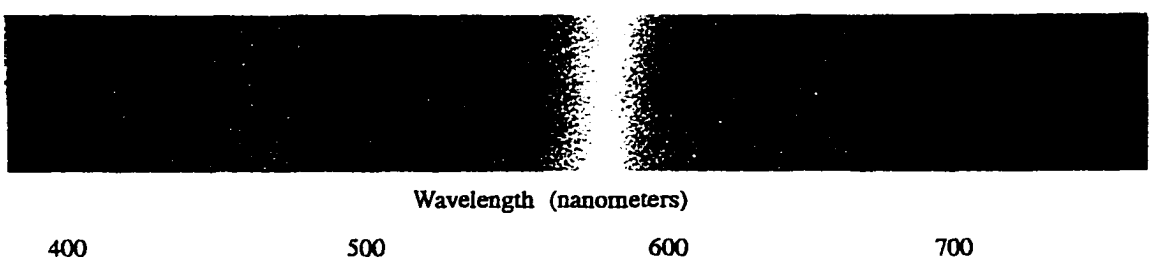

Figure 2.2: Colour spectrum as a function of wavelength

Being a function of wavelength, absorption is quantified by measuring light energy received in very narrow frequency bands from a calibrated source. Fluorescence, the transformation of radiation from one wavelength to a longer one, may appear to contribute to absorption. In fact, the maximum estimated contribution of fluorescence to apparent absorption is 2% [24].

Attenuation of light energy by water is most succinctly introduced with reference to a highly collimated light beam and an elemental volume of water as depicted in Figure 2.3. The following development draws from theoretical concepts found in many texts and papers such as [17, 18, 24, 27, 29].

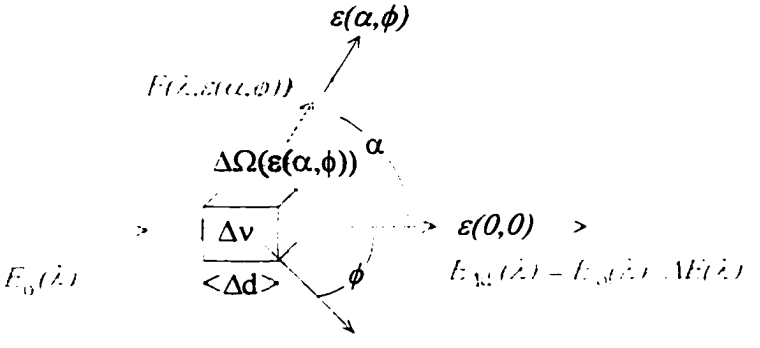

Figure 2.3: Illustration of light scattering from an elemental volume of water

Figure 2.3. illustrates a small volume illuminated by a collimated light beam with spectral irradiance $E_0(\lambda)$ traveling in direction ε. Within the volume, spectral irradiance $\Delta E(\lambda)$ is lost through absorption and scattering and $E_0(\lambda)$ - $\Delta E(\lambda)$ radiates out of the volume in the original direction. Assuming Δv sufficiently small to eliminate the

possibility of second or higher order scattering[11], the irradiance at some distance d along the beam is given relative to a reference irradiance by the exponential equation:

$$E_d(\lambda) = E_o(\lambda)e^{-c(\lambda)d} \tag{2.1}$$

Where: $E_d(\lambda)$ = irradiance of light with wavelength λ at a distance d from the reference irradiance $E_0(\lambda)$;

$c(\lambda)$ = volume attenuation coefficient at wavelength λ.

The parameter $\{c(\lambda)d\}$ is the *optical depth*. The volume attenuation coefficient results from a linear combination of scattering and absorption [4, 91], hence:

$$c(\lambda) = a(\lambda) + b(\lambda) \tag{2.2}$$

where: $a(\lambda)$ = volume absorption coefficient;

$b(\lambda)$ = volume scattering coefficient; a scalar representing the total fractional power scattered out of Δv and is defined in greater detail in the next section.

Collectively $a(\lambda)$, $c(\lambda)$, and $b(\lambda)$ comprise a body of water's *inherent optical properties* [24]. It is generally very difficult to measure inherent optical properties. They are however, relatively easy to interpret in terms of constituents of the medium since they are additive over these constituents hence satisfy the Lambert-Beer Law [30]. For example, given b_w, the volume scattering coefficient of pure sea water, and b_p, the volume scattering coefficient of particles suspended in the water, the total volume scattering coefficient b is given by:

$$b = b_w + b_p \tag{2.3}$$

Through radiative transfer, inherent optical properties yield apparent optical properties such as radiance distribution which are more easily measured–a characteristic that is

---

[11] A complication with scattering, which will be addressed in Section 3.2 is that, in all but the most elemental volumes light energy scattered out of the volume may subsequently be partially or completely scattered back in.

in this thesis. The radiative transfer equation[12] has not yet demonstrated a closed form solution (except in the case where $\tilde{\omega}=0$; $\tilde{\omega}$ is defined below) so researchers rely on simulation for examination of the behavior of light in water.

A fourth parameter that is sometimes included in the set of inherent optical properties is the dimensionless quantity, *spectral single scattering albedo*, $\tilde{\omega}$, defined as:

$$\tilde{\omega} \equiv {}^{b(\lambda)}\!/_{c(\lambda)}. \tag{2.4}$$

From Eqn. 2.4 it is seen that $\tilde{\omega}$ approaches unity in waters where beam attenuation is due mainly to scattering, and zero when attenuation results primarily from absorption. It can be shown [20] that the value of the single scattering albedo equals the probability that a photon will be scattered (rather than absorbed) hence it is also known as the *probability of photon survival*.

Volume attenuation coefficient is arguably the most important of water's optical properties. It is therefore not surprising that there are numerous ways of expressing this parameter. The sum effect of scattering and absorption is the net loss of $\Delta E(\lambda)$. The fractional net loss is the *attenuance* defined as:

$$C(\lambda) = \Delta E(\lambda)/E(\lambda) \quad . \tag{2.5}$$

Equation 2.6 expresses the relation between attenuance and the more generally applicable attenuation coefficient.

$$c(\lambda) = \frac{-\ln(1 - C(\lambda))}{\Delta d} \quad \mathrm{m}^{-1}, \tag{2.6}$$

---

[12] For a homogeneous ocean the radiative transfer equation, referring to Figure 2.1, is [20]:

$$\frac{dL(z,\theta,\phi)}{dz} = -cL(z,\theta,\phi) + \int_{\phi'=0}^{2\pi}\int_{\theta'=0}^{\pi} \beta(\theta,\phi;\theta',\phi')L(z,\theta',\phi')\sin\theta' d\theta' d\phi'$$

β is the *volume scattering function* to be discussed in detail in the next section and L is radiance.

where Δd is the elemental distance as shown in Figure 2.3.

The attenuation coefficient is an extremely convenient parameter for irradiance calculations; however, in units of reciprocal distance it has little intuitive meaning for those unfamiliar with its use. A more intuitive way to represent attenuation is in terms of *attenuation length*, $\pounds_c(\lambda)$ defined as the reciprocal of the attenuation coefficient:

$$\pounds_c(\lambda) = 1/c(\lambda) \quad \text{m} \tag{2.7}$$

Substituting Equation 2.7 into 2.1, it is obvious that light traveling one attenuation length in a collimated beam is reduced by $1/e$ or is approximately 36.8 % of its original power.

The clearest natural body of ocean water on earth is reportedly the Sargasso Sea where attenuation lengths exceeding 20 m are not uncommon [24]. Attenuation lengths and attenuation coefficients measured in other regions of the world are listed in Table 2.1 for a 440 nm wavelength [93]. Most of these points are also plotted in Figure 2.1 for comparison. Attenuation in water always varies as a function of wavelength [29]. At any given wavelength, distilled water has the least possible attenuation of any water and is at a minimum in the 480 to 500 nm region where $\pounds \approx 27$ m.

Location	Attenuation Coefficient (c) m^{-1}	Attenuation Length ($1/c$) m
Caribbean	0.125	8
Pacific N. Equatorial Current	0.083	12
Pacific S. Equatorial Current	0.111	9
Pacific Countercurrent	0.083	12
Pacific Equatorial Divergence	0.100	10
Gulf of Panama	0.167	6
Galapagos Islands	0.250	4

Table 2.1: Attenuation of ocean water for wavelength 440 nm

Thus far only propagation of a collimated beam and first-order scattering have been considered. Capturing underwater images typically requires areas to be floodlit by broader beam sources. In this case higher order scattering (Section 2.2.3) and *diffuse* optical parameters must be considered.

The distinction between *diffuse* and *beam* parameters (those discussed thus far) is as follows: *beam* parameters describe effects of the medium on a narrow, highly collimated beam of photons; *diffuse* parameters describe effects the medium has on a directional broad beam light field. For example the scattering component of diffuse attenuation includes first and higher order scattering whereby, for example, radiant energy may be scattered from the beam then scattered back in again. Diffuse parameters are typically classified with apparent optical properties. However, the *diffuse attenuation coefficient*, K, is insensitive to environmental conditions and its variation with wavelength is governed by inherent optical properties [94]; the diffuse attenuation coefficient is therefore considered a quasi-inherent optical property of water [95].

So important is diffuse attenuation that Nils Jerlov proposed a now frequently used scheme for classifying water based on the spectral shape and magnitude of the diffuse attenuation coefficient [23]. In the Jerlov classification, turbidity increases with classification number over the domain Type I, IA, IB, II, and III for open ocean waters, and Type 1 through 9 for coastal waters. Table 2.2 lists the slightly revised [96] percent transmittance and attenuation coefficient for the ocean water Jerlov classifications.

Transmittance $T(\lambda)$, is the fraction of irradiance remaining after propagating one meter. Referring to Figure 2.3 transmittance is defined as:

$$T(\lambda) = \left(\frac{E(\lambda) - \Delta E(\lambda)}{E(\lambda)} \right)^{1/\Delta d} = e^{-K(\lambda)\Delta d} \tag{2.8}$$

The percent transmittance and diffuse attenuation coefficient is also plotted in Figure 2.4 for Jerlov water types I, II, III, and 1. Jerlov Type I is the clearest open ocean water and Jerlov Type III is the most turbid; similarly, Jerlov Type 1 is clear coastal water. The significant characteristic for this thesis is that all four display a strong dependence on the frequency of the light.

	Type I		Type II		Type III	
λ (nm)	K(λ)	T(λ) (%)	K(λ)	T(λ) (%)	K(λ)	T(λ) (%)
350	0.0510	95.03	0.1325	87.59	0.2335	79.18
375	0.0302	97.03	0.1031	90.20	0.1935	82.41
400	0.0217	97.85	0.0878	91.59	0.1697	84.39
425	0.0185	98.17	0.0814	92.18	0.1594	85.27
450	0.0176	98.26	0.0714	93.11	0.1381	87.10
475	0.0184	98.18	0.0620	93.99	0.1160	89.05
500	0.0280	97.24	0.0627	93.92	0.1056	89.98
525	0.0504	95.08	0.0779	92.51	0.1120	89.40
550	0.0640	93.80	0.0863	91.73	0.1139	89.23
575	0.0931	91.11	0.1122	89.39	0.1359	87.29
600	0.2408	78.60	0.2595	77.14	0.2826	75.38
625	0.3174	72.80	0.3389	71.26	0.3655	69.38
650	0.3559	70.05	0.3837	68.13	0.4181	65.83
675	0.4372	64.58	0.4626	62.96	0.4942	61.01
700	0.6513	52.14	0.6623	51.57	0.6760	50.86

Table 2.2: Attenuation coefficient and percent transmittance for Jerlov water types

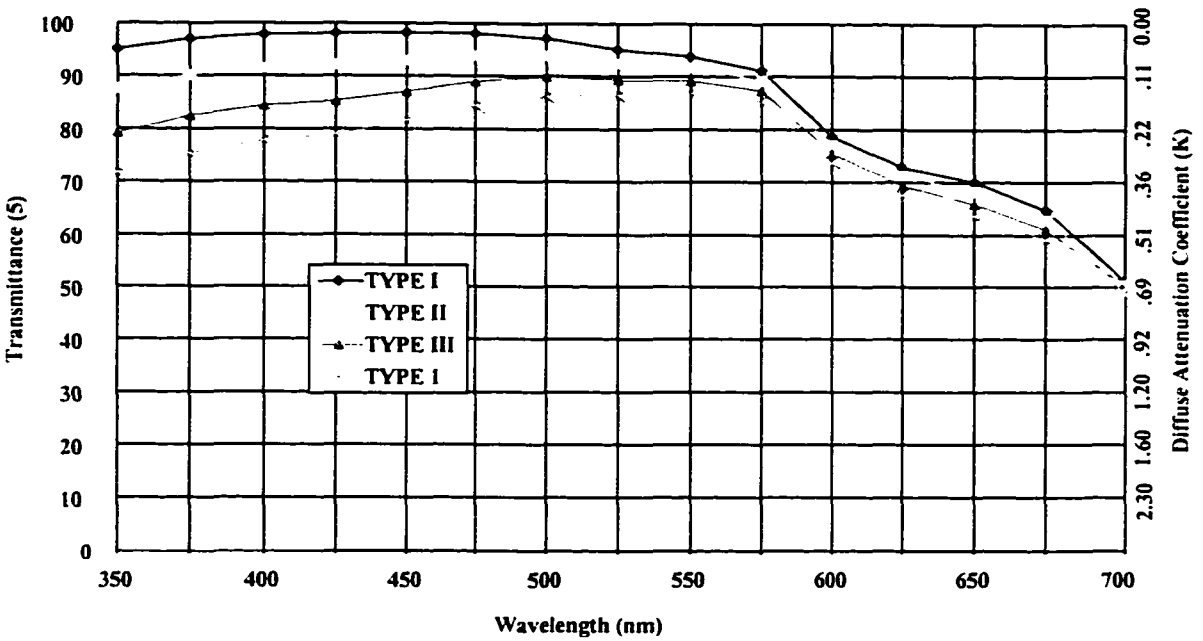

Figure 2.4: Spectral response of Jerlov water types

Attenuation of light underwater is illustrated in the figures which follow. Figure 2.5 is a reduced replica of the color chart that was attached to the top half of the test plate shown in Figure 2.6. The photographs were taken at a depth of 4 m. In Figure 2.6a, photographed at a distance of approximately 2 m, the high saturation and brightness of the color chart (though partly occluded by algae) is clearly evident. In Figure 2.6b, taken at approximately 4m distance, attenuation manifests in the colors being significantly less saturated, particularly in the red band. Also evident is the reduction in image contrast due to scattering of light. The apparent increase in overall image brightness from Figure 2.6a to 2.6b is due to an increase in camera aperture.

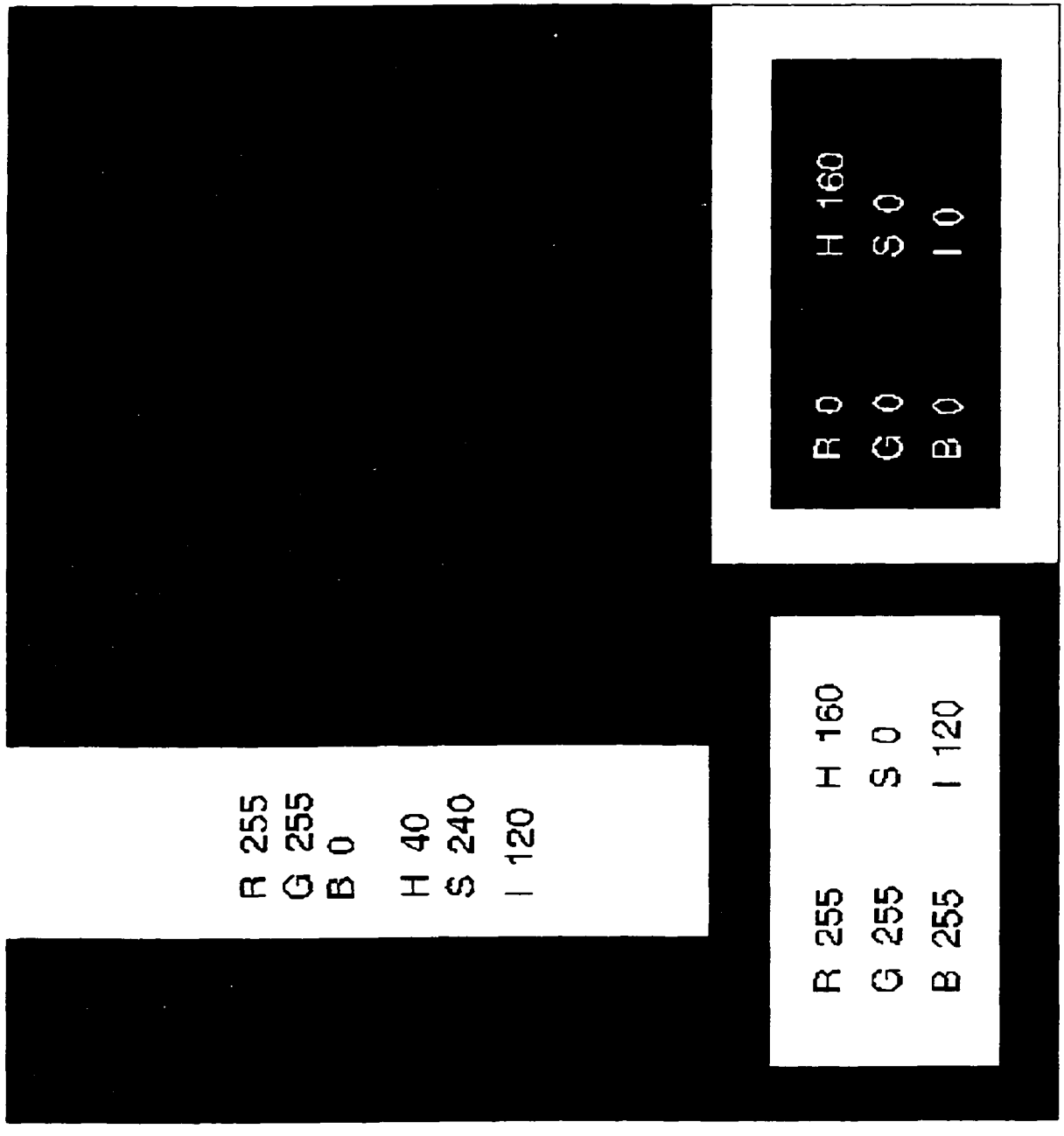

Figure 2.5: Test color palette

Figure 2.6a: Photograph taken at a distance of approximately 2 m

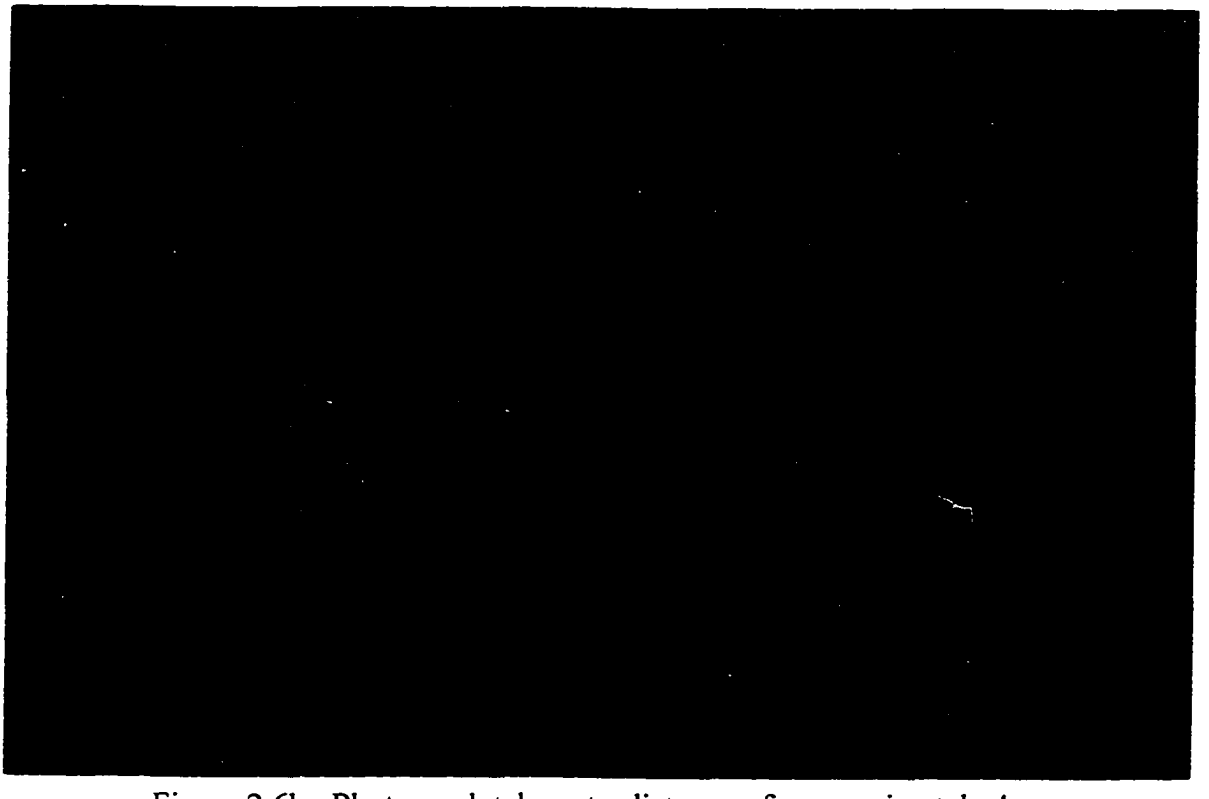

Figure 2.6b: Photograph taken at a distance of approximately 4 m

2.1.2 Attenuation of Non-Monochromatic Light

Thus far propagation of monochromatic light has been considered. For non-monochromatic light, irradiance parameters are calculated by integrating over the entire (sometimes weighted) spectrum of irradiance. For white light, total irradiance is calculated by integrating over the entire visible spectrum:

$$E = \int_{400nm}^{700nm} E(\lambda)d\lambda \tag{2.9}$$

Note that irradiance decay of wide band light is *not* exponential since different frequencies of light attenuate at different rates. This is a fundamental error in irradiance-based computations using non-monochromatic light and the exponential relationship given in Equation 2.1. At short ranges irradiance drops rapidly as lower frequency light is quickly attenuated, at longer ranges when only the blue-green light is present in any significant amount, attenuation characteristics approach the exponential model. Figure 2.7 illustrates the difference between *actual* (from numerical calculations using $K(\lambda)$ in Table 2.2) attenuation and attenuation computed from the exponential model[13].

This Section discussed of the propagation of light underwater in terms of the absorption and volume scattering coefficients. No consideration has thus far been given to how light is scattered out of the ray path and what happens to it. The ability to describe this phenomenon is necessary to model the effects of the underwater medium on the propagation of light. The next section provides a review of the scattering phenomena as a function of that medium.

---

[13] where K is computed from *actual* irradiance at 1m

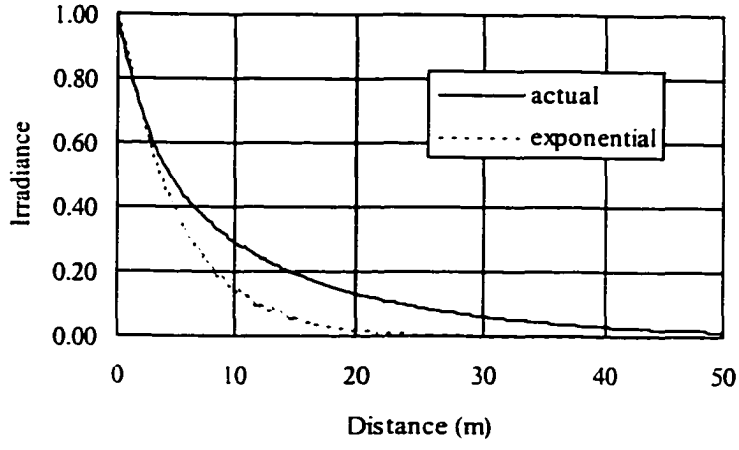

Figure 2.7: Actual attenuation of non-monochromatic light compared with attenuation based on exponential model

2.2 Higher Order Scattering Effects on Light in Water

Section 2.1 introduced the *volume scattering coefficient* $b(\lambda)$ as a scalar function of wavelength. In practice, when using non-collimated light underwater the angular distribution of the scattering coefficient must also be considered; also, elemental volumes of water cannot be considered in isolation since energy scattered out of a light beam may be subsequently scattered back into it. This higher order scattering requires examination of the *volume scattering function*, β.

Scattering of light in water is a complex phenomenon and difficult to deal with analytically. In fact, from the theses examined that were based on development of in-water vision systems, there appears to be a tradition of either ignoring scattering completely or assuming it is removed by "some other means" and not including its effects in the model of light propagation underwater. If the effect of scattering was only an increase in attenuation, problems associated with acquiring clear and detailed underwater images could be alleviated with powerful light sources, CCD's with highly sensitive photosites, and spectral equalizing filters. Unfortunately scattering effects are much more

complex and manifest through two obvious results beyond an increase in attenuation: back scatter causes images to appear washed out; and forward scatter is singularly responsible for the loss of contrast in underwater images. This section provides a more in-depth description of the underwater light scattering phenomenon.

2.2.1 Light Scattering in Pure Water

This Section introduces multiple order scattering with consideration of Rayleigh scattering which can be modelled parametrically. Rayleigh scattering is dominant in pure water but, as will be discussed, accounts for only a small percentage of the scattering in natural water (which must be examined with computer simulation using empirical data). Nonetheless, Rayleigh scattering is a reasonable starting point.

In pure water, light scattering is due to the water molecules themselves and is traditionally modeled by the Rayleigh law:

$$b_R = \frac{8}{3}\left(N\pi r^2\right)\left(\frac{n^2-1}{n^2+2}\right)^2\left(\frac{2\pi r}{\lambda}\right)^4 \tag{2.10}$$

where b_R = Rayleigh volume scattering coefficient;

N = particles per m^3;

n = particle index of refraction at wavelength λ;

r = particle radius.

Water molecules have a radius on the order of 1.5×10^{-10} m hence the Rayleigh scattering coefficient for pure water (with $n = 1.334$) is:

$$b_R = \frac{8}{3}\left(2.361\times 10^9\right)(0.043)\frac{7.890\times 10^{-37}}{\lambda^4} = \frac{2.113\times 10^{-28}}{\lambda^4}.$$

Note from this calculation that 2.361×10^9 is analogous to the geometric cross section of a cubic meter of pure water.

In the blue-green region where clear (not pure) ocean water is most transparent, b_R is on the order of 0.004 m^{-1} accounting for about 7% of the total scattering coefficient and is

dominant only at scattering angles near 90° (were it accounts for up to 2/3 or more of the total scattering). The blue-green color of clear ocean water is almost entirely due to selective absorption [24]. From Equation 2.10 the Rayleigh scattering coefficient is seen to vary inversely as the fourth power of wavelength; however, as will be discussed in the next subsection, small particulate scattering is so heavily masked by the non selective scattering of larger particles that *the total scattering process in natural waters is virtually independent of wavelength.*

As implied above, scattering also varies as a function of scattering angle. This function, called the *volume scattering function* is of prime importance in describing the propagation of light in water and is denoted $\beta(\alpha,\phi)$[14], where α and ϕ are mutually orthogonal angles. Revisiting the elemental volume of water introduced at the beginning of this Chapter, Figure 2.8 below illustrates that α is measured in a plane containing the incident light beam and ϕ is measured in a plane orthogonal to the beam. In homogeneous water, β is constant with respect to ϕ, hence is considered a function of α only. Therefore, the volume scattering coefficient may be computed by integrating the volume scatter function over all α as illustrated by Equation 2.11.

$$b = 2\pi \int_0^{\pi} \beta(\alpha) \sin\alpha \, d\alpha \qquad m^{-1} \tag{2.11}$$

Considering only light scattered at an angle of $\pi/2$ radians or more we define the *backscattering coefficient*, b_b as:

$$b_b = 2\pi \int_{\pi/2}^{\pi} \beta(\alpha) \sin\alpha \, d\alpha \qquad m^{-1}$$

and the *forward scattering coefficient* as: $b_f = b - b_b$.

---

[14] The standard symbol for the volume scattering function is σ, however that is reserved here to denote standard deviation.

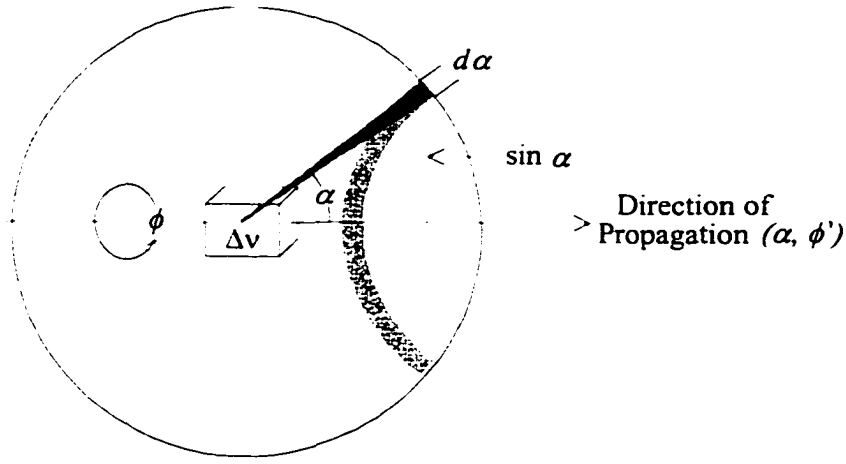

Figure 2.8: Illustration of Volume Scattering Function geometry

The volume scattering function for Rayleigh scattering is given by:

$$\beta_R(\alpha) = \frac{3}{16\pi}\left(1+\cos^2(\alpha)\right)b_R \qquad \text{/m-sr} \qquad (2.12)$$

where b_R is given in Equation 2.10. Figure 2.9 is a polar plot of this function and clearly illustrates the symmetry of the Rayleigh region between forward and back scattering. Also, Rayleigh scattering is relatively independent of scatter angle α, varying by, at most, a factor of 2. This variation is practically insignificant compared with Mie scattering and geometric optics discussed in the next subsection.

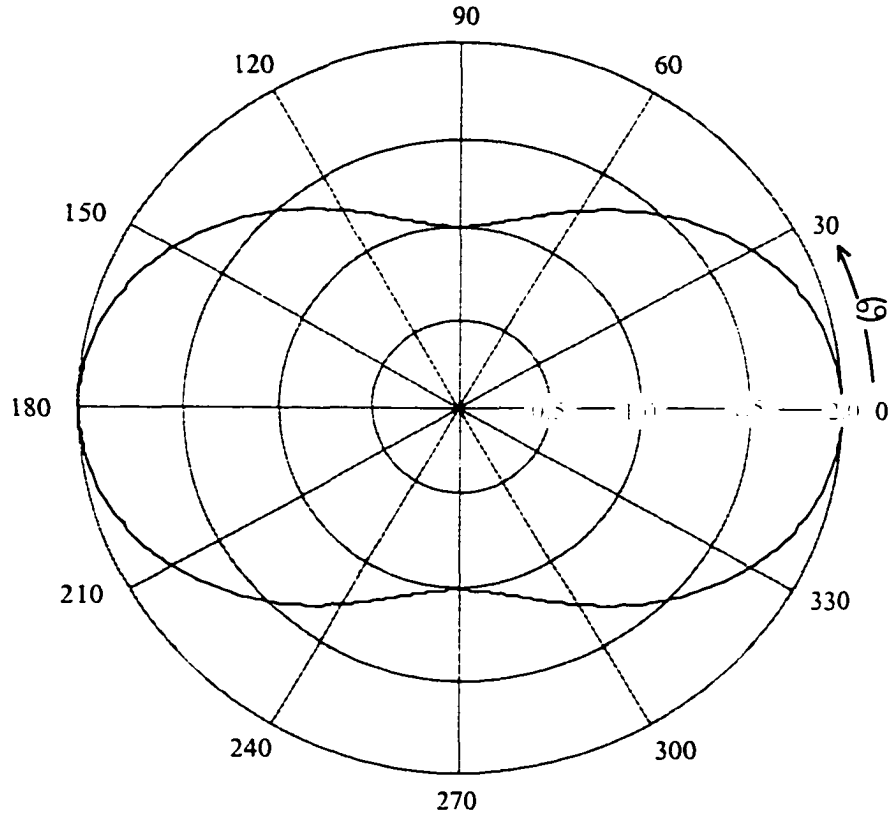

Figure 2.9: Volume Scattering Function, $\beta(\alpha)$, for Rayleigh scattering

2.2.2 Light Scattering in Natural Water

> *Natural waters contain a continuous size distribution of particles ranging from water molecules of size ~0.1 nm, to small organic molecules of size ~1 nm, to large organic molecules of size ~10 nm, to viruses of size ~100 nm, to ..., to whales of size ~10m, to submarines of size ~100m. ... Heroic efforts are required to obtain water of sufficient purity that* (the Rayleigh volume scattering function) *is observed.* [20]

Like a perfect vacuum, pure water does not naturally exist; in fact, it doesn't exist at all in any significant quantity. Natural waters consist of dissolved and particulate matter. Particles whose size approach and exceed the wavelength of light give rise to a very intricate scattering problem. Gustave Mie presented the solution to this problem in a

1908 publication by considering a homogeneous sphere with a complex[15] index of refraction imbedded in an infinite, uniform, non-absorbing medium. In a much simplified version for modeling hydrologic optics the scattering coefficient due to Mie scattering, b_M is a function of the geometric cross-section of the scattering particles and an adjustment coefficient K_M. Hence,

$$b_M = \pi r^2 N K_M \tag{2.13}$$

where: r and N are the same as in Equation 2.10;

K_M = ratio of scattering cross-sectional area to the geometric cross-sectional area comprising the index of refraction of the particle, Bessel functions, and the ratio r/λ. Its shape throughout the various scattering regions is illustrated in Figure 2.10.

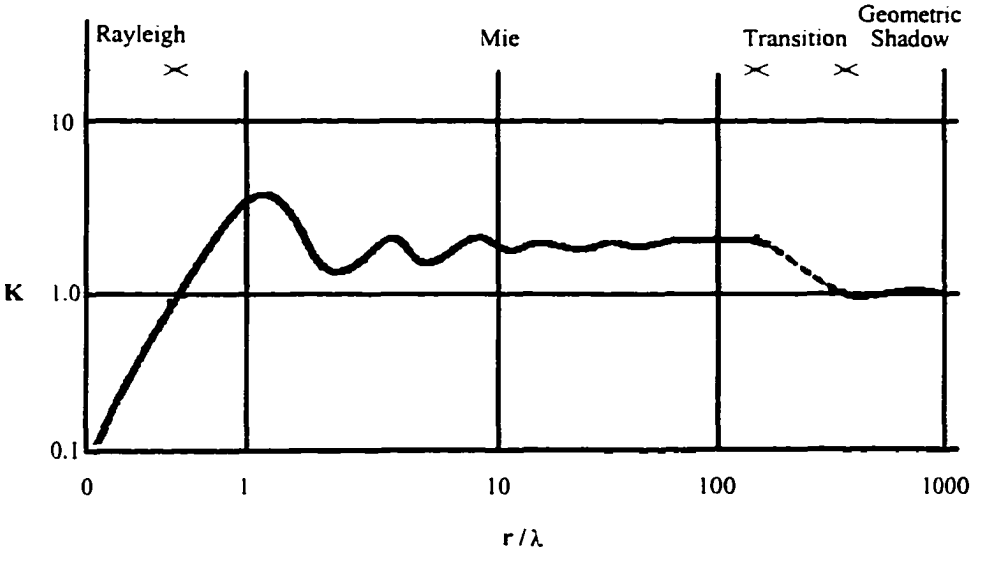

Figure 2.10: Approximate K_M versus ratio of particle size to wavelength of light (from [29])

Mie scattering also predicts a tendency for the volume scattering function to "flatten out" at very small scattering angles. This has been validated in laboratory tests but is not

[15] in the mathematical sense, i.e. of the form a + *j*b

observed in natural waters [97]. The inconsistency is presently attributed to turbulence in natural waters – small temperature and salinity variations generating fluctuations in the index of refraction which causes small angular deviations in the light rays.

Fluorescence, as mentioned at the beginning of this chapter is not a significant contributor in the model of light propagation underwater; however, it is worthy of note in any serious study of scattering. Fluorescence occurs when photons of light energy are absorbed by atoms then re-emitted at another wavelength[16]. When only a portion of the light energy is absorbed by an atom or molecule it is scattered with an increased wavelength. When the kinetic energy of the atom or molecule is transferred to the light energy it is scattered with a decreased wavelength. Either of these types of scattering are described as *Raman scattering*.

2.2.3 Higher Order Scattering

Thus far, only first order scattering from an elemental volume has been discussed. In practice light energy scatters from one elemental volume into another. where it may again be redirected, perhaps back along the original ray. This second and higher order scattering is illustrated schematically in Figure 2.11. From the Figure, the highly contrasted edge that should be apparent in the image will appear to emanate from at least four different directions resulting in a blurred edge in the image. The Figure depicts light emanating from each elemental volume along two or three rays, however one should recall that each elemental volume actually scatters light in all directions according to the volume scattering function and that each transmission path comprises an unfathomably large number of elemental volumes.

---

[16] Fluorescence is sometimes confused with phosphorescence which is re-emission of absorbed light energy after the source of light energy is removed.

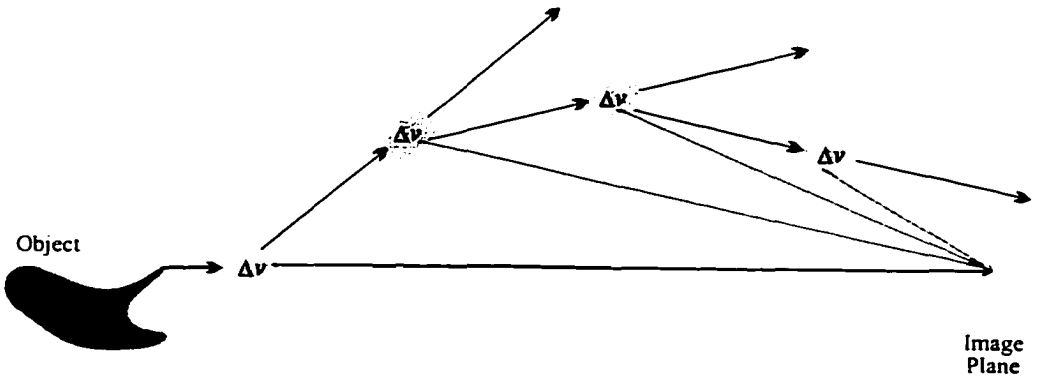

Figure 2.11: Schematic illustrating multiple scattering

Fortunately, as illustrated in the previous section the volume scattering coefficient is strongly biased toward the small angles hence forward scattering is predominant. The qualified effects of forward scattering is illustrated in the following series of figures. Figure 2.12 is a scaled copy of the target attached to the bottom half of the test plate photographed in Figure 2.13 under moderate (for the area) scattering. In Figure 2.13a, taken at a range of approximately 1m, the letters UVIC all have very sharp, highly contrasted edges. Also discernible are the horizontal bands following the "C" and the geometric figures on the bottom of the plate. In Figure 2.13b, taken at an approximate range of 3.5m, the UVIC letters are slightly blurred due to scattering but still quite readable. However, the top three or four horizontal lines are barely distinguishable but it is possible to discriminate between the lines placed farther apart. In Figure 2.13c, imaged from approximately 5m, it is impossible to read anything from the plate. In fact, forward and back scatter have reduced contrast to the point where it is getting difficult to discern the target at all. It is also difficult to distinguish the author in the lower right of the photograph however a light halfway up the right side of the photo can be seen. Its "fuzzy" edges are due to forward scattering.

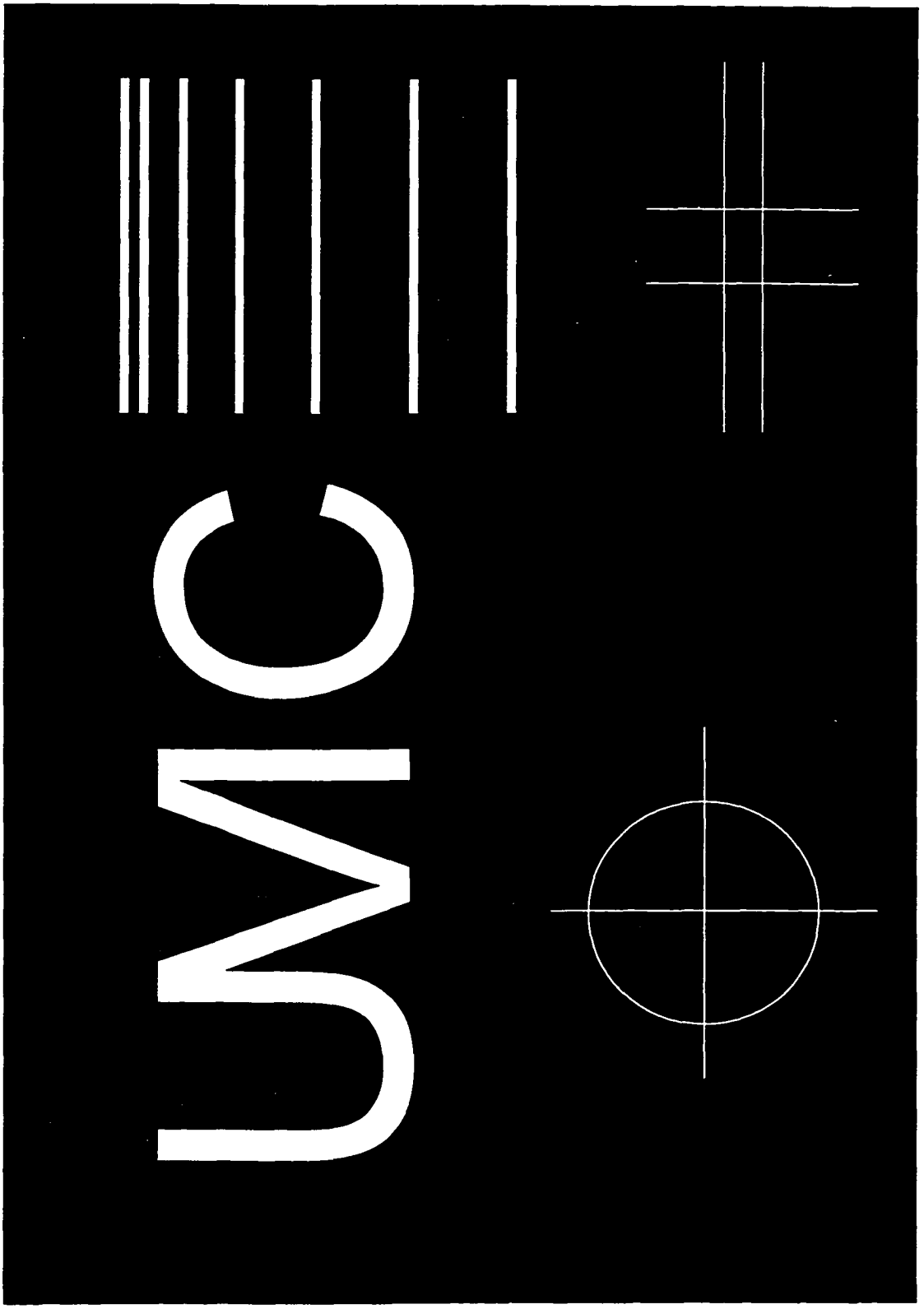

Figure 2.12: Geometric target

Also notable in the photographs of Figure 2.13 is the lack of perspective. The left side of Figures 2.13b and c (about 1/4 of the photograph) indicates a variety of rack surfaces. From the information in the Figure it is very difficult to determine their orientation relative to the camera and whether they are convex or concave. It appears that illumination is from the left and most of the surfaces are convex; when in fact, the illumination source was slightly to the right and many of the surfaces are actually concave. If the author were not present in the photographs, geometric scale would also be indiscernible. Using the techniques presented in this dissertation it will be possible to extract such "three dimensional" data.

Analysis of the effects due to multiple scattering is very complex. Theoretically it may be possible to perform multiple integrations over the entire water volume; however, this is not only computationally impractical but, since actual volume scattering functions are described numerically it cannot be completed in closed form. Nonetheless, some approximations have been tractable in closed form. These include formulations considering only second order scattering and those assuming isotropic scattering (i.e. a spherical shaped volume scattering function). Unfortunately none of these approaches yield acceptably accurate results and analytical techniques have been abandoned in favor of qualitative analysis and quantitative simulation.

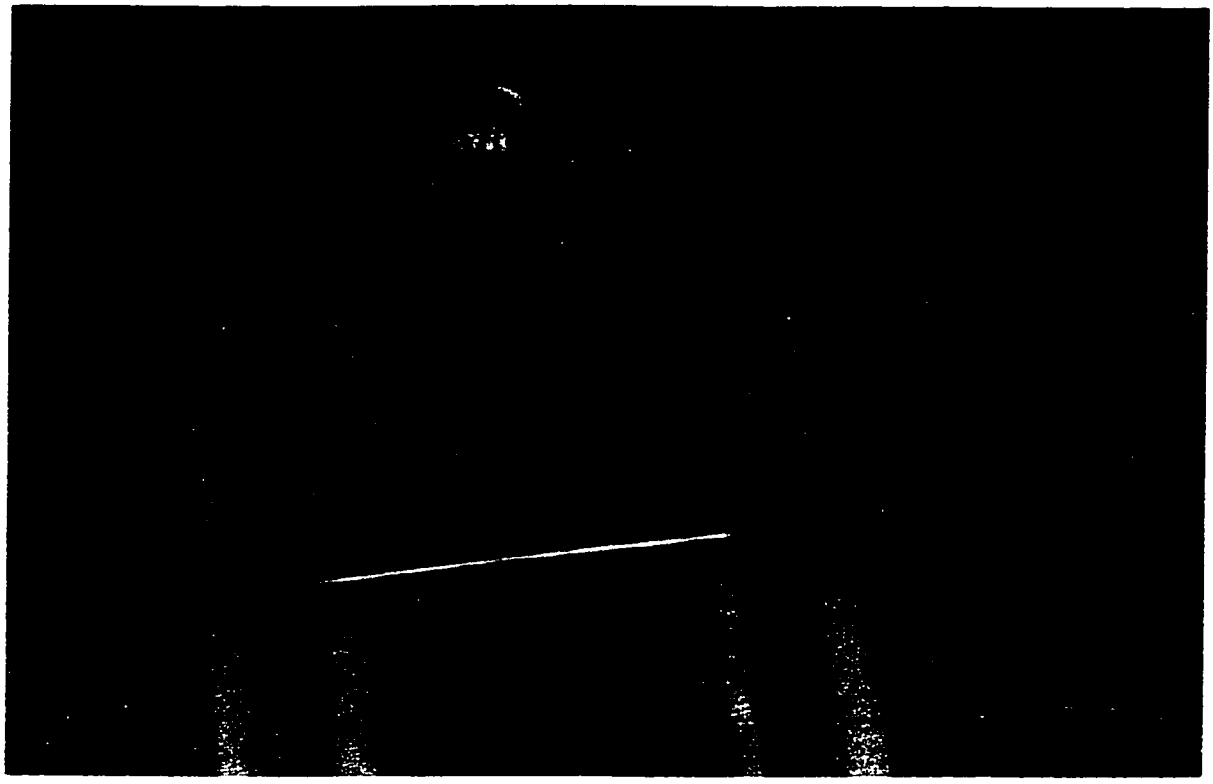

Figure 2.13a: Underwater images affected by scattering; 1 m range

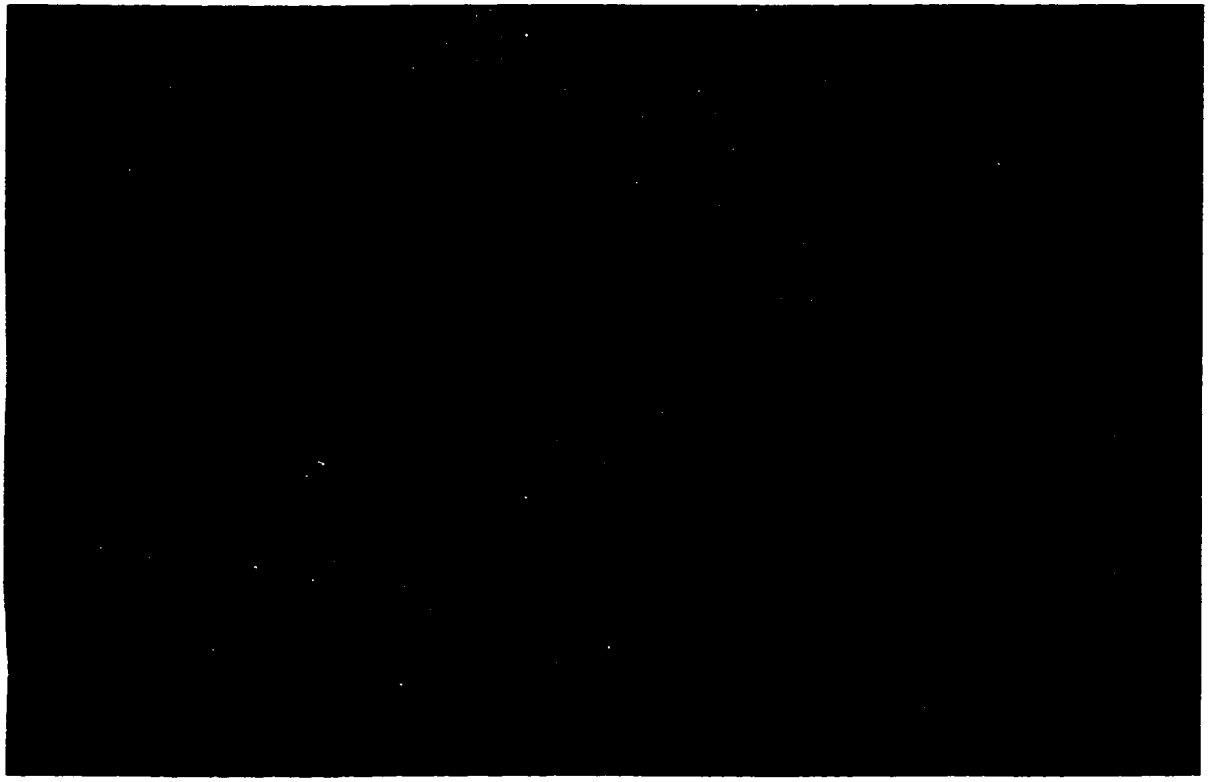

Figure 2.13b: Underwater images affected by scattering; 3.5 m range

Figure 2.13c: Underwater images affected by scattering; 5 m range

2.3 Modulation Transfer Function

Although this dissertation is not intended as a study in the physics of light propagation in scattering media, it is helpful to define a mathematical function for modeling the effects of light scattering. This function, the *modulation transfer function* (MTF), describes a water's optical response to spatial waveforms and is analogous to a system transfer function defined in the frequency domain. The MTF is described in the spatial frequency domain and is analogous to a "conventional" system transfer function. where the transfer function forms a Fourier transform pair with the system impulse response, the MTF forms a Fourier transform pair with the *point spread function* (PSF).

The MTF is best described mathematically. Consider a scene whose irradiance is given by

$$E_{in}(x) = 1 + a_i \sin \omega x \tag{2.14}$$

where ω is the spatial frequency[17] with wavelength 2π/ω. In Figure 2.14, ω = 2π/50 yielding the 50 unit wavelength. If Figure 2.14 was photographed in water, blurring due to forward scattering would effectively decrease the amplitude modulation of the scene resulting in image an irradiance described by

$$\begin{aligned} E_{out}(x) &= 1 + mtf(\omega) a_i \sin(\omega x) \\ &= 1 + a_o \sin(\omega x) \end{aligned} \tag{2.15}$$

where *mtf* is the MTF for the optical system (water) at spatial frequency ω and

$$mtf = \frac{a_o}{a_i}. \tag{2.16}$$

The complete modulation transfer function is found by measuring *mtf* at all frequencies. In general, the MTF for an optical system at any given spatial frequency is the ratio of the output modulation to the input modulation; or, the system's frequency response. The well known work of Willard Wells [33] showed that by using an acceptable small angle approximation, a linearity exists by which (as with any linear system) the net output of the response of the entire optical system is the sum of all the component MTFs.

---

[17] Although most images are two dimensional, symmetry of the homogeneous underwater channel permits valid explanation in one dimension. This will be expanded to two dimensions for illustrating the effects of the MTF.

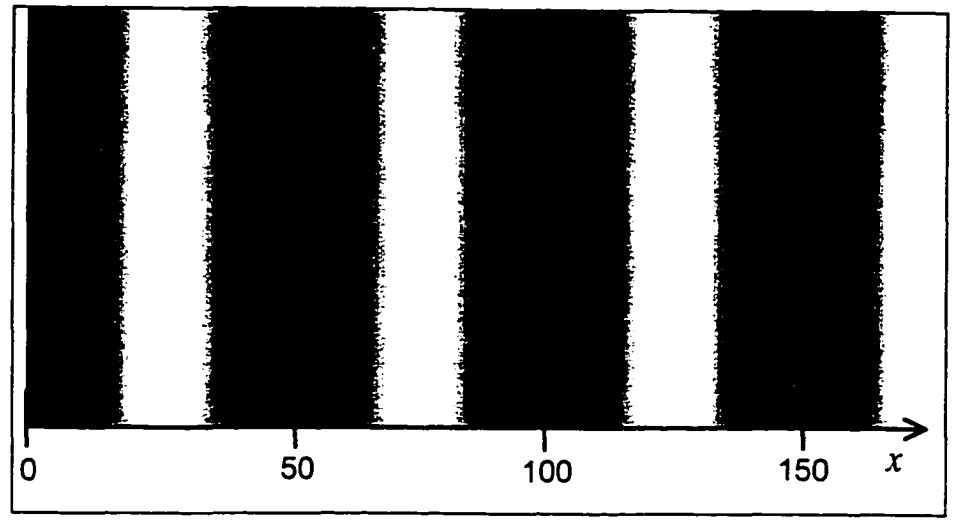

Figure 2.14: Optical system input with $\omega = 2\pi/50$

Figure 2.15 illustrates the effect of the MTF or PSF on an image. Figure 2.15*a* is an intensity plot of an impulse applied to the optical system—the underwater channel. Figure 2.15*b* is the original scene and also how the image would appear in a non-scattering, non-attenuating medium. Water is a scattering medium with a PSF whose shape is often similar to that shown in Figure 2.15*c*. Convolving the PSF with the scene yields Figure 2.15*d*, the system output due to the MTF (or equivalently, the PSF) and commonly referred to as the *glow field* component of the image. In the absorbing and scattering medium of water, as range increases the glow field becomes stronger than the direct image and at sufficiently long range, only the glow field can be distinguished. Nonetheless, the diffuse light received at this range remains significantly more intense near the centre of the beam indicating that the strong forward scattering characteristic noted in the previous section is retained.

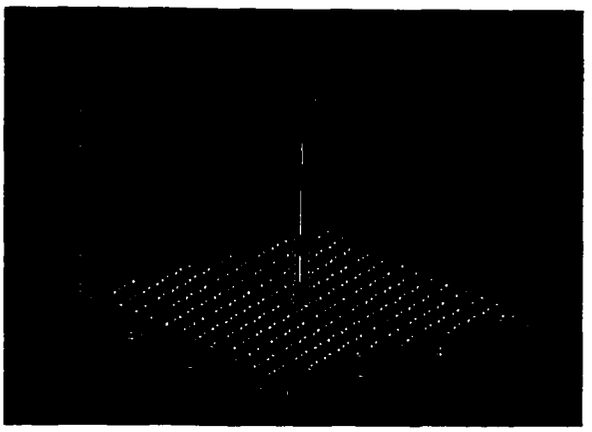

Figure 2.15 a: Scene intensity

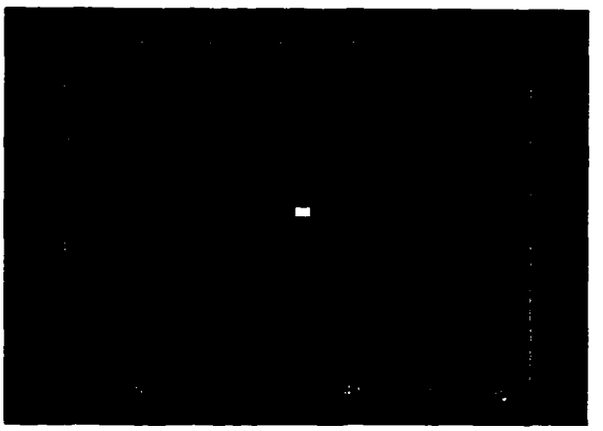

Figure 2.15 b: Non-scattered scene with impulse

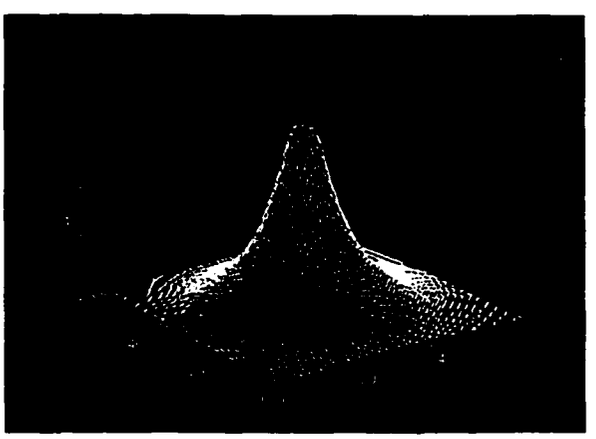

Figure 2.15 c: Normalized PSF

Figure 2.15 d: Image with scattering

Figure 2.15: Scattering modeled by the PSF and its effect on an image

Chapter 3

Multi-Spectral Monocular Ranging

3.0 Introduction

This Chapter contains the conceptual development for a multi-spectral monocular machine vision system capable of producing a three-dimensional scene from a two-dimensional image acquired in an attenuating medium such as water. Section 3.1 introduces the fundamentals which result in a transformation algorithm for the conversion of colour intensity images into a range image. The Section then addresses many issues related to imaging geometry and system calibration and implementation. Section 3.2 presents a numerical example illustrating implementation of the calibration procedure and execution of the transformation. The chapter concludes with actual underwater images and the associated range images generated by the intensity–transformation.

3.1 Three Dimensional Reconstruction from Multispectral Analysis

Chapter 2 discussed the IOPs of water and equations for calculation of light irradiances. A salient point of that discussion was that the attenuation of light energy in water is a strong function of frequency. By exploiting that characteristic in this Chapter, a transformation is derived which converts spectral irradiances into range estimates.

Subsection 3.1.1 describes the generation of irradiance images. Derivation and implementation of the intensity–range transformation are presented in subsequent subsections.

3.1.1 Generalized Reflectance Map

Thus far in this dissertation light energy has been regarded fairly generally as "intensity" levels. Prior to formulating equations for image plane irradiance it is appropriate to define a few key optical terms. The definitions that follow are consistent with those used by Jerlov [16] in the study of marine optics.

Radiant flux (F), units (W): radiant power or the time rate flow of radiant (light) energy;

Radiant intensity (I), units (W/sr): radiant power per unit solid angle emitted by a source. Note that for a point source, I at a given radius from the source is spatially constant in a homogeneous medium. For a directional source I, is a function of emission direction.

Radiance (L), units ($W/m^2 \cdot sr$): power per unit solid angle per unit projected area of a surface; or, radiant intensity measured per unit area. Spectral radiance is the fundamental radiometric quantity of interest in hydrologic optics; however, because of instrument difficulties and because such complete information is seldom required [3], the most commonly measured radiometric quantity is irradiance.

Irradiance (E), units (W/m^2): normalized radiant flux incident on an infinitesimal area of a surface. It is similar to radiance but without the solid angle normalization; i.e. it measures radiant power from several or all directions. Radiance measured from an entire hemisphere is planar irradiance, radiance received from all directions is called scalar irradiance.

It is important to note that these defined quantities are absolute radiometric measures. They are not variables weighted by a luminosity curve to allow for instrumentation (or human visual perception) sensitivities (as in luminance).

In the work presented here we consider an underwater vehicle or robot to be equipped with a vision system consisting of a single camera and a light source. Radiant energy incident on the image plane of the camera is dependent on several factors: radiant intensity of the light source, the IOP of the medium as discussed in Chapter 2, reflectance of the object being imaged, transmittance of the camera optics, and imaging geometry (relative postures of the object, light, and camera). Only the latter is independent of frequency.

Figure 3.1 illustrates the IOPs of water and some of the geometric effects on image formation. In the Figure, ray 1 depicts a direct-reflected path along which light energy travels from the luminaire to a point on the object (P) where it is reflected directly through the camera's lens and focused on the image plane. Not all of the energy initiating along ray 1 makes it to the camera via this direct path. As discussed in Chapter 2 forward scatter, depicted by rays 2, 4, 5 and 7 cause image blurring and/or attenuation. The various effects are described in the Figure. Rays 3 and 6 illustrate attenuation and contrast reduction due to backscatter. Ray 7 is second order forward scattering which, in this case contributes to image blurring by making it appear as though point P is at another location. Multiple order scattering can yield any or all of the above effects. In general *scattering gain*, rays 2, 3, 5, and 7 manifests as blurring and a loss of contrast in the image while scattering loss (rays 4 and 6) contributes to loss of irradiance and is included in the attenuation coefficient in Equation 2.2.

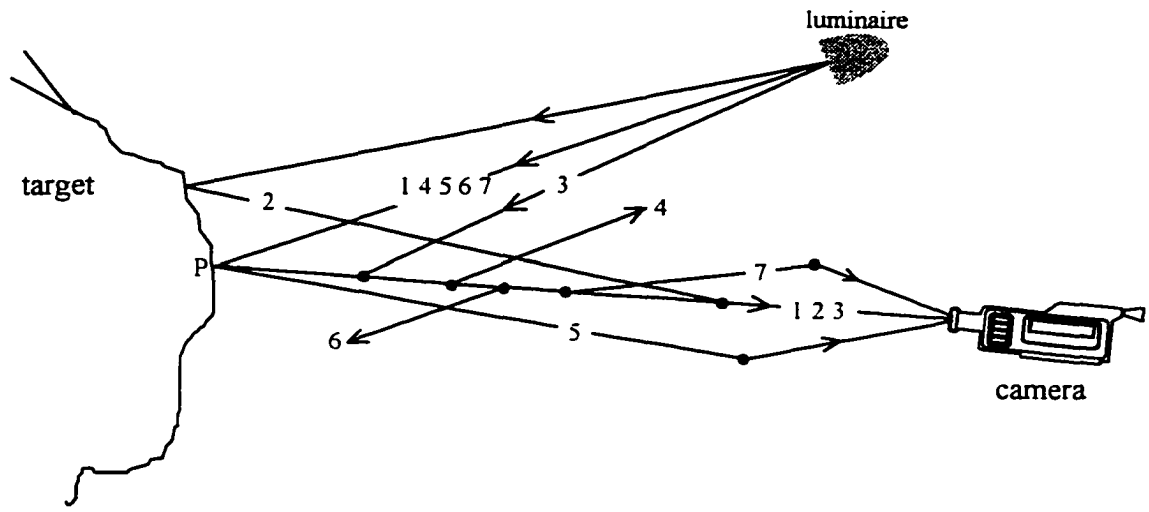

1. Direct Ray
2. Forward Scatter - blurring
3. Backscatter - washing out
4. Forward Scatter - attenuation
5. Forward Scatter - blurring
6. Backscatter - attenuation
7. 2nd Order Forward Scatter - blurring

Figure 3.1: Scattering effects on image brightness

It is common in the following derivation to assume a point light source and a surface with Lambertian reflectance properties. Those assumptions are made here only as a starting point. They are replaced with more general parameters as the development progresses.

For a scene geometry similar to that in Figure 3.2, consider a point light source with spectral radiant intensity I(λ) at a distance d_s from point P on the target object. The radiance on an elemental area at P, perpendicular to a radius vector from the source is given by:

$$L_P(\lambda) = \frac{I(\lambda)}{d_s^2} e^{-c(\lambda)d_s} \quad \frac{W}{m^2 sr} \tag{3.1}$$

where $c(\lambda)$ is the attenuation coefficient.

Assuming a Lambertian reflector with spectral reflection coefficient $\rho(\lambda)$, the reflected irradiance is given by:

$$E_P(\lambda) = \frac{L_P(\lambda)}{\pi}\rho(\lambda) \quad \text{W/m}^2 \tag{3.2}$$

When, as in Figure 3.2, the reflector is not perpendicular to the source vector,

$$E_P(\lambda) = \frac{E_P'(\lambda)\rho(\lambda)\cos(\gamma)}{\pi} \quad \text{W/m}^2 \tag{3.3}$$

where γ is the angle of incidence measured from the surface normal $(\bar{n})$ at P. Hence radiance at point P due to the source with radiant intensity $I(\lambda)$ is:

$$E_P(\lambda) = \frac{I(\lambda)}{\pi d_s^2} e^{-c(\lambda)d_s}\rho(\lambda)\cos(\gamma) \quad \text{W/m}^2 \tag{3.4}$$

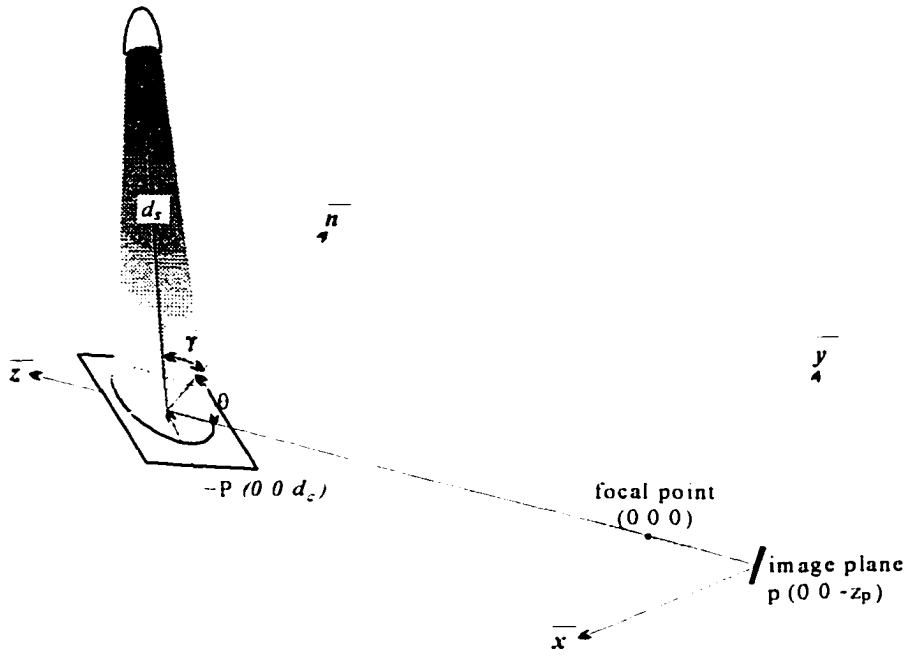

Figure 3.2: Imaging geometry

For mathematical tractability, scattering is not included in the model at this stage but will be reintroduced later. The light irradiance on point p of the image plane due to the radiance at P on the object is given by:

$$E_p(\lambda) = E_P(\lambda)e^{-c(\lambda)d_c}. \tag{3.5}$$

The left side of Equation 3.5 has the lower case subscript p, referring to a point on the image plane and should not be confused with the uppercase P subscript which refers to a point within the scene. Substituting Equation 3.4 into 3.5, image irradiance in terms of source radiant intensity, optical depth, reflection coefficient, and angle of incidence is given by:

$$E_p(\lambda) = \frac{I(\lambda)}{\pi d_s^2} e^{-c(\lambda)(d_s+d_c)} \rho(\lambda)\cos(\gamma) \tag{3.6}$$

Equation 3.6 is the "brightness" equation for a scene with a Lambertian surface illuminated by a point light source. It is also known as a *reflectance map* and is similar to the models proposed in the literature(for example [29, 37, 45, 70]).

The equation is a type of "ideal" model that does not account for the physical characteristics of an actual underwater imaging system. In an actual system, irradiance is not measured at a point in a scene but over a finite, albeit small area represented in an image pixel. We consider each pixel to correspond to a planar "patch" on the surface being imaged. The physical area of the surface patch represented in a pixel depends on camera parameters (such as focal length and CCD photosite size), the distance between the camera and the surface (d_c in Figure 3.2), and the orientation of the surface relative to the image plane. Given a patch size $A(d_c)$ the projected area of the patch onto a plane parallel to the image plane is $A(d_c)\cos(\theta)$ where θ is the camera nadir angle (which is also the angle between the object plane normal at P and a line extending from P through the

camera's focal point as illustrated in Figure (3.2)). Consequently the radiant flux passing through the camera lens from a diffuse reflector is given by:

$$F(\lambda) = \frac{I(\lambda)}{\pi d_s^2} e^{-c(\lambda)(d_s+d_c)} \rho(\lambda) A(d_c) \cos(\theta) \cos(\gamma) filter(\lambda) \tag{3.7}$$

The wavelength sensitive parameters such as lens transmittance and spectral response of the wavelength dependent filter covering a given array are grouped in the term *filter*(λ).

To express Equation 3.7 as an irradiance we normalize by the image plane pixel area *a*. The relationship between camera pixel area and projected scene area, $A(d_c)\cos(\theta)$ is:

$$a = A(d_c)\cos(\theta) m^2 \tag{3.8}$$

where *m* is the camera magnification factor given by:

$$m = \frac{f}{d_c} \tag{3.9}$$

with *f* being the focal length of the camera. Normalizing Equation 3.7 now yields:

$$E(\lambda) = \frac{I(\lambda) e^{-c(\lambda)(d_s+d_c)} \rho(\lambda) \cos(\gamma) filter(\lambda)}{\pi m^2 d_s^2} \tag{3.10}$$

A restriction still inherent in the model is the assumption of a point light source. Underwater imaging systems normally use a directional source to both increase efficiency and reduce the effects of back scatter. We therefore further expand on the previous work to derive a generalized reflectance map with the provision for a conical beam pattern with a uniformly distributed irradiance. A weighting function may be added to account for non-uniform irradiance sources. An advantage of the intensity–range transformation derived herein is that it is sufficiently robust to be unaffected by such non-uniformities.

Referring to Figure 3.3, the angle Ω subtended by a illumination source lens of area A_0 defines the beamwidth of the source. We define *r* to be the *effective radius* which yields the beamwidth Ω. This is given by:

$$\Omega = \frac{A_o}{r^2}, \tag{3.11a}$$

or

$$r = \sqrt{\frac{A_o}{\Omega}}. \tag{3.11b}$$

At a distance d_s from the source, the irradiated area is:

$$A_{d_s} = \Omega(r + d_s)^2. \tag{3.12}$$

Thus the increase in illuminated area over lens area is:

$$\frac{A_{d_s}}{A_o} = \frac{\Omega(r + d_s)^2}{\Omega r^2}, \tag{3.13}$$

and, recalling the irradiance is power per unit area, the decrease due to spreading loss is given by:

$$\frac{E_{d_s}}{E} = \left(\frac{r}{d_s + r}\right)^2. \tag{3.14}$$

Replacing the spherical spreading loss component in Equation 3.10 with Equation 3.14 yields our generalized reflectance map for a planar patch in an attenuating medium illuminated by a directional source with effective radius r. This is given in Equation 3.15.

$$E(\lambda) = \frac{I(\lambda)e^{-c(\lambda)(d_s + d_c)}\rho(\lambda)\cos(\gamma)filter(\lambda)}{\pi m^2}\left(\frac{r}{d_s + r}\right)^2 \tag{3.15}$$

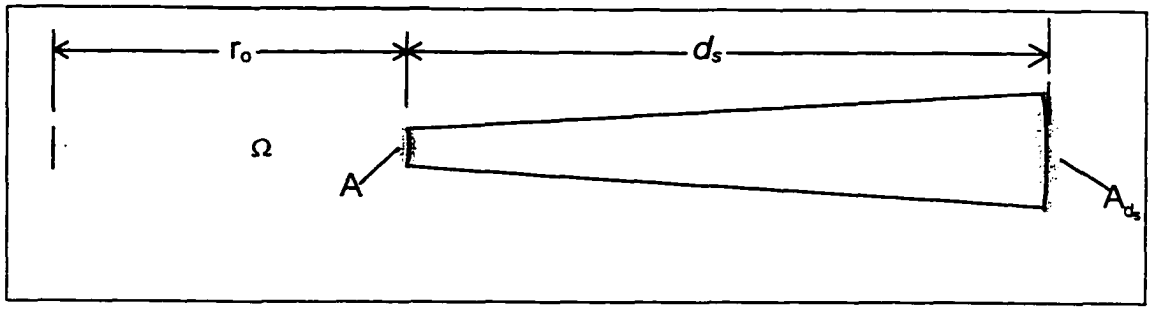

Figure 3.3: Beam spread geometry

3.1.2 Range Estimation

Equation 3.15 infers that the level of received irradiance in underwater imaging is dependent on scene geometry (distance and incidence angles) and the wavelength(s) or frequency of light energy received. Many of the newer CCD cameras measure scene irradiance in three spectral bands (representative of the C.I.E. tristimulus functions) through three separate but registered CCD arrays. With proper calibration and data manipulation, differences in the intensity recorded in each spectral band can be transformed into an estimate of range to the surface patch represented in each pixel of an image. It is therefore possible to generate both an intensity image and a *range* image.

Much of the scene geometry dependence inherent in the measurement of spectral irradiance cancels when considering the ratio of irradiances measured at registered photosites in different spectral bands. For example, the ratio of light irradiance measured in spectral bands λ_1 and λ_2 is:

$$\frac{E(\lambda_1)}{E(\lambda_2)} = \frac{I(\lambda_1)e^{-c(\lambda_1)(d_s+d_c)}\rho(\lambda_1)\cos(\theta)\cos(\gamma)filter(\lambda_1)\pi\left(\frac{r}{d_s+r}\right)^2}{I(\lambda_2)e^{-c(\lambda_2)(d_s+d_c)}\rho(\lambda_2)\cos(\theta)\cos(\gamma)filter(\lambda_2)\pi\left(\frac{r}{d_s+r}\right)^2},$$

which can obviously be simplified to:

$$\frac{E(\lambda_1)}{E(\lambda_2)} = \frac{I(\lambda_1)e^{-c(\lambda_1)(d_s+d_c)}\rho(\lambda_1)filter(\lambda_1)}{I(\lambda_2)e^{-c(\lambda_2)(d_s+d_c)}\rho(\lambda_2)filter(\lambda_2)}. \tag{3.16}$$

Equation 3.16 reveals that, not only is the ratio independent of scene geometry such as incidence angles, it is also independent of camera constants and the illumination source beam pattern. In addition, any assumptions regarding the nature of the reflector (Lambertian etc.) can be eliminated. Rewriting Equation 3.16 to solve for distance yields:

$$d_s + d_c = \frac{\ln\left(\frac{E(\lambda_1)}{E(\lambda_2)}\frac{I(\lambda_2)\rho(\lambda_2)filter(\lambda_2)}{I(\lambda_1)\rho(\lambda_1)filter(\lambda_1)}\right)}{c(\lambda_2)-c(\lambda_1)} \tag{3.17}$$

The two distances, d_s and d_c can be separated by considering the geometry in Figure 3.4. The figure depicts one quadrant of the image plane and the corresponding scene containing point P. The origin of the reference coordinate system is at the focal point of the camera and the *xy* plane is parallel to the image plane. The position of the illumination source is known and placed at (S_x, S_y, S_z) such that there are no assumptions on the source and camera being collocated, coaxial, etc.. The total distance, $d_s + d_c$ is computed from Equation 3.17 and is designated d_T such that:

$$d_T = d_s + d_c. \tag{3.18}$$

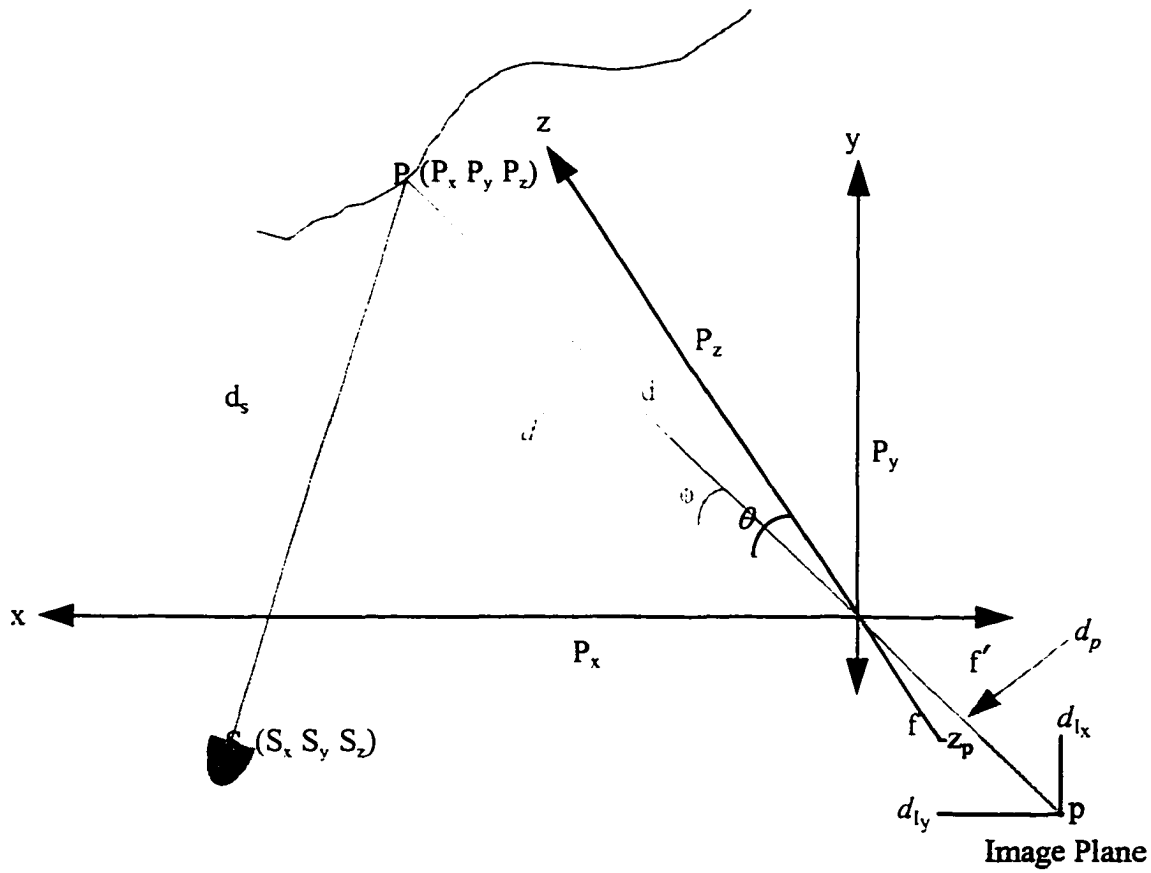

Figure 3.4: Coordinate system for d_c and d_s

The point P lies on an ellipsoid whose foci are coincident with the positions of the luminaire and the camera focal point. From the Figure, total distance can be expressed as:

$$d_T = \sqrt{(S_x - P_x)^2 + (S_y - P_y)^2 + (S_z - P_z)^2} + \sqrt{P_x^2 + P_y^2 + P_z^2}\,. \qquad (3.19)$$

Equation 3.19 can be rewritten as:

$$(S_x - P_x)^2 + (S_y - P_y)^2 + (S_z - P_z)^2 = \left(d_T - \sqrt{P_x^2 + P_y^2 + P_z^2}\right)^2, \qquad (3.20)$$

which, after multiplying out and substituting in range from the camera to surface point P (i.e. d_c) becomes:

$$S^2 - 2\left(S_x P_x + S_y P_y + S_z P_z\right) = {d_T}^2 - 2 d_T d_c . \tag{3.21}$$

where

$$S^2 = S_x^2 + S_y^2 + S_z^2 . \tag{3.22}$$

In Eqn. 3.21, S_x, S_y, and S_z, hence also S are known and d_T is found from Eqns. 3.17 and 3.18. To compute d_c from Equation 3.21 it is necessary to express P_x, P_y, and P_z in terms of known quantities. First consider d_c', the projection of d_c onto the xz plane:

$$d_c' = d_c \cos(\phi) . \tag{3.23}$$

Expressing P_x in terms of d_c' yields:

$$P_x = d_c' \sin(\theta) ; \tag{3.24}$$

similarly,

$$P_y = d_c \sin(\phi) ; \tag{3.25}$$

$$P_z = d_c' \cos(\theta) . \tag{3.26}$$

Substituting Equations 3.23 to 3.26 into 3.21 and solving for d_c:

$$d_c = \frac{S_x^2 + S_y^2 + S_z^2 - d_T^2}{2\left(S_x \cos(\phi)\sin(\theta) + S_y \sin(\phi) + S_z \cos(\phi)\cos(\theta) - d_T\right)} . \tag{3.27}$$

The angles ϕ and θ are found from the position of p, the photosite in the image plane containing scene point P. From Figure 3.4, f is the camera's focal length, I_x and I_y are the CCD array column and row number respectively of the pixel containing p (again considering only one quadrant of the array). For a square, 10 mm CCD array of 512 ×

512 pixels, each I_x and I_y represent an interval 1.95 μm wide. The maximum error in localizing p in this case is:

$$\sqrt{\left(1.95\times10^{-6}/2\right)^2+\left(1.95\times10^{-6}/2\right)^2}\approx 1.38\times10^{-6}m$$

From the image plane geometry in the Figure we can write:

$$\cos(\phi)=\frac{f'}{d_p}=\frac{\sqrt{f^2+d_{I_x}^2}}{\sqrt{f^2+d_{I_x}^2+d_{I_y}^2}}, \tag{3.28a}$$

$$\sin(\phi)=\frac{d_{I_y}}{d_p}=\frac{d_{I_y}}{\sqrt{f^2+d_{I_x}^2+d_{I_y}^2}}, \tag{3.28b}$$

$$\sin(\theta)=\frac{f}{f'}=\frac{f}{\sqrt{f^2+d_{I_x}^2}}, \tag{3.28c}$$

and

$$\sin(\theta)=\frac{d_{I_x}}{f'}=\frac{d_{I_x}}{\sqrt{f^2+d_{I_x}^2}}. \tag{3.28d}$$

Using Eqns 3.17, 3.18, 3.27 and 3.28, the range from the camera to the surface patches represented by each pixel can be calculated with no assumptions about scene or imaging system geometry.

If computation speed is as important as accuracy, the preceding computations in Equations 3.27 and 3.28 may be omitted and it can be assumed that the camera and illumination source (lamp) are equidistant from the patch being imaged such that:

$$\hat{d}_c=\hat{d}_s=\frac{d_c+d_s}{2}=\frac{d_T}{2}. \tag{3.29}$$

The error associated with this assumption is maximum when the difference between d_c and d_s is maximum as illustrated in the simplified coordinate system in Figure 3.5. In that case, assuming the camera and source are both in the *xy* plane, the maximum error is computed as follows:

$$error = \frac{d_s + d_c}{2} - d_c; \tag{3.30}$$

$$d_s = \sqrt{\left(d_c \cos(\theta)\right)^2 + \left(S + d_c \sin(\theta)\right)^2}$$

$$= \sqrt{d_c^2 + S^2 + 2Sd_c \sin(\theta)}; \tag{3.31}$$

$$error = \frac{\sqrt{d_c^2 + S^2 + 2Sd_c \sin(\theta)} - d_c}{2}; \tag{3.32}$$

where S is again the separation in meters between the camera and the lamp, and θ is the complement to the angle formed by the intersection of a line segment containing the camera and lamp and one containing the camera and the imaged point as before. As an example of the magnitude of this error, consider a vision system with a field of view of 20° and a 0.50 m separation between the camera and lamp, at a range of 3.00 m the maximum estimation error resulting from the equidistant assumption is 6.29 cm or 2.10%. At a range of 10.00 m the respective error is 4.94 cm (0.49%).

By recognizing when the projections of the target and source are in different quadrants of the *xy* plane, a correction factor can be applied to reduce this error. It is computed from the ratio of d_c/d_s when the target is on the *z* axis and is given by:

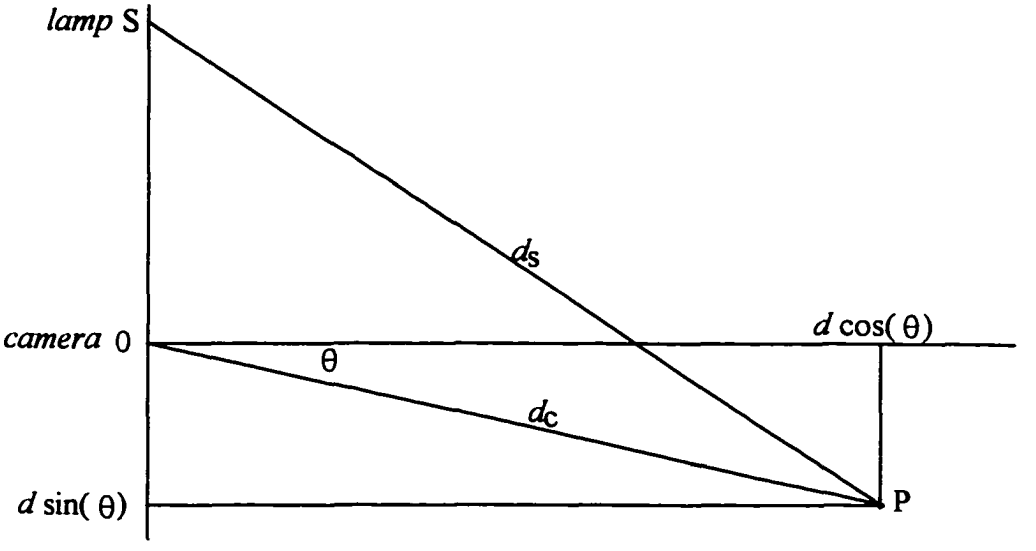

Figure 3.5: Simplified coordinate system for d_c and d_s

$$\hat{\hat{d}}_c = \sqrt{\frac{\hat{d}_c^2}{S^2 + \hat{d}_c^2}} \cdot \hat{d}_c, \tag{3.33}$$

where $\hat{\hat{d}}_c$ is the corrected estimate based on the $\hat{d}_c$ computed from Eqn. 3.29. Using Eqn. 3.33, error is approximated by:

$$error \approx \frac{\sqrt{d_c^2 + S^2 - 2Sd_c\sin(\theta)} - d_c}{2}. \tag{3.34}$$

From the previous example, at 3.0 m range, using the modification in Eqn. 3.33, actual error is 2.29 cm or 0.76% (reduced from 2.10%). The error computed by Eqn. 3.34 is 2.28 cm. At 10 m range the modified estimate has an error of 3.70 cm or 0.37 % (reduced from 0.49%). The error computed by Eqn. 3.34 is 3.37 cm.

For illustration and notational clarity, the approximation in Equation 3.29 will be invoked for the remainder of this Section. Equation 3.17 is rewritten as:

$$d = \frac{\ln\left(\frac{E(\lambda_1)I(\lambda_2)filter(\lambda_2)\rho(\lambda_2)}{E(\lambda_2)I(\lambda_1)filter(\lambda_1)\rho(\lambda_1)}\right)}{2\left(c(\lambda_2)-c(\lambda_1)\right)} \tag{3.35}$$

Equations 3.17 and 3.35 both provide a closed form solution for distance to the imaged patch. $E(\lambda_1)$ and $E(\lambda_2)$ are measured directly and many variables in previous equations have been eliminated. Still one is faced with an equation containing many as yet unknown parameters. Two facts permit the employment of this equation as an intensity-range transformation: first, most of the unknown parameters may be treated as ratios instead of absolute values; second, it is possible to derive a practical calibration procedure to measure or compute many of the unknown ratios.

To be practical, the calibration of an underwater vision and measurement system should be designed to be performed *in situ* without fragile or highly specialized instrumentation (such as transmissometers and scatterometers). Further, it should not require a complex setup as is so often the case with optical calibrations. Calibration should include all components of the imaging system; camera, lamp, and medium. If it is possible to access a surface sample that is representative of the target surface, that should be included as well. The objective of the procedure is to obtain estimates for the attenuation of light within the spectral bands available in the system, source spectral radiant intensity, camera response and, if a surface sample is available, reflection coefficients.

System calibration consists of measuring light irradiance for two different path lengths. This is easily accomplished by either directing the illumination source directly into the camera as in Figure 3.6a, or illuminating and imaging a planar target with a

known reflection coefficient as illustrated in Figure 3.6b. Since the illumination source is usually fixed to the camera, the latter configuration is likely more practical and will be considered here. If the former is possible, the equations derived are still valid except there is one way travel and no reflection coefficient. Figure 3.6 depicts a setup where the image frames are grabbed by an external computer for processing. In a commercial system this can be a self contained unit.[18]

From Equation 3.15, the irradiance measured at a CCD photosite is given by:

$$E(\lambda_1, d_1) = \frac{I(\lambda_1) e^{-c(\lambda_1) d_T} \rho(\lambda_1) \cos(\gamma) filter(\lambda_1)}{\pi m^2} \left(\frac{r}{d_s + r} \right)^2 \tag{3.36}$$

where d_T is the path length traversed by the light propagating from the source via the reflector to the camera lens and d_s is the distance from the illumination source to the reflector as shown in Figure 3.6. During calibration both d_T and d_s are known. Data are collected from each CCD array (i.e. each spectral band) in the camera and the ratio of irradiance measured in two spectral bands is:

$$\frac{E(\lambda_1, d_1)}{E(\lambda_2, d_1)} = \frac{I(\lambda_1) filter(\lambda_1) e^{-c(\lambda_1) d_T} \rho(\lambda_1)}{I(\lambda_2) filter(\lambda_2) e^{-c(\lambda_2) d_T} \rho(\lambda_2)} \tag{3.37}$$

where $\rho(\lambda_1)$, and $\rho(\lambda_2)$ are also known. $E(\lambda_1, d_1)$ and $E(\lambda_2, d_1)$ are received irradiance. For convenience a white reflector may be used such that $\rho(\lambda_1) = \rho(\lambda_2) = 1$; however, in actual trials it has been found that when using a white reflector the calibration procedure is susceptible to errors from saturation. This can, of course be alleviated by decreasing illumination intensity but, for an automatic calibration procedure it may be preferable to decrease reflectance.

---

[18] For example the Canpolar VE-262 which consists of a CCD camera, frame grabber (although presently monochrome), and 486 computer all contained in a single underwater housing measuring 30.0×14.5×17.5 cm.

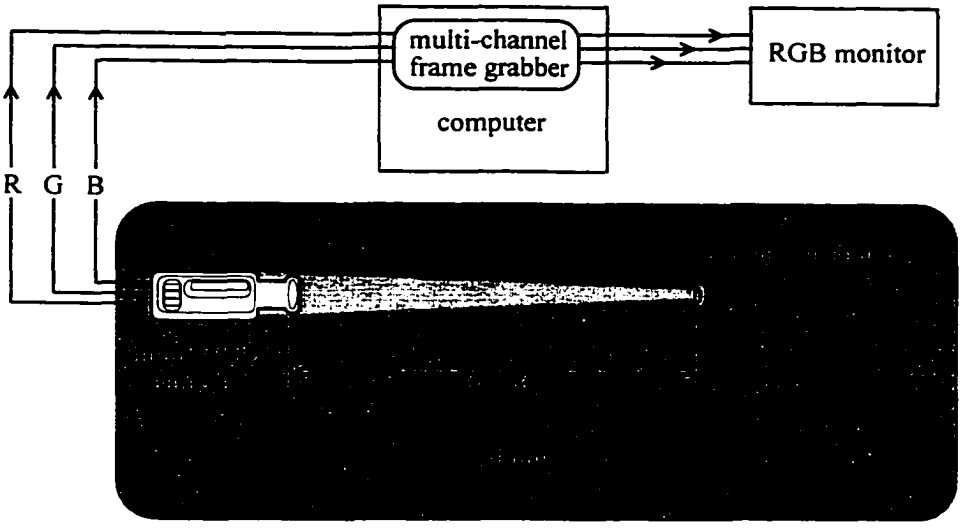

Figure 3.6a: Configuration for Direct Calibration

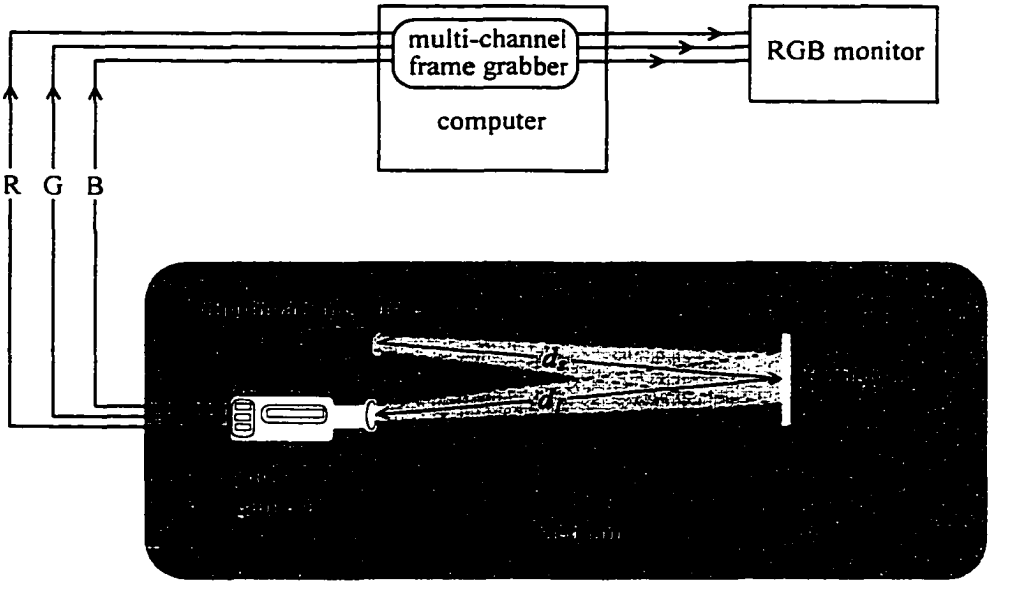

Figure 3.6b: Configuration for Calibration with Planar Target

Figure 3.6: Calibration configurations for an underwater imaging system

Changing the propagation path length by a known amount yields a second set of irradiance measures at distance d_2. For a given spectral band, the ratio of irradiances measured at d_1 and d_2 is:

$$\frac{E(\lambda_1,d_1)}{E(\lambda_1,d_2)} = e^{c(\lambda_1)(d_{T_2}-d_{T_1})}\left(\frac{d_{s_2}+r}{d_{s_1}+r}\right)^2 \tag{3.38}$$

Dividing Equation 3.38 by its counterpart in spectral band λ_2 yields:

$$\frac{E(\lambda_1,d_1)/E(\lambda_1,d_2)}{E(\lambda_2,d_1)/E(\lambda_2,d_2)} = \frac{e^{c(\lambda_1)(d_{T_2}-d_{T_1})}}{e^{c(\lambda_2)(d_{T_2}-d_{T_1})}} = e^{(c(\lambda_1)-c(\lambda_2))(d_{T_2}-d_{T_1})} \tag{3.39}$$

By rewriting Equation 3.39, the difference in attenuation coefficients $c(\lambda_1)$ and $c(\lambda_2)$ can be expressed as in Equation 3.40. Since the right hand side of the equation consists entirely of known parameters it can be solved in closed form.

$$c(\lambda_2)-c(\lambda_1) = \frac{\ln\left(\frac{E(\lambda_1,d_1)/E(\lambda_1,d_2)}{E(\lambda_2,d_1)/E(\lambda_2,d_2)}\right)}{d_{T_1}-d_{T_2}} \tag{3.40}$$

Although it is not required to compute a solution for the intensity–range transformation, the attenuation coefficient for a given spectral band can also be calculated as follows:

$$\ln\left(E(\lambda_1,d_{T_1})\right) = \ln\left(\frac{I(\lambda_1)\rho(\lambda_1)\cos(\gamma)filter(\lambda_1)}{\pi m^2}\right) + 2\ln\left(\frac{r}{d_{T_1}+r}\right) - c(\lambda_1)d_{T_1}; \tag{3.41}$$

and

$$\ln\left(E(\lambda_1,d_{T_2})\right) = \ln\left(E(\lambda_1,d_{T_1})\right) - 2\ln\left(\frac{r}{d_{T_1}+r}\right) + c(\lambda_1)d_{T_1} + 2\ln\left(\frac{r}{d_{T_2}+r}\right) - c(\lambda_1)d_{T_2}. \tag{3.42}$$

From which we calculate the spectral attenuation coefficient $c(\lambda_1)$ to be:

$$c(\lambda_1) = \frac{\ln\left(\frac{E(\lambda_1, d_{T1})}{E(\lambda_1, d_{T2})}\right) + 2\ln\left(\frac{d_{T2}+r}{d_{T1}+r}\right)}{2(d_{T2}-d_{T1})}. \tag{3.43}$$

Expressing Equation 3.37 in terms of the camera and source spectral characteristics yields:

$$\frac{I(\lambda_2)filter(\lambda_2)}{I(\lambda_1)filter(\lambda_1)} = \frac{E(\lambda_2, d_{T1})}{E(\lambda_1, d_{T1})}\frac{\rho(\lambda_1)}{\rho(\lambda_2)}e^{d_{T1}(c(\lambda_2)-c(\lambda_1))} \tag{3.44}$$

The LHS of Equation 3.44 is a system constant for two spectral bands and can be included in the range equation as a scalar. For the standard calibration reflector $\rho(\lambda_1)$ and $\rho(\lambda_2)$ are known; however, if a small portion of the surface of interest is accessible as the calibration reflector, the reflection coefficient ratio is also moved to the LHS of the equation.

The intensity–range transformation (Equation 3.35) is repeated here for convenience as Equation 3.45. For any given scene the first term of the natural logarithm in the numerator is the ratio of measured intensities, the second term is found from the calibration procedure by Equation 3.44, and the final term is the ratio of reflection coefficients which may be known *a priori* or found by other means (Section 4.2.1). The difference in attenuation coefficients in the denominator is found during calibration with Equation (3.40).

$$d_T = \frac{\ln\left(\frac{E(\lambda_1)}{E(\lambda_2)}\cdot\frac{I(\lambda_2)filter(\lambda_2)}{I(\lambda_1)filter(\lambda_1)}\cdot\frac{\rho(\lambda_2)}{\rho(\lambda_1)}\right)}{(c(\lambda_2)-c(\lambda_1))} \tag{3.45}$$

Representing the *constants* in the imaging system as U and V, the range computation can be written as:

$$d_T = \frac{\ln\left(\frac{E(\lambda_1)}{E(\lambda_2)} \cdot \mathrm{U}\right)}{\mathrm{V}} \tag{3.46}$$

$$\text{where} \quad \mathrm{U} = \frac{I(\lambda_2)\,filter(\lambda_2)}{I(\lambda_1)\,filter(\lambda_1)} \cdot \frac{\rho(\lambda_2)}{\rho(\lambda_1)} \tag{3.47}$$

$$\text{and} \quad \mathrm{V} = \left(c(\lambda_2) - c(\lambda_1)\right). \tag{3.48}$$

Equation 3.46 demonstrates the computational efficiency of the algorithm[19]. Since U and V need only be calculated once for given operating conditions the transformation from two intensity measurements to a range estimate requires only three floating point operations (two divisions, one multiplication) and one transcendental function call.

Depending on the region of operation, the spectral attenuation of water may remain constant over very large areas or it may vary over tens of meters. Oceanic data indicate that any local variation (differences measured within a few meters) in attenuation coefficient is typically characterized by a fairly consistent change across the entire spectrum [29] such that the attenuation coefficient versus wavelength curve moves "up" or "down" but retains its shape and slope. Since, as discussed in Chapter 2, total scattering is predominantly independent of wavelength, such an effect may be attributed

---

[19] Note also that, substituting Eqn. 3.44 into 3.45 eliminates the reflection coefficients for a given surface:

$d = \dfrac{\ln\left(\frac{E(\lambda_1)}{E(\lambda_1)}\frac{E(\lambda_2, d_{T1})}{E(\lambda_1, d_{T1})} e^{d_1(c(\lambda_2)-c(\lambda_1))}\right)}{2(c(\lambda_2)-c(\lambda_1))}$. This ratio is accounted for in the term, $E(\lambda_2, d_1)/E(\lambda_1, d_1)$; however, this presupposes that the calibration and test surfaces are the same hue.

to changes in the scattering coefficient while the absorption coefficient remains constant. The equation for range derived here depends on the difference in attenuation coefficients; therefore, a uniform shift of the entire attenuation curve does not affect calibration constants. However if desired, calibration may continue to be monitored by positioning a calibration target such that it continually reflects onto a small portion of the camera's image plane. The spectral difference in attenuation coefficients can then be continually updated with Equation 3.49.

$$c(\lambda_2) - c(\lambda_1) = \frac{\ln\left(\frac{E(\lambda_1)}{E(\lambda_2)}U\right)}{d_T} \tag{3.49}$$

3.2 Numeric Example

The following numeric example demonstrates implementation of the derived transformation. Consider a system utilizing two spectral bands with the following specifications:

Illumination Source:	lens diameter (A_o)	0.0500 m
	radiant flux (F)	500.0 W constant across the spectrum
	beam width (Ω)	0.0800 sr
Calibration Target	$\rho(\lambda_1)$	0.9000
	$\rho(\lambda_2)$	0.8000
Camera	*filter* (λ_1)	.9500
	filter (λ_2)	.9200
	m	1.000 (parallel projection)

Medium	$c(\lambda_1)$	0.0620 (Jerlov Type II @ λ = 475 nm)
	$c(\lambda_2)$	0.5800 (Jerlov Type II @ λ = 700 nm)

Hence, the radiant intensity of the source is:

$$I = \frac{F}{\Omega} = \frac{500.0\,W}{0.0800\,sr} = 6250\,{}^{W}/_{sr};$$

and the effective radius is:

$$r_o = \sqrt{\frac{A}{\Omega}} = \sqrt{\frac{0.0500^2\,\pi}{0.0800}} = 0.3133$$

During this calibration procedure, the following irradiance is measured in two spectral bands[20] (assume $\gamma = 0^o$):

at 0.5 m: $$E(\lambda_1,1) = \frac{6250e^{-0.06200}\,0.9000\cdot 0.9500}{\pi}\left(\frac{0.3133}{0.5000+0.3133}\right)^2 = 237.0\,{}^{W}/_{m^2}$$

$$E(\lambda_2,1) = 121.5\,{}^{W}/_{m^2}$$

at 1.0 m $$E(\lambda_1,2) = 85.39\,{}^{W}/_{m^2}$$

$$E(\lambda_2,2) = 26.08\,{}^{W}/_{m^2}$$

Calibration Computation:

From Equation 3.40;

$$c(\lambda_2) - c(\lambda_1) = \frac{\ln\left(\frac{E(\lambda_1,d_1)/E(\lambda_1,d_2)}{E(\lambda_2,d_1)/E(\lambda_2,d_2)}\right)}{d_{T_1} - d_{T_2}} = \frac{\ln\left(\frac{237.0/85.39}{121.5/26.08}\right)}{1.000-2.000} = 0.5175$$

---

[20] From Eqn. 3.15

From Equation 3.28;

$$\frac{I(\lambda_2)filter(\lambda_2)}{I(\lambda_1)filter(\lambda_1)} = \frac{E(\lambda_2, d_{T1})}{E(\lambda_1, d_{T1})} \frac{\rho(\lambda_1)}{\rho(\lambda_2)} e^{d_{T1}(c(\lambda_2)-c(\lambda_1))} = \frac{121.5 \cdot 0.9000}{237.0 \cdot 0.8000} e^{0.5175} = 0.9677$$

Test Surface:

Given a test surface at a distance of 3.350 m oriented an angle of 6° with $\rho(\lambda_1) = 0.7200$ and $\rho(\lambda_2) = 0.9300$, the following irradiances would be measured in the two spectral bands:

$$E(\lambda_1) = \frac{6250 e^{-0.0620(6.700)} 0.7200 \cos(6.0) 0.9500}{\pi} \left(\frac{0.3133}{3.350 + 0.3133} \right)^2 = 6.522$$

$$E(\lambda_2) = 0.2540$$

Range Calculation:

Substituting the results from the calibration and the measured spectral irradiances (above) into Equation 3.29 yields the following estimate of range:

$$\hat{d} = \frac{\ln\left(\frac{E(\lambda_1)}{E(\lambda_2)} \cdot \frac{I(\lambda_2)filter(\lambda_2)}{I(\lambda_1)filter(\lambda_1)} \cdot \frac{\rho(\lambda_2)}{\rho(\lambda_1)} \right)}{2(c(\lambda_2) - c(\lambda_1))} = \frac{\ln\left(\frac{6.522}{0.2540} \cdot 0.9677 \cdot \frac{0.9300}{0.7200} \right)}{2(0.5175)} = 3.350 \text{ m.}$$

This example serves to demonstrate how the intensity–range transformation is implemented. It confirms that a closed form solution for range is possible but does not provide insight into the sensitivity or accuracy of the approach in the presence of interference and scattering. These issues are considered in the subsequent chapters.

3.3 Image Examples

This Chapter concludes with examples of range derivation from actual images. The images were acquired in a test tank with a 3-chip RGB camera and associated frame grabber. Figure 3.7a is a photograph of the test facility prior to being filled with water. The camera is contained in the aluminum cylinder shown in a frontal view in Figure 3.7b (with the lexan cover removed).

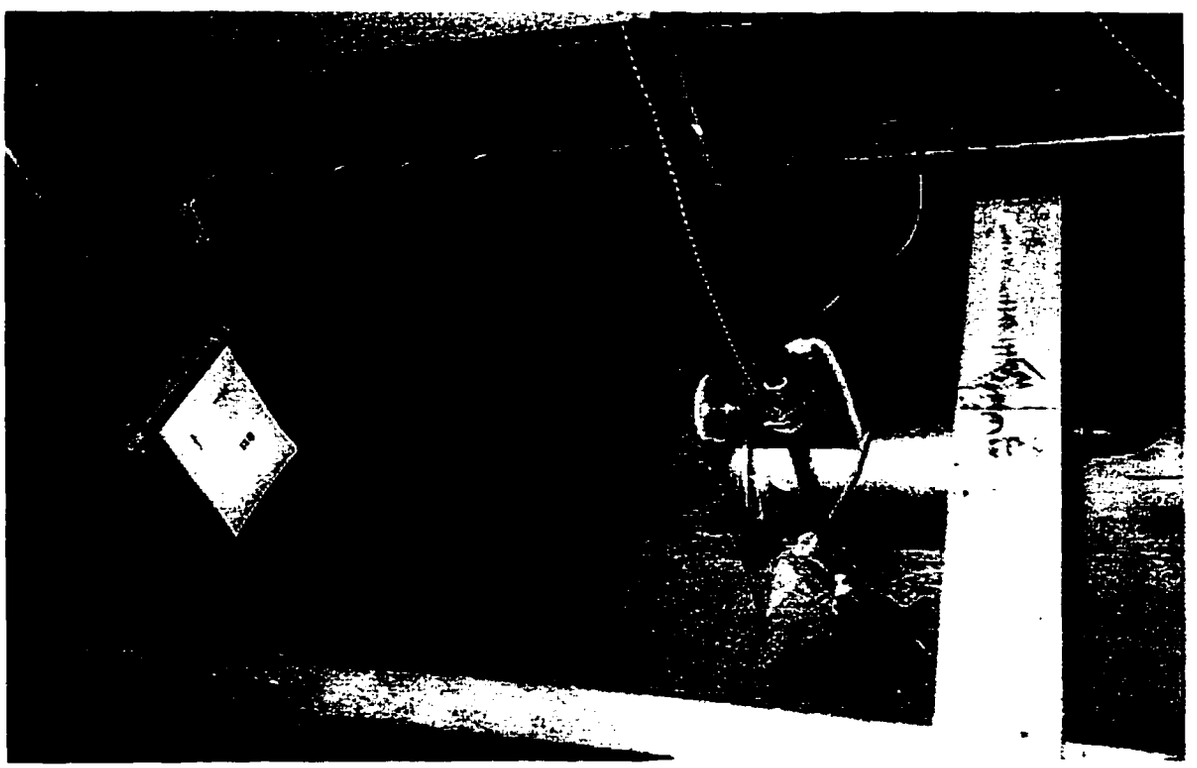

Figure 3.7a: Test tank

Figure 3.7b: Test camera

Figure 3.7: Test facility for example images

A calibration procedure was performed as described in Section 3.1.2 at:

$$d_{T_1} = 1.010 \text{ m}$$
$$d_{T_2} = 2.080 \text{ m}$$

yielding the following differences in attenuation coefficients:

c(red) - c(green)	0.034;
c(red) - c(blue)	-0.234;
c(blue) - c(green)	0.268.

where the "red" "green" and "blue spectral bands correspond to the R, G, and B channels of the camera. The calibration plate was repositioned within the tank to a range of 0.800 m and using the calibration data, the following estimates were made:

colour spectrums	**mean estimate**	**variance**	**% error**
green/red	0.812	0.1129	1.50 %
blue/red	0.807	0.0056	0.88 %
green/blue	0.806	0.0056	0.75 %

These results confirm valid calibration data and demonstrate correct range estimation capability for the vision system. They also indicate that estimation accuracy is proportional to the difference in attenuation coefficients as seen previously.

Figures 3.8, 3.9 and 3.10 illustrate the results using the intensity–range transformation on real images of underwater objects. Preprocessing the data consisted of applying an 3×3 neighborhood averaging for rudimentary smoothing, and thresholding or segmenting. Each image illustrates different preprocessing approaches. In the first image a lower threshold was used to discern the object from the "open water" behind it. In the second image an object is on the seabed and segmentation was used. The intensity–range transformation is then applied to both segmented image components and the resultant range maps are "reassembled". The final image is partially affected by saturation and both upper and lower thresholds are used. To clearly demonstrate the performance of the intensity–range transformation, the three-dimensional range data plotted in the figures are the "raw" transformation output with no attempts to enhance appearance of the outputs through techniques such as surface fitting. Post-processing was used on the data from the third (Figure 3.10) image.

These results are presented to illustrate practical implementation of the algorithm. The performance that can be inferred from these results is below the performance that

should be expected from a more optimal system where the spectral bands are narrower and greater differences in attenuation coefficients can be exploited. Analysis of system performance is conducted in Chapters 4 and 5.

Figure 3.8a is an intensity image of a 0.26 m diameter pipe taken underwater at a range of 0.90 m. Figure 3.8b is a plot of the red, green and blue intensities across row 250 of the image. The peaks approximately between pixels 180 and 200 are due to the slight specular reflection as seen in the image. An advantage of using intensity ratios is that such characteristics are constant across all spectral bands, hence may be cancelled out. Figure 3.8c is the range-map from the intensity–range transformation using the green and blue channels.

Figure 3.9a is an enhanced image of an 11 cm reddish-brown metal ball laying on a sandy bottom at a closest range of 0.42 m. Figure 3.9b is a plot of the intensities in each spectral band and again one can see how using ratios normalize many of the intensity variations. Instead of thresholding in this case, the blue and green intensities were used to segment the ball from the sand and two separate range transformations were performed. The complete range map is shown in Figure 3.9c. The vertical "banding" apparent in the image was not completely removed by the algorithms and appears in the range plot as creases in the scene. The range map was generated using the red and blue spectral bands.

Figure 3.10a is an enhanced image of an 0.115 m ring taken at a range of 0.50 m. In the interior of the ring is a white disk and there is a 1.3×1.3 cm gray-white square on the lower right of the ring. The former is saturated in at least one of the spectral bands. The upper right quadrant of the image illustrates specular reflection from the ring surface. A plot of the intensities received across row 80 of the image is given in Figure 3.10b.

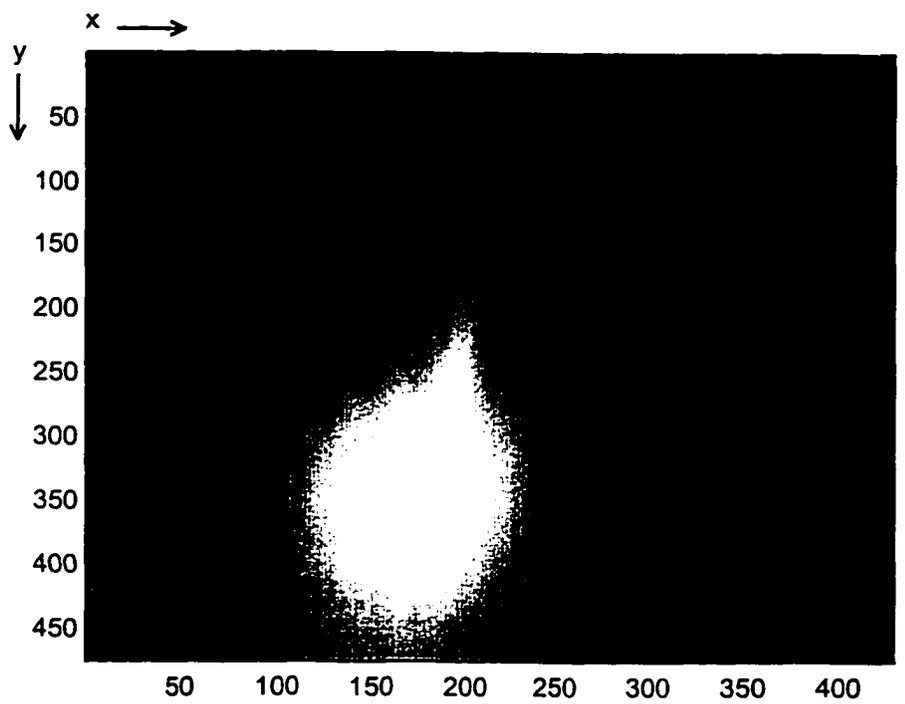

Figure 3.8a: Contrast enhanced image of pipe

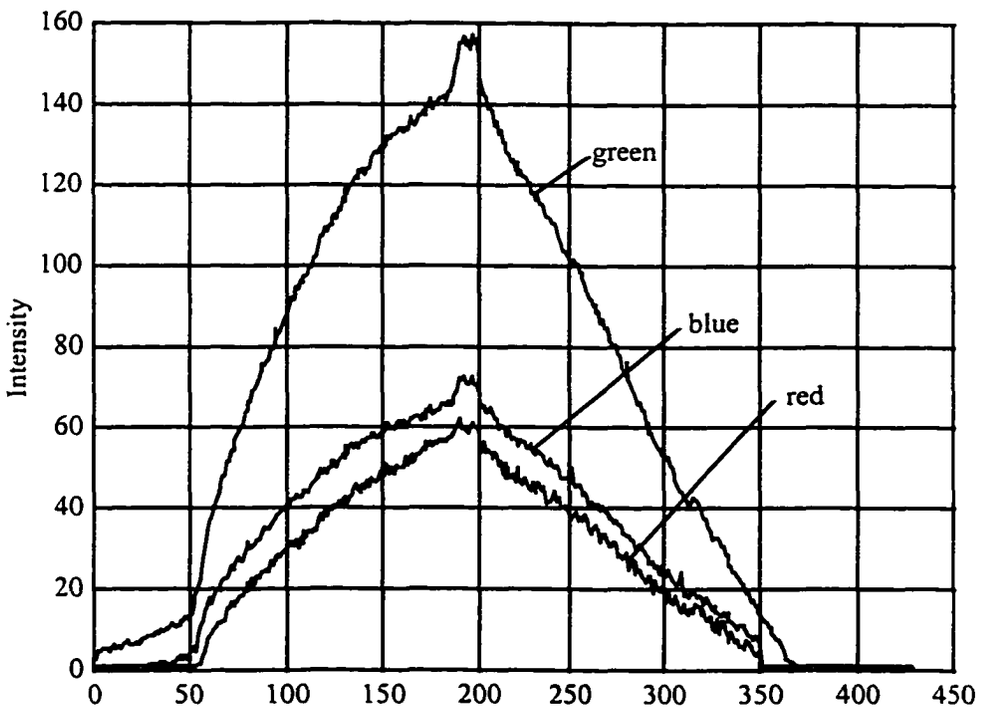

Fig. 3.8b: Intensity plot

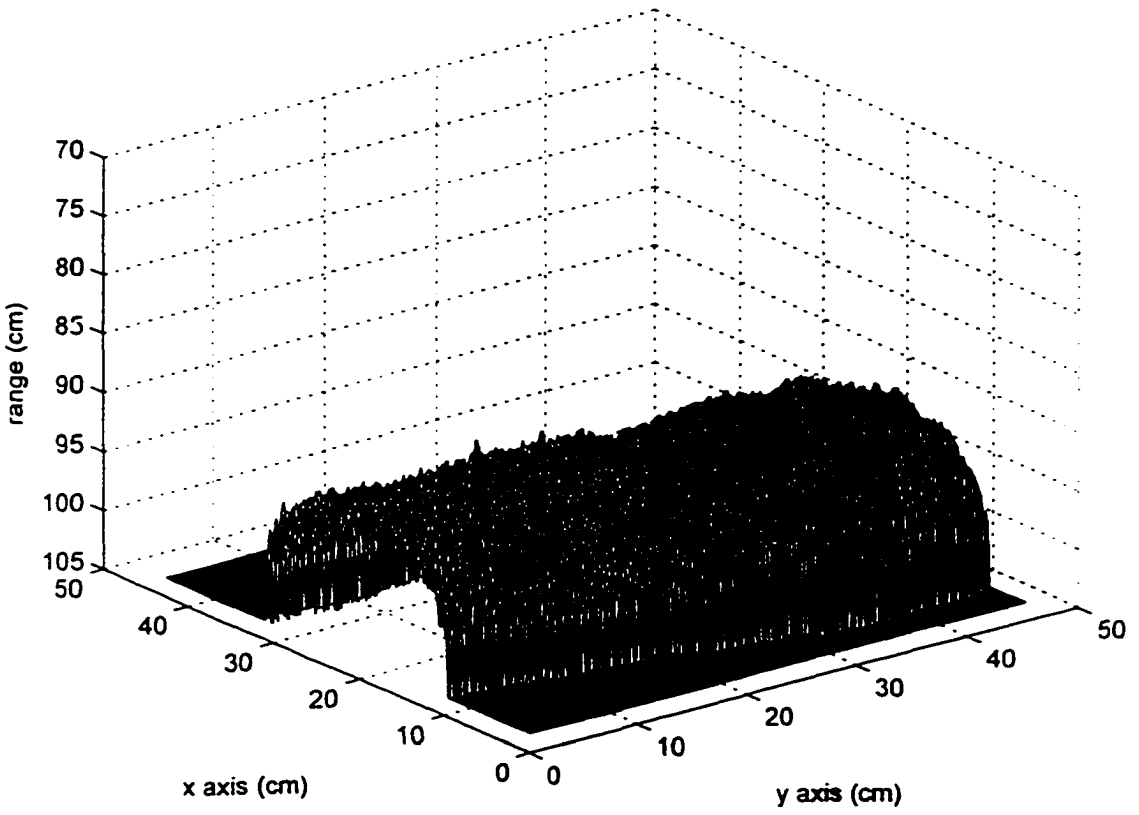

Figure 3.8c: Range image for 0.26 m pipe

Figure 3.8: Data for underwater pipe

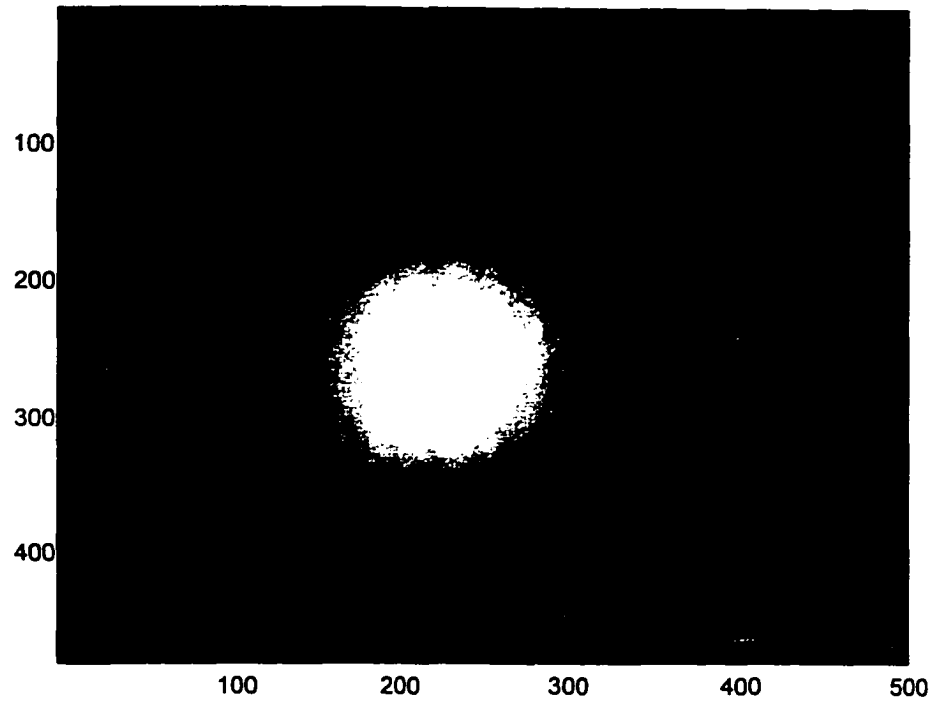

Figure 3.9a: Contrast enhanced image of ball on seabed

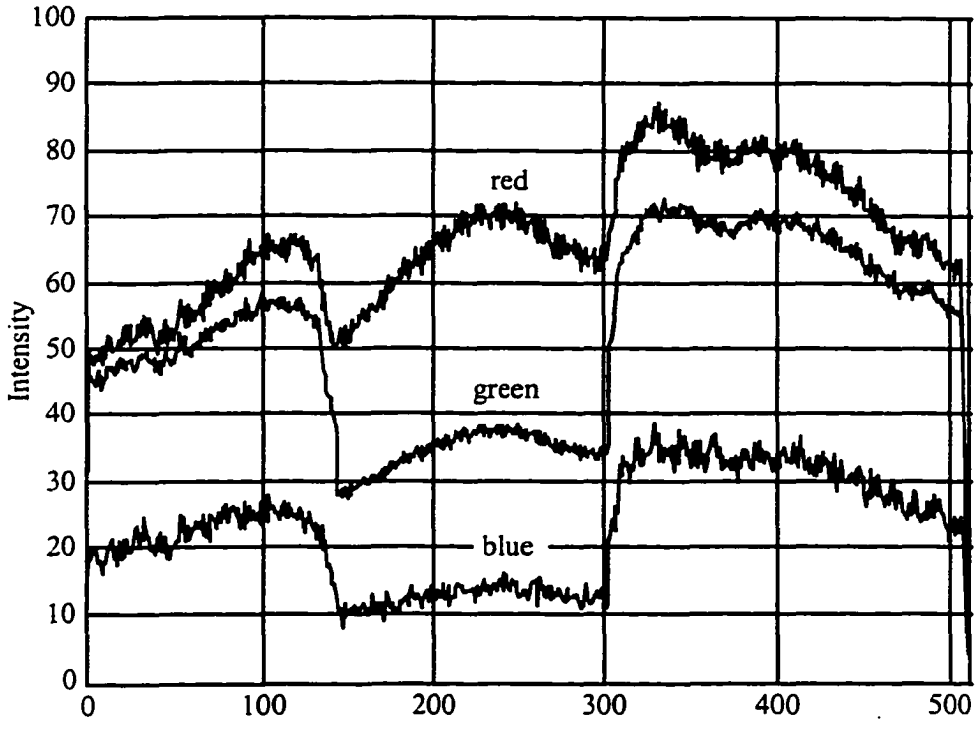

Fig. 3.9b: Intensity plot

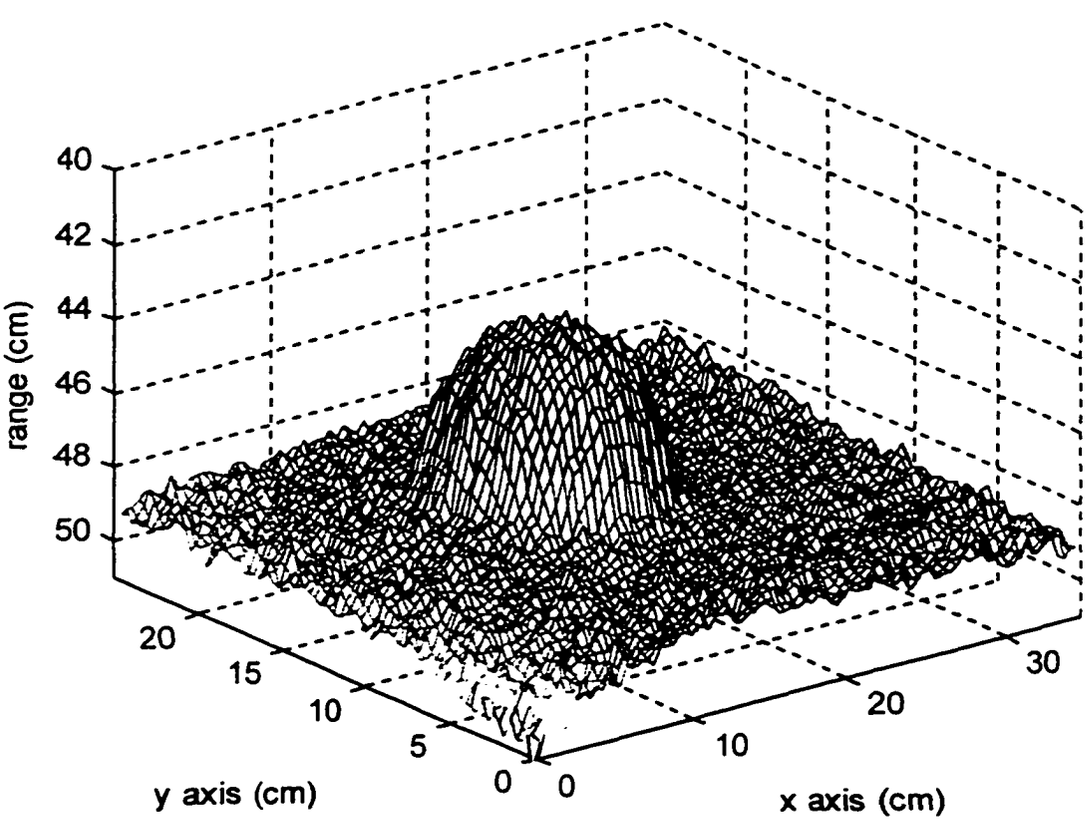

Figure 3.9c: Range image for ball

Figure 3.9: Data for ball on a sea bed

It is speculated that the high spatial frequency intensity variations are due to variation in incidence angle for the multifaceted ring surface.

Upper (255) and lower (7) thresholds were set to discount data suspected of being invalid. In addition, when the intensity–range algorithm was envoked, a partial circle of outliers appeared around the outer edge of the ring in the range map. These encircled approximately 3/4 of the ring including the two upper and lower right quadrants. In this case, post processing was employed to mask the outliers and smooth the remaining range data. The pixels containing the outliers were set to the mean range of their eight neighbors. The resulting range plot using the green and blue spectral data is given in Figure 3.10c. In this instance the specular reflection causes slight deterioration in the range map; up to 0.05 m estimate error. This could be minimized with a more diffuse illumination source, or an adaptive system could reduce source intensity or camera gain. For these tests, all compensation techniques such as gamma correction and an automatic iris adjusment were disabled.

The ring was chosen to represent a docking collar for an underwater vehicle. In that instance, a reasonably competent system could match the range data to a stored model of the collar with a high correlation and proceed with docking (recognizing that the saturated regions of the image represented potential obstacles).

This chapter derived the intensity-range transformation and a calibration process to extract the required system and medium parameters. It also demonstrated the algorithms in an actual vision system. Chapters 4 and 5 provide a quantitative analysis of algorithm performance.

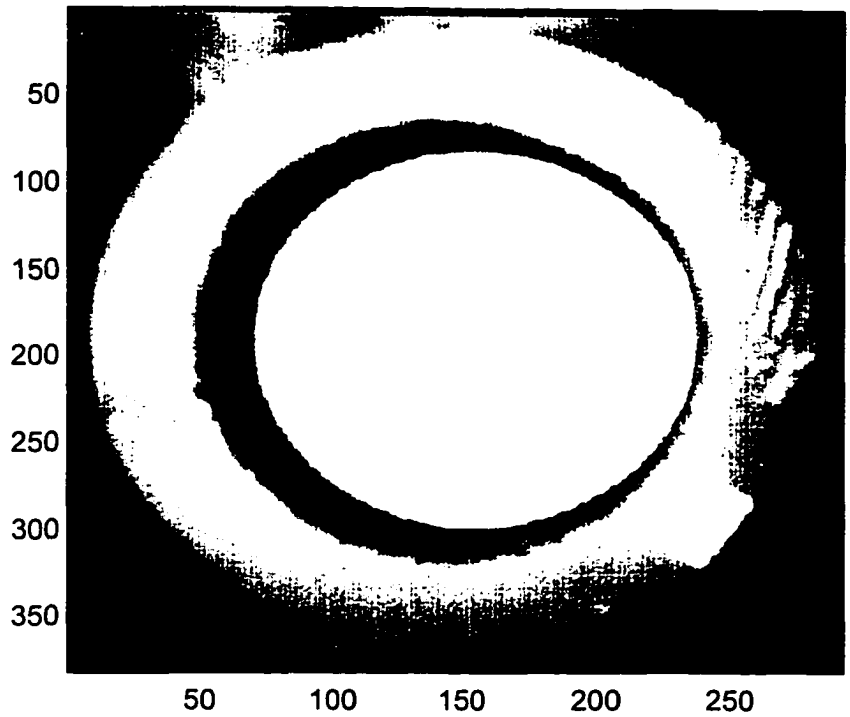

Figure 3.10a: Image of ring

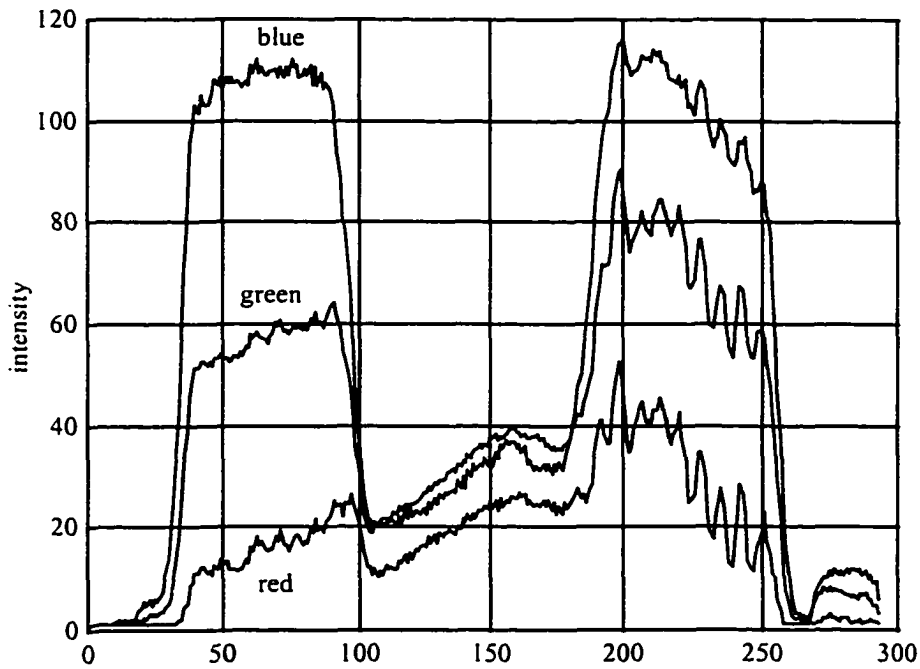

Fig. 3.10b: Intensity plot for row 80

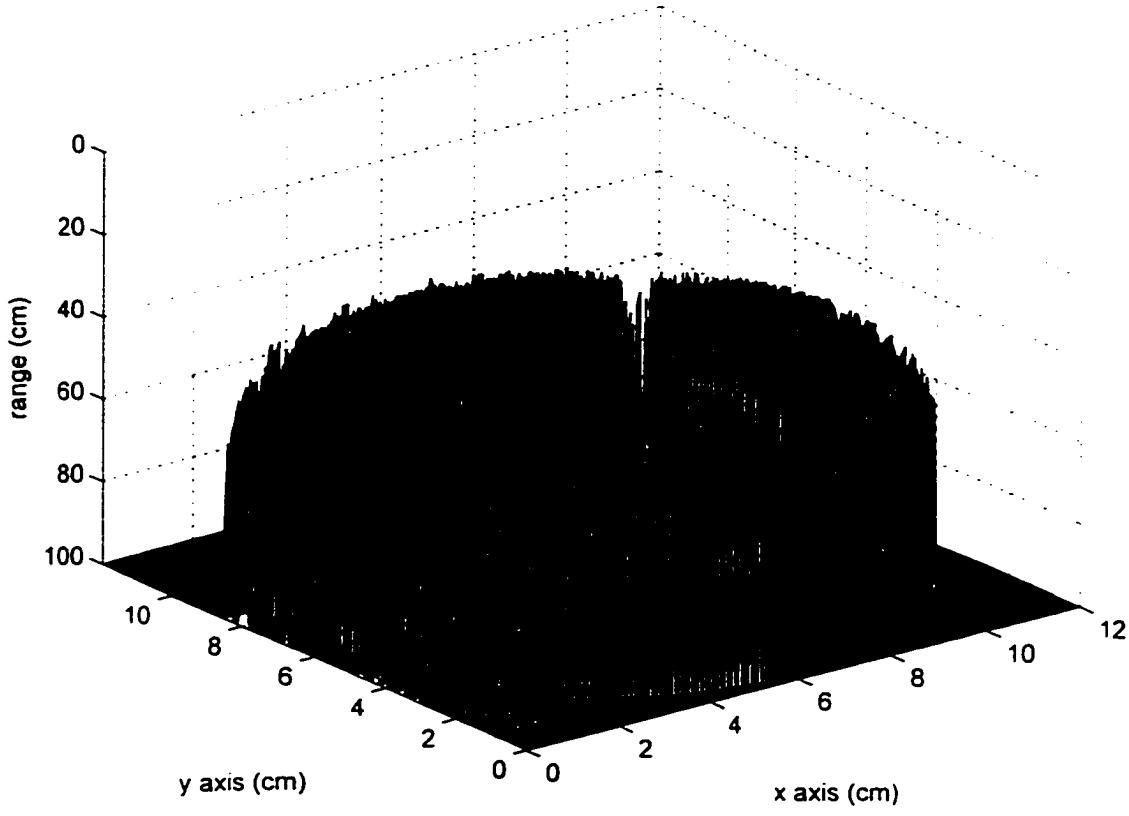

Figure 3.10c: Range image for ring

Figure 3.10: Data for underwater collar or ring

Chapter 4

Analytic Analysis and Implementation

4.0 Introduction

In the previous section, a transformation was derived for converting standard intensity images received from a scene in different spectral bands, into a single range image or three dimensional representation of the imaged environment. In practice, the variables used in that transformation are based on measured parameters hence are subject to measurement error. Due to the mathematically untractable nature of light propagation underwater, scattering and blurring effects in particular, researchers rely on simulation techniques to analyze the effects of noise, uncertainty and other perturbations in subsea imaging systems [20, 24, 27, 28, 29, 30]. That is the subject of the next Chapter. In this Chapter scattering is assumed insignificant (beyond its contribution to attenuation) and further insight and understanding is gained from considering the effects of noise on the intensity–range transformation, and the sensitivity of range calculations to inaccuracies in the *independent* (medium and scene) parameters.

Although the complexity of water as a conductor of light energy dictates that simulation techniques be used for complete, quantifiable performance analysis, the parametric analysis in Sections 4.1 and 4.2 provide useful insight into the sensitivities and error propagation inherent in the transformation. Section 4.3 further develops the concept

and addresses implementation considerations, particularly that of incorporating more than two spectral measurements into the range estimates.

4.1 Estimate Probability Distribution

A machine vision system exploiting the developments of this thesis will most likely consist of a CCD camera followed by a frame grabber. Resulting digital images will be two dimensional functions of the form $g(i,j)$ where both the domain and range are quantized such that $0 < i$, $0 < j$, and $0 < g(i,j) \leq 256$ for 8-bit digitization (per spectral band). The non-quantized value of $g(i,j)$ that will be measured within a given pixel is given by

$$E = T\int_{\lambda_o}^{\lambda_f} E(\lambda)q(\lambda)d\lambda \tag{4.1}$$

where T is integration time (inverse of shutter speed), $E(\lambda)$ is radiance over the pixel area, and $q(\lambda)$ is the quantum efficiency of the photosite. In any practical system this measurement is corrupted by noise such that the corresponding pixel value output from the frame grabber is [98]:

$$\hat{E}(i,j) = A\left(E(i,j) + N_S + N_D + N_R\right) + N_Q \tag{4.2}$$

where: N_S is shot noise inherent in CCD devices;

N_D is noise due to "dark currents" similar to thermal noise;

N_R is noise from the on-chip amplifier that transforms photosite charge to voltage;

N_Q is analog-to-digital converter quantization noise;

A is camera gain.

Another machine vision noise that should be identified is *fixed pattern noise* resulting from CCD fabrication errors that cause slight variations in the transfer function of each photosite across a CCD array. With reference to Equation 4.1, the output from any photosite within a uniformly irradiated array is given by:

$$E(x,y) = K(x,y)T\int I(\lambda)q(\lambda)d\lambda \tag{4.3}$$

where K is a random variable with a mean of 1 and (normally) a very small variance. If the non-uniformity across the array is significant, it can be accounted for in the calibration procedure described previously and stored as a quantum efficiency lookup table, or map for each array. A preferred approach is to use a better quality camera.

The probability distribution of total measurement noise, that is the noise added to E, depends on which noise is dominant. This in turn is dependent on system electronics and irradiance level. Measurements and heuristic arguments presented in the literature typically show this distribution ranging from Poisson to Gaussian. Uniform noise, which would be predominant if N_Q were dominant [98], has also been used in analysis. Typically, at low irradiance levels, shot noise dominates and the probability density function (pdf) is close to a Poisson function. As irradiance increases other noise dominates and the pdf changes [99].

The intensity-range transformation derived in Chapter 3 can be rewritten as:

$$\hat{d} = \frac{\ln\left(\frac{\hat{E}(\lambda_1)}{\hat{E}(\lambda_2)} \cdot \frac{I(\lambda_2)filter(\lambda_2)}{I(\lambda_1)filter(\lambda_1)} \cdot \frac{\rho(\lambda_2)}{\rho(\lambda_1)}\right)}{2\left(c(\lambda_2) - c(\lambda_1)\right)} \tag{4.4}$$

$$= \frac{\ln\left(\hat{E}(\lambda_1)\right) - \ln\left(\hat{E}(\lambda_2)\right) + \ln(U)}{V}. \tag{4.5}$$

where $\hat{d}$ is now the value of a random variable, and U and V are computed in Eqns. 3.47 and 3.48. The pdf of $\ln\left(\hat{E}(\lambda_n)\right)$ is found from the nonlinear transformation:

$$x = \ln(y) \tag{4.6}$$

(where the substitution $y = \hat{E}(\lambda_n)$ is used for notational convenience). Since $y > 0$, $\ln(y)$ exists and represents a continuous, monotonic transformation of $\hat{E}(\lambda_n)$ such that the resultant pdf, $f_X(x)$, is given by [100]:

$$f_X(x) = f_Y(y)\frac{dy}{dx} \tag{4.7}$$

If the noise associated with $\hat{E}(\lambda_n)$ is assumed Gaussian, than

$$f_Y(y) = \frac{1}{\sigma_y\sqrt{2\pi}} e^{\frac{-(y-\mu_y)^2}{2\sigma_y^2}}, \tag{4.8}$$

a Gaussian distributed random variable. Also:

$$\frac{dy}{dx} = \frac{de^x}{dx} = e^x. \tag{4.9}$$

Hence, $f_X(x) = f_X\left(\ln(y)\right) = \frac{1}{\sigma_y\sqrt{2\pi}} e^{\frac{-(e^x-\mu_y)^2}{2\sigma_y^2}} e^x$

$$= \frac{1}{\sqrt{2\pi e^{-2x}\sigma_y^2}} e^{\frac{-(1-e^{-x}\mu_y)^2}{2e^{-2x}\sigma_y^2}}. \tag{4.10}$$

Typically, the camera will be adjusted to maximize the signal level without saturating the CCD. In this region, where $y = \hat{E}(\lambda) \geq 10$, the transformation becomes somewhat linear and the pdf in Equation 4.10 approximates a Gaussian density function with:

$$\mu_x = \ln(\mu_y), \tag{4.11 a}$$

and

$$\sigma_x^2 = e^{-2\ln(\mu_y)}\sigma_y^2. \tag{4.11 b}$$

This is illustrated in Figures 4.1 a and b for $\mu_y = 10$ and $\mu_y = 100$.

Although the Gaussian pdf assumption seems reasonable for values of $\hat{E}(\lambda) >> 1$, in situations with low scene reflectance, high attenuation coefficients and/or long range, the quantized irradiance output from a photosite may not be considerably greater than unity. Although occurrences are expected to be few, the Gaussian pdf assumption is no longer adequate since it may imply

$$\hat{E}(\lambda_n) \leq 0,$$

which can not exist. For this analysis $\hat{E}(\lambda)$ is considered to be log-normal distributed yielding a Gaussian pdf for $\ln(\hat{E}(\lambda))$ when $\hat{E}(\lambda) >> 1$ as above, and an approximated Poisson pdf (resulting from shot noise) when $\hat{E}(\lambda)$ is closer to unity. This represents a compromise between the Poisson and Gaussian distributed noise which is characteristic of CCD arrays.

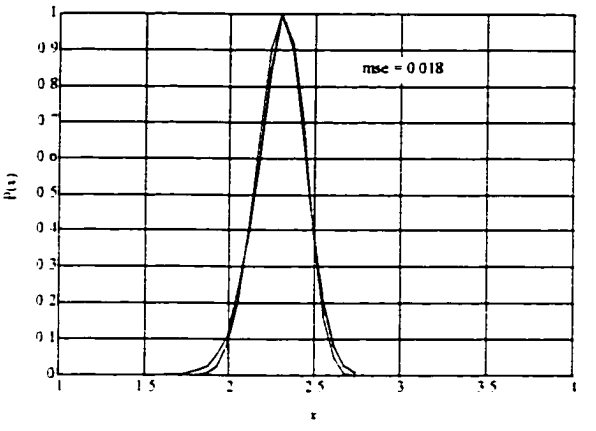

Figure 4.1a: Actual and approximated pdf for $x = \ln(y)$, $\mu_y = 10$

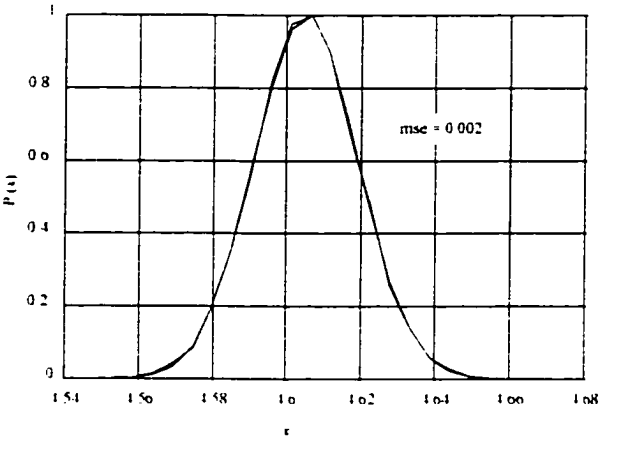

Figure 4.1b: actual and approximated pdf for $x = \ln(y)$, $\mu_y = 100$

Figure 4.1: Actual and approximated pdf for $x = \ln(y)$

A log-normal pdf is described by:

$$f_Y(y) = \frac{1}{y\sigma_x\sqrt{2\pi}} e^{\frac{-(\ln(y)-\mu_x)^2}{2\sigma_x^2}} \tag{4.12}$$

and from Eqn. 4.7 the pdf resulting from the transformation $x = \ln(y)$ is the Gaussian pdf:

$$f_X(x) = \frac{1}{\sigma_x \sqrt{2\pi}} e^{\frac{-(x-\mu_x)^2}{2\sigma_x^2}} . \tag{4.13}$$

Substituting $\ln\left(\hat{E}(\lambda_i)\right)$ for x_i yields:

$$f_{E(\lambda_1)}\left(\ln\left(\hat{E}(\lambda_1)\right)\right) = \frac{1}{\sqrt{2\pi\sigma^2_{\ln(\hat{E}(\lambda_1))}}} e^{\frac{-\ln(\hat{E}(\lambda_1))-\mu_{\ln(\hat{E}(\lambda_1))}}{2\sigma^2_{\ln(\hat{E}(\lambda_1))}}} \tag{4.14a}$$

and

$$f_{E(\lambda_2)}\left(\ln\left(\hat{E}(\lambda_2)\right)\right) = \frac{1}{\sqrt{2\pi\sigma^2_{\ln(\hat{E}(\lambda_2))}}} e^{\frac{-\ln(\hat{E}(\lambda_2))-\mu_{\ln(\hat{E}(\lambda_2))}}{2\sigma^2_{\ln(\hat{E}(\lambda_2))}}} . \tag{4.14b}$$

Given that $\ln\left(\hat{E}(\lambda_1)\right)$ and $\ln\left(\hat{E}(\lambda_2)\right)$ are independent Gaussian random variables, it would be instructive to know the resultant pdf of $\hat{d}$. This can be found from the joint density function of $\ln\left(\hat{E}(\lambda_1)\right)$ and $\ln\left(\hat{E}(\lambda_2)\right)$ with Equation 4.4 rewritten as:

$$V\hat{d} - \ln(U) = \hat{G} = \ln\left(\hat{E}(\lambda_1)\right) - \ln\left(\hat{E}(\lambda_2)\right) = x_1 - x_2 . \tag{4.15}$$

Using an approach similar to that found in [100] the probability distribution, hence the pdf of $\hat{G}$, is as follows:

$$\begin{aligned} F_G(\hat{G}) &= P\left\{x_1 - x_2 \le \hat{d}\right\} \\ &= \int_{-\infty}^{\infty} \int_{-\infty}^{\hat{d}-x_2} f_{x_1 x_2}(x_1, x_2)\, dx_1\, dx_2 \end{aligned} \tag{4.16}$$

and, because x_1 and x_2 are independent:

$$F_G(\hat{G}) = \int_{-\infty}^{\infty} f_{x_2}(x_2) \int_{-\infty}^{\hat{G}-x_2} f_{x_1}(x_1)\, dx_1\, dx_2 . \tag{4.17}$$

Using Leibniz's Rule in differentiating Equation 4.17 to find the pdf yields:

$$f_G(\hat{G}) = \frac{dF_G(\hat{G})}{d\hat{G}} = \int_{-\infty}^{\infty} f_{x_2}(x_2)\left[f_{x_1}(\hat{G}+x_2)\frac{d(\hat{G}+x_2)}{d\hat{G}} + \int_{-\infty}^{\hat{G}-x_2} \frac{\partial f_{x_1}(x_1)}{\partial \hat{G}} dx_1 \right] dx_2$$

$$= \int_{-\infty}^{\infty} f_{x_2}(x_2) f_{x_1}(\hat{G}+x_2) dx_2 \qquad (4.18)$$

Substituting Equation 4.14 into Equation 4.18:

$$f_G(\hat{G}) = \frac{1}{2\pi\sigma_1\sigma_2} \int_{-\infty}^{\infty} e^{\frac{(\hat{G}-x_2-\mu_1)^2}{2\sigma_1^2}} e^{\frac{(x_2-\mu_2)^2}{2\sigma_2^2}} dx_2 . \qquad (4.19)$$

where $\mu_1 = \mu_{\ln(\hat{E}(\lambda_1))}$

$\mu_2 = \mu_{\ln(\hat{E}(\lambda_2))}$

$\sigma_1^2 = \sigma^2_{\ln(\hat{E}(\lambda_1))}$

$\sigma_2^2 = \sigma^2_{\ln(\hat{E}(\lambda_2))}$

Larson and Shubert [101] showed that the exponent in the integrand can be rewritten as:

$$\exp\left(-\frac{(\hat{G}-x_2-\mu_1)^2}{2\sigma_1^2} - \frac{(x_2-\mu_2)^2}{2\sigma_2^2} \right)$$

$$= \exp\left(-\frac{\left(\hat{G}-(\mu_1-\mu_2)\right)^2}{2(\sigma_1^2+\sigma_2^2)} - \frac{\sigma_1^2+\sigma_2^2}{\sigma_1^2\sigma_2^2}\left(x_2 - \frac{\sigma_2^2(\mu_1-\hat{G})+\mu_2\sigma_1^2}{\sigma_1^2+\sigma_2^2} \right)^2 \right). \qquad (4.20)$$

Let $p = x_2 - \dfrac{\sigma_2^2(\mu_1-\hat{G})+\mu_2\sigma_1^2}{\sigma_1^2+\sigma_2^2}$ such that $\dfrac{dp}{dx_2} = 1$,

and let $s = \dfrac{\sqrt{\sigma_1^2+\sigma_2^2}}{\sigma_1\sigma_2}$.

Now Equation 4.19 can be written as:

$$f_G(\hat{G}) = \frac{1}{2\pi\sigma_1\sigma_2}\exp\left(-\frac{\left(\hat{G}-(\mu_1-\mu_2)\right)^2}{2(\sigma_1^2+\sigma_2^2)}\right)\int_{-\infty}^{\infty}\exp\left(-\frac{(sp)^2}{2}\right)dp \tag{4.21}$$

and the integrand now resembles the form of the *standard normal density function* [102]

$$\frac{1}{\sqrt{2\pi}}\exp\left(-\frac{z^2}{2}\right), \tag{4.22}$$

and

$$\int_{-\infty}^{\infty}\frac{1}{\sqrt{2\pi}}\exp\left(-\frac{z^2}{2}\right) = 1.$$

Substituting $z = sp$, and $\frac{dz}{dp} = s$ into the integral in Equation 4.21 yields

$$\int_{-\infty}^{\infty}\exp\left(-\frac{(sp)^2}{2}\right)dp = \frac{1}{s}\int_{-\infty}^{\infty}\exp\left(-\frac{z^2}{2}\right)dz = \sqrt{2\pi}\,\frac{\sigma_1\sigma_2}{\sqrt{\sigma_1^2+\sigma_2^2}}. \tag{4.23}$$

So the pdf in Equation 4.18 is:

$$f_G(\hat{G}) = \frac{1}{\sqrt{2\pi(\sigma_1^2+\sigma_2^2)}}\exp\left(-\frac{\left(\hat{G}-(\mu_1-\mu_2)\right)^2}{2(\sigma_1^2+\sigma_2^2)}\right). \tag{4.24}$$

Which is a Gaussian pdf with mean $(\mu_1-\mu_2)$ and variance $(\sigma_1^2+\sigma_2^2)$. Finally, rewriting Equation 4.15 for $\hat{d}$ yields

$$\hat{d} = \frac{\hat{G}+\ln(U)}{V} \tag{4.25}$$

which is a linear transformation with mean,

$$u_{\hat{d}} = \frac{\left(\mu_{\ln(\hat{E}(\lambda_1))}-\mu_{\ln(\hat{E}(\lambda_2))}\right)+\ln(U)}{V} \tag{4.26}$$

and variance

$$\sigma_{\hat{d}}^2 = \frac{\left(\sigma^2_{\ln(\hat{E}(\lambda_1))}+\sigma^2_{\ln(\hat{E}(\lambda_2))}\right)}{V^2}. \tag{4.27}$$

In general $\hat{E}(\lambda) > 10$ permitting substitution of Equation 4.11 to find the range estimate mean and variance in terms of system and mean parameters. The mean estimate of range is thus given by:

$$u_{\hat{d}} = \frac{\ln\left(\mu_{\hat{E}(\lambda_1)}\right) - \ln\left(\mu_{\hat{E}(\lambda_2)}\right) + \ln\left(\dfrac{I(\lambda_2)filter(\lambda_2)}{I(\lambda_1)filter(\lambda_1)} \cdot \dfrac{\rho(\lambda_2)}{\rho(\lambda_1)}\right)}{2\left(c(\lambda_2) - c(\lambda_1)\right)}$$

$$= \frac{\ln\left(\dfrac{\mu_{\hat{E}(\lambda_1)}}{\mu_{\hat{E}(\lambda_2)}} \cdot \dfrac{I(\lambda_2)filter(\lambda_2)}{I(\lambda_1)filter(\lambda_1)} \cdot \dfrac{\rho(\lambda_2)}{\rho(\lambda_1)}\right)}{2\left(c(\lambda_2) - c(\lambda_1)\right)} \tag{4.28}$$

which demonstrates that the intensity–range transformation is an unbiased estimator. Variance is given by:

$$\sigma_{\hat{d}}^2 = \frac{e^{-2\ln\left(\mu_{\hat{E}(\lambda_1)}\right)}\sigma^2_{\hat{E}(\lambda_1)} + e^{-2\ln\left(\mu_{\hat{E}(\lambda_2)}\right)}\sigma^2_{\hat{E}(\lambda_2)}}{4\left(c(\lambda_2) - c(\lambda_1)\right)^2} \tag{4.29}$$

This results will be tested in Section 5.2.2.

Since the intensity-range transformation is an unbiased estimator it is desirable to minimize variance which, as Equation 4.26 demonstrates is achieved by maximizing the measured intensities, and maximizing the difference between attenuation coefficients. These criteria are confirmed by a sensitivity analysis which follows shortly.

4.2 Estimation Sensitivity and Calibration Considerations

4.2.1 Reflection Coefficient Estimation

Although the technology developed in this thesis can be implemented in a package physically small enough to be carried underwater by a diver, its primary intended application is as a machine vision system for unmanned underwater vehicles (UUVs). As such, it will be one component in a suite of sensors and other data sources will be available to enhance operation. At a higher level of processing and perception, these data will likely be combined to yield the "optimal" description of the environment. Data fusion is a very active research area and it is hoped that future work will see inclusion of the developments presented herein into a high level, multi-sensor perception system.

At present, it is appropriate to consider how additional data can improve functionality of the intensity–range transformation. The spectral attenuation of the medium must be measured in situ [78] and is achieved through the calibration procedure defined in Section 3.1.2. The ability to measure the medium's optical properties is desirable within the vision system since it is very uncommon for a UUV to be equipped with suitable apparatus (such as a spectral transmissometer). Also inherent in calibration is inclusion of *system* parameters such as relative spectral intensity of the source and spectral response of lenses, filters, and CCD arrays. What may not be included in the calibration procedure and is the subject of this and the next section, is measurement or estimation of the relative reflection coefficients of a surface within the scene.

For many scenes, such as images of non-fouling surfaces on underwater docking cages, pipelines, drilling platforms, and other manmade structures, the reflection coefficient may well be known *a priori* and scene reconstruction proceeds with direct application of the intensity–range transformation. Exploitation of prior knowledge is

common in underwater vision systems [67]. There are also natural structures and surfaces for which relative reflection coefficients can be assumed. An example of interest in this category are icebergs[1] as discussed in Chapter 1. Other structures that are expected to be regularly inspected or navigated around such as subsea pipelines, can be fitted with optically well defined "tags" which function as visual beacons or reference points for 3D modeling by the vision system. Numerous algorithms have been developed for three dimensional modelling of surfaces from such data points and although analysis is beyond the scope of this dissertation, it can be stated that these techniques are particularly effective when, as in this case, there are a limited number of surface shapes to fit to the data. There are numerous useful applications for the intensity-range transformation where the relative reflectance of surface(s) of interest will be known; however, broader application of the results from this thesis requires strategies to extract or measure the relative spectral reflection coefficients of unknown surfaces. This can be achieved by combining the image data with data from "standard" UUV instruments.

With no information about the reflectance of a surface, the most direct means to extract spectral reflection coefficient ratios is to avail of other UUV sensors to obtain one or more surface range measurements, for example by "pinging" the surface with an active sonar. Relatively narrow beam sonars are common on UUVs for collision avoidance and can provide the required datum. This is a standard procedure for range gating underwater imaging systems to minimize the back scatter in an image. A sonar is used to estimate the distance to a surface of interest from which the two-way travel time for light is computed. A strobe light is pulsed for illumination but the camera's electronic shutter is delayed until just before the light from the illuminated surface is received thereby minimizing the loss of contrast due to backscatter. If the intensity-range transformation

---

[1] No written reference could be found to support or refute this assumption however discussions with ice experts in Canada and the UK have confirmed that there is very little difference in the color of icebergs or sea ice within a region such as the North Atlantic or Antarctic.

is to be used in a "self-contained" system with no other sonar available, the camera can easily and inexpensively be equipped with single point ranging capability by, for example, adopting a household ultrasonic ranging device of the type often used now as a replacement for conventional measuring tapes.

Some UUV builders and operators have equipped their vehicles with stereo vision for range estimation. A technique requiring salient visual features that will generate a cross-correlation peak, or that can be identified and localized in each of the stereo images. Very often underwater images do not contain salient or contrasting features (hence an advantage of the technique developed in this thesis) so stereo vision systems used underwater have been equipped with laser pointers to produce a "feature" on the surface of interest [15, 68, 69, 103]. This provides a single range estimate. It is practical to program the processor for one or both cameras in the stereo to execute the intensity-range transformation and efficiently compute the entire shape of the surface.

Fixed position lasers are also used in single camera underwater imaging systems. For example, the Johnson-Sea-Link series of submersibles used by Harbor Branch Foundation employ the LASER AIMING SYSTEM illustrated in Figure 4.2 [104]. The system was developed to overcome the difficulty in properly focusing cameras underwater (due to lack of contrast and scattering) combined with a typically narrow depth of field. With the LASER AIMING SYSTEM, the camera is prefocused to the intersection of two laser beams and the operator maneuvers the vehicle until this intersection is at the surface of interest. The surface is then photographed. A variation on this system could be to use different colored lasers so the approximate distance to the surface could be computed from the spacing of the laser "dots" in the image. In an iterative process, this estimate could be further refined once the orientation of the surface had been computed by the intensity–range transformation.

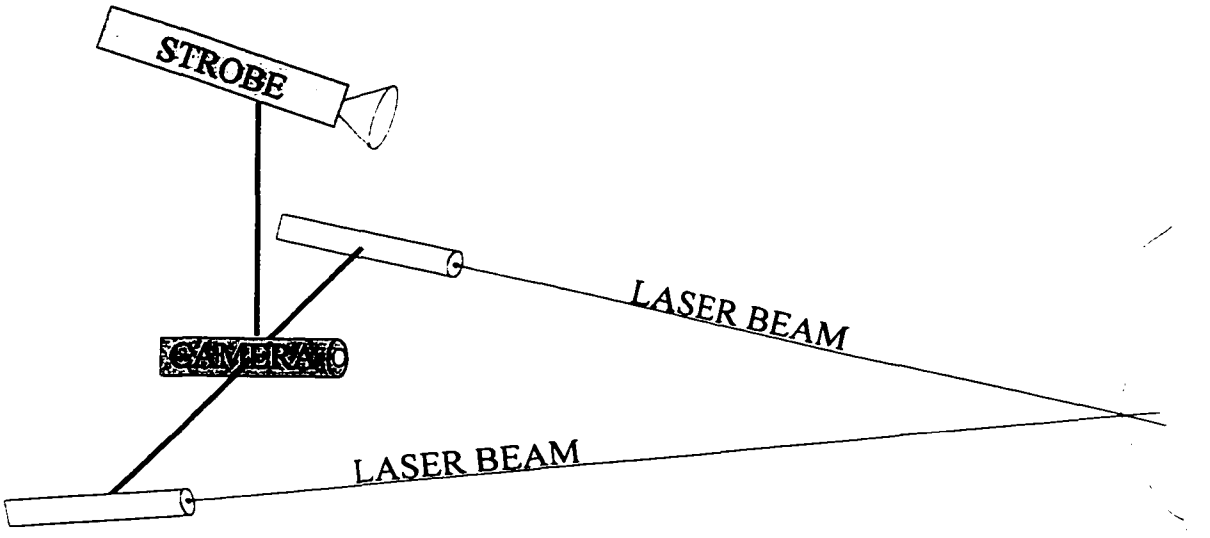

Figure 4.2: Laser Aiming System

It is also possible to employ the transformation in a "stand-alone" mode requiring no other sensors or projectors. With this capability, the transformation may be performed *in situ* or used to extract shape and range information after the fact from video tapes. If one considers a flat surface with constant reflectivity illuminated by a well defined light source, the magnitude of the illumination gradient across the surface varies inversely with the distance between the surface and the source. This was developed in a Ph.D. dissertation by Yu [70] and subsequent work by Yu, et. al. [71 - 74, 105] (described in Section 1.2) to estimate orientation of planar surfaces from underwater images.

At present this approach is very restrictive in its application; the scene must be of a Lambertian plane, the light source must be a point source, the camera and illumination source are co-located, and scattering is assumed not to exist. Also, because the first and second derivatives of measured intensities over the scene is required, this approach is very susceptible to noise. However, it is the subject of ongoing development in at least

two universities by researchers who are working to extend it to second order surfaces and non-point light sources [77, 105, 106].

Whether the reference datum is acquired through acoustic or optical means, it can be used to extract the reflectivity characteristics of the surface. The spectral reflection coefficient ratio can be computed from a single range measurement by rewriting Equation 4.4 as:

$$\frac{\rho(\lambda_2)}{\rho(\lambda_1)} \equiv \Delta\hat{\rho}_{21} = \exp\left(2\hat{d}\left(c(\lambda_2) - c(\lambda_1)\right)\right)\frac{\hat{E}(\lambda_1)}{\hat{E}(\lambda_2)} \cdot \frac{I(\lambda_2)filter(\lambda_2)}{I(\lambda_1)filter(\lambda_1)}, \qquad (4.30)$$

where $\hat{d}$ is the range estimate and the parameters in parenthesis on the rhs of Equation 4.30 are obtained from calibration. As discussed previously, if $\hat{d}$ is a Gaussian random variable, $\Delta\hat{\rho}_{21}$ will be an unbiased estimate with a variance of:

$$\sigma^2_{\Delta\hat{\rho}_{21}} = \exp\left(4\sigma^2_{\hat{d}}\left(c(\lambda_2) - c(\lambda_1)\right)^2\right)\left(\frac{2\hat{E}(\lambda_1)}{\hat{E}(\lambda_2)} \cdot \frac{I(\lambda_2)filter(\lambda_2)}{I(\lambda_1)filter(\lambda_1)}\right)^2. \qquad (4.31)$$

The sensitivity of subsequent range estimates with the intensity–range transformation to errors in $\Delta\hat{\rho}_{21}$ is explored in the next section.

As mentioned in this Section and previously in Chapter 1, fusion of information is a rapidly evolving technology and there are several robust algorithms available for its implementation; for example see [107]. The remainder of this Chapter considers the sensitivity of the intensity–range transformation to errors in estimates of reflection coefficient ratios and attenuation coefficients.

4.2.2 Sensitivity to Reflection Coefficient Estimation

Although several ways exist to recover surface reflection coefficient information, they are all subject to measurement error. The sensitivity of range calculations to these errors is examined through the partial derivative of the range estimate with respect to the reflection coefficient ratio. First, to provide more succinct writing of equations let

$$\frac{\rho(\lambda_2)}{\rho(\lambda_1)} = \rho_{21} \tag{4.32}$$

$$\frac{E(\lambda_1)}{E(\lambda_2)} = E_{12} \tag{4.33}$$

$$\frac{I(\lambda_2)filter(\lambda_2)}{I(\lambda_1)filter(\lambda_1)} = If_{21} \tag{4.34}$$

$$c(\lambda_2) - c(\lambda_1) = \Delta c_{21} \tag{4.35}$$

Substituting Equations 4.32 - 4.35 into Equation 4.4, the intensity–range transformation, and taking the partial derivative of $\hat{d}$ with respect to ρ_{21} yields

$$\frac{\partial \hat{d}}{\partial \hat{\rho}_{21}} = \frac{1}{2\Delta c_{21}} \cdot \frac{1}{\hat{\rho}21} \tag{4.36}$$

Equation 4.36 states that range estimation sensitivity to errors in the reflection coefficient ratio is a function of both attenuation coefficient difference and the reflection coefficient ratio. To understand more about the magnitude of the resultant error it is convenient to consider the range estimate error as a fraction of actual range. Solving the intensity–range transformation for Δc_{21} and substituting into Equation 4.36 yields:

$$\frac{\partial \hat{d}}{d} = \frac{1}{\ln(E_{12} If_{21} \rho 21)} \cdot \frac{\partial \hat{\rho}_{21}}{\hat{\rho}21} \tag{4.37}$$

which demonstrates that error in calculated range does not vary linearly with reflection coefficient error. Moreover, because of the monotonically increasing nature of the natural logarithm it is evident that range errors due to erroneous increases reflection coefficient ratio are smaller than those resulting from equivalent erroneous decreases in reflection coefficient ratio error. This is illustrated in Figure 4.3 using the system parameters from Section 3.2. The curve shows that, with the exception of gross errors (greater 90%), range estimation error is less than the error in reflection coefficient ratio. Equation 4.37 further indicates that errors will be minimized if the ratios in Equations 4.32 - 4.34 are maximized.

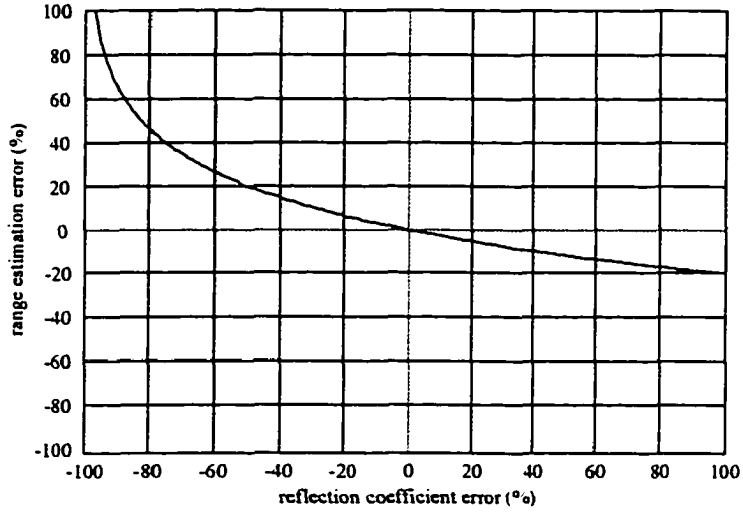

Figure 4.3: Range estimation error due to error in reflectance ratio

4.2.3 Sensitivity to Attenuation Coefficient Estimation

Equation 4.36 begs consideration of the sensitivity of range estimates to error in the calculation of attenuation coefficient difference. This is examined through the partial derivative of $\hat{d}$ with respect to $\Delta\hat{c}_{21}$ as given in Equation 4.38.

$$\frac{\partial \hat{d}}{\partial \Delta\hat{c}_{21}} = -\frac{\ln\left(E_{12} If_{21} \rho_{21}\right)}{2\left(\Delta\hat{c}_{21}\right)^2}. \tag{4.38}$$

Again writing in terms of fractional errors:

$$\frac{\partial \hat{d}}{d} = -\frac{\partial \Delta \hat{c}_{21}}{\Delta \hat{c}_{21}}. \tag{4.39}$$

In this case the magnitude of the fractional range estimation error equals the error in attenuation coefficient difference as illustrated in Figure 4.4. From Figures 4.3 and 4.4 it can be seen that, except for a gross error in calibration, the intensity/range transform is more sensitive to errors in attenuation difference than any other calibration parameter.

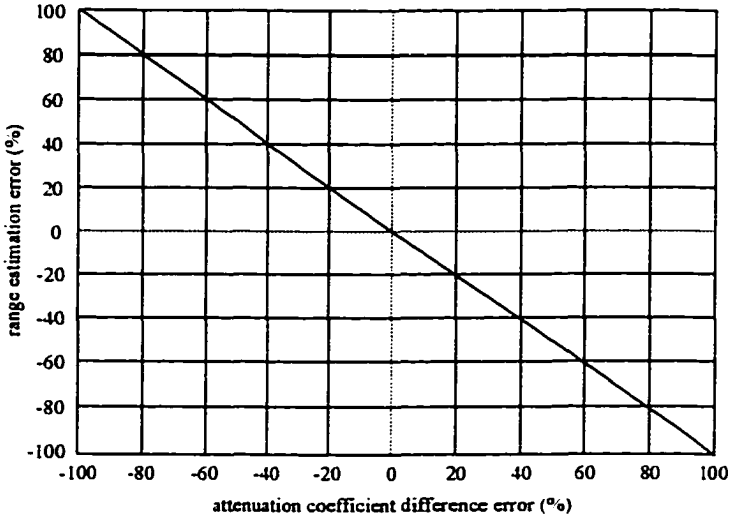

Figure 4.4: Range estimation error due to error in attenuation coefficient difference

The previous analysis confirms that for any given range, range estimation error is minimum when the fractional error in measured attenuation coefficient difference is minimum. Therefore, in the absence of other considerations, *maximum range estimation accuracy is achieved when using spectral bands whose attenuation coefficients are maximally unequal.* This is consistent with Eqn. 4.28 in which estimate variance is inversely proportional to the square of the difference in attenuation coefficients.

4.3 Multichannel Estimation

Thus far, consideration has been given to data from only two channels. Many of the CCD cameras presently available on both the industrial and consumer markets contain optics for diverting light received through the lens to three separate, filtered, CCD arrays - one each for the red, green, and blue channels required to fully represent the visible light spectrum. Such readily available optics, coupled with filters having 3 dB bandwidths of 10 - 15 nm [108], gives rise to the possibility of cameras that can receive light from up to 40 individual channels spanning the visual spectrum from 300 to 700 nm. Although that many optical channels may be somewhat unmanageable, one can envisage 5 or 10 separate spectral bands, or data channels. With 10 channels of data, the intensity – range transformation can yield up to 45 series' of range estimates.

4.3.1 Multichannel Advantages and Considerations

Combining series of estimates yields two conflicting criteria: analyses in Sections 4.1 and 4.2 reveal that for a given range estimate, it is advantageous to use data from channels with maximally unequal attenuation coefficients. For example, referring back to Figure 2.1 for pure seawater, one could combine data from channels centred on 450 nm where c(450) = 0.0190, and 700 nm where c(700) = 0.6507. However, Section 4.1 showed that estimate variance is directly proportional to signal variance. Other parameters being equal, the higher the attenuation coefficient, the lower the received irradiance and very likely, the lower the signal to noise ratio. Even for targets a few meters away the received signal can be significantly attenuated[2]. For example, light whose attenuation coefficient is 0.5 or greater decreases in intensity by more than 39% for each meter it propagates.

---

[2] The difference is more obvious when considering attenuation length. The attenuation length for c(450) = 0.0190 m^{-1} is 52.63 m, in contrast to 1.54 m for c(700) = 0.6507 m^{-1}.

Treating the range estimate extracted from two spectral channels as a random variable, and recalling Eqn. 4.29 (repeated below) for estimate variance, it is apparent that these requirements of minimum variance and maximum attenuation difference will manifest in the variance of the range estimate. If a series of estimates can be computed (i.e. if there is a stationary time series from each pixel in the camera) it is possible to improve subsequent estimates. This is illustrated in Chapter 5.

$$\sigma_{\hat{d}}^2 = \frac{e^{-2\ln\left(\mu_{\hat{E}(\lambda_1)}\right)}\sigma^2_{\hat{E}(\lambda_1)} + e^{-2\ln\left(\mu_{\hat{E}(\lambda_2)}\right)}\sigma^2_{\hat{E}(\lambda_2)}}{4\left(c(\lambda_2) - c(\lambda_1)\right)^2} \qquad \text{(4.29, repeated)}$$

One of the advantages of the system being developed in this dissertation is that it can estimate range from a single video data take (lasting only hundredths of a second). It can therefore be used in dynamic situations where the use of slower data acquisition methods may be impractical. In those cases alternate approaches are required for selecting spectral bands to use in the estimate. Again one can refer to the criteria of maximizing the difference in attenuation coefficients but minimizing signal variance. A caveat when maximizing attenuation coefficient difference is not to use data from channels where the signal is attenuated to a level below the noise floor of the camera. With only one observation, further processing to extract the signal from the noise is not an option.

A threshold for accepting spectral band data can be determined during the calibration procedure. Measuring the CCD output from pixels focused on a black "patch" on the calibration plate yields a threshold above which data can be used in range computations. This threshold represents the noise floor of the camera plus light backscattered from the medium between the camera and the plate. It is a reasonable lower bound for a threshold.

Figure 3.1 depicted the formation of underwater images as a combination of direct, forward scattered, and backscattered irradiance. It is still possible for a received signal containing an insignificant direct component to have a level above this threshold through the contribution of additional backscatter (received beyond the range of the calibration target). Backscattered irradiance decreases exponentially with range so its contribution to received signal level will "flatten out" beyond a few meters this is illustrated in Chapter 5). An upper bound on the threshold can thus be obtained from the irradiance backscattered from "open" water containing no obstacles other than the medium. Assuming no changes in the medium, any subsequent signals received above this threshold will contain information on the target surface of interest. This threshold was used in Section 3.3 when generating range maps of the pipe and ring.

4.3.2 Parameter Extraction Using the Kirlin Algorithm

By exploiting multispectral data a methodology devised by Kirlin [90] is adapted to extract various scene parameters. In general, it returns relative estimates for parameters from a medium's transfer function using sensitivity vectors. Applied to estimating geometric terms from the transfer function for water, the approach does not always provide a closed form solution but does have the advantage of including intensity measurements from an arbitrary number of spectral bands with minimal changes required to the coded algorithm, and provides information on parameters that cancel in the intensity–range transformation. The sensitivity vectors may also be used as objective functions to be minimized, thereby yielding absolute parameter estimates.

The transfer function of non-scattering water for the propagation of light has been developed in previous chapters as

$$T(\lambda_n, d, \gamma) = \frac{e^{-2c(\lambda_n)d}\,\rho(\lambda_n)\,filter(\lambda_n)\cos(\gamma)}{\pi m^2 d^2}. \tag{4.40}$$

For a given geometry, the irradiance at registered pixels in N spectral bands is given in matrix notation as:

$$\mathbf{E} = \mathbf{D_I T} \tag{4.41}$$

where

$$\mathbf{E} = \begin{bmatrix} E(\lambda_1) \\ E(\lambda_2) \\ \mathsf{M} \\ E(\lambda_N) \end{bmatrix}, \tag{4.42}$$

$$\mathbf{D_I} = \begin{bmatrix} I(\lambda_1) & 0 & \mathsf{L} & 0 \\ 0 & I(\lambda_2) & \mathsf{L} & 0 \\ \mathsf{M} & \mathsf{M} & \mathsf{O} & \mathsf{M} \\ 0 & 0 & \mathsf{L} & I(\lambda_N) \end{bmatrix}, \tag{4.43}$$

and

$$\mathbf{T} = \begin{bmatrix} \dfrac{e^{-2c(\lambda_1)d}\,\rho(\lambda_1)\,filter(\lambda_1)\cos(\gamma)}{\pi m^2 d^2} \\ \dfrac{e^{-2c(\lambda_2)d}\,\rho(\lambda_2)\,filter(\lambda_2)\cos(\gamma)}{\pi m^2 d^2} \\ \mathsf{M} \\ \dfrac{e^{-2c(\lambda_N)d}\,\rho(\lambda_N)\,filter(\lambda_N)\cos(\gamma)}{\pi m^2 d^2} \end{bmatrix}. \tag{4.44}$$

In this case, the desired geometric parameters are angle of incidence γ and range d. Expanding Eqn. 4.41 in a Taylor series about the nominal parameter values $\cos(\gamma_o)$ and d_o yields, for spectral band n:

$$\mathrm{E}(\lambda_n,\cos(\gamma),d)=\mathrm{E}_0(\cos(\gamma_o),d_o)+(\cos(\gamma)-\cos(\gamma_o))I_n\frac{\partial T_{no}}{\partial\cos(\gamma)}+(d-d_o)I_n\frac{\partial T_{no}}{\partial d}$$
$$+\frac{1}{2}\left((\cos(\gamma)-\cos(\gamma_o))^2 I_n\frac{\partial^2 T_{no}}{\partial\cos(\gamma)^2}+(d-d_o)^2 I_n\frac{\partial^2 T_{no}}{\partial d^2}\right)$$
$$+(\cos(\gamma)-\cos(\gamma_o))(d-d_o)I_n\frac{\partial^2 T_{no}}{\partial\cos(\gamma)\partial d}+\mathrm{L} \qquad (4.45)$$

where T_{n_o} is the transfer function with attenuation coefficient $c(\lambda_n)$, computed at $\cos(\gamma_o)$ and d_o. The difference between irradiance *measured* in all spectral bands, **E**, and irradiance *computed* for all spectral bands, $\mathbf{E_0}$ is found by rewriting Eqn. 4.41 as:

$$\mathbf{E}-\mathbf{E_0}=\delta_{\mathbf{E}}=\mathbf{D_I}\mathbf{D}_{coef}\left[\left.\frac{\partial \mathrm{T_{no}}}{\partial\alpha}\right|_{\alpha=\alpha_o}\right]\delta_\alpha, \qquad (4.46)$$

where: $\mathbf{D}_{coef}$ is a diagonal matrix for which element (i,i) is the coefficient associated with the i^{th} order derivative in the Taylor expansion, and

α is defined by Kirlin as a vector of unknown parameters and possibly their products. In this application

$$\alpha=\left[\cos(\gamma)\quad d\quad \cos(\gamma)^2\quad d\cos(\gamma)\quad d^2\right]^T, \qquad (4.47)$$

$$\text{hence}\quad\left[\left.\frac{\partial \mathrm{T_{no}}}{\partial\alpha}\right|_{\alpha=\alpha_o}\right]=\left[\frac{\partial \mathrm{T_{no}}}{\partial\cos(\gamma)}\quad\frac{\partial \mathrm{T_{no}}}{\partial d}\quad\frac{\partial^2 \mathrm{T_{no}}}{\partial\cos(\gamma)^2}\quad\frac{\partial^2 \mathrm{T_{no}}}{\partial\cos(\gamma)\partial d}\quad\frac{\partial^2 \mathrm{T_{no}}}{\partial d^2}\right]. \qquad (4.48)$$

δ_α is the deviation from nominal of the actual geometric parameters and is given by,

$$\delta_\alpha = \begin{bmatrix} \cos(\gamma) - \cos(\gamma_O) \\ d - d_o \\ \left(\cos(\gamma) - \cos(\gamma_O)\right)^2 \\ (d - d_o)\left(\cos(\gamma) - \cos(\gamma_O)\right) \\ (d - d_o)^2 \end{bmatrix}. \tag{4.49}$$

In the general development using complex Fourier transform data, Kirlin identifies a spectrally normalized matrix with columns that are sensitivity vectors relative to the parameters in α. For the application herein the data are real and measured in the frequency domain. The sensitivity matrix is given by:

$$\mathbf{G} = \mathbf{D}_{coef}\left[\left.\frac{\partial \mathrm{T_{no}}}{\partial \alpha}\right|_{\alpha=\alpha_o}\right] \tag{4.50}$$

which need not be square. Substituting Equation 4.50 into Equation 4.46, the difference between measured and computed irradiance is:

$$\mathbf{E} - \mathbf{E_o} = \delta_{\mathbf{E}} = \mathbf{D_I G}\,\delta_\alpha, \tag{4.51}$$

Applying the algorithm to estimating the geometric parameters in the transfer function of Eqn. 4.40, the derivatives for the sensitivity matrix are:

$$\frac{\partial \mathrm{T_{no}}}{\partial \cos(\gamma)} = \frac{e^{-2c(\lambda_n)d}\, filter(\lambda_n)\rho(\lambda_n)}{\pi m^2 d^2}; \tag{4.52}$$

$$\frac{\partial \mathrm{T_{no}}}{\partial d} = \frac{-2e^{-2c(\lambda_n)d}\cos(\gamma) filter(\lambda_n)\rho(\lambda_n)}{\pi m^2}\left(\frac{1}{d^3} + \frac{c(\lambda_n)}{d^2}\right); \tag{4.53}$$

$$\frac{\partial^2 T_{no}}{\partial \cos(\gamma)^2} = 0; \tag{4.54}$$

$$\frac{\partial^2 T_{no}}{\partial \cos(\gamma)\partial d} = \frac{-2e^{-2c(\lambda_n)d}\, filter(\lambda_n)\rho(\lambda_n)}{\pi m^2}\left(\frac{1}{d^3} + \frac{c(\lambda_n)}{d^2}\right); \tag{4.55}$$

$$\frac{\partial^2 T_{no}}{\partial d^2} = \frac{e^{-2c(\lambda_n)d}\cos(\gamma)\, filter(\lambda_n)\rho(\lambda_n)}{\pi m^2}\left(\frac{6}{d^4} + \frac{8c(\lambda_n)}{d^3} + \frac{4c(\lambda_n)^2}{d^2}\right). \tag{4.56}$$

The general algorithm derived by Kirlin generates a covariance matrix which is amenable to high resolution eigenanalysis to separate the signal and noise subspaces, ultimately leading to an estimate of the deviation-from-nominal-vector $\hat{\delta}_\alpha$. Estimates of the actual parameters are then given by:

$$\hat{\alpha} = \alpha_o + \hat{\delta}_\alpha \tag{4.57}$$

In the application considered here $\hat{\delta}_\alpha$ is found by solving Equation 4.51 to generate the estimates:

$$\hat{\delta}_\alpha = \left(\mathbf{G}^T\mathbf{G}\right)^{-1}\mathbf{G}^T\mathbf{D}_I^{-1}\delta_E \tag{4.58}$$

which is zero when the nominal value of the parameters in α equal the actual geometric values. Equation 4.58 therefore, can be considered an objective function in an optimization problem. In this reduced form, the algorithm is similar to the Gauss-Newton optimization technique with the sensitivity matrix **G** analogous to the Jacobian. The objective now is to find nominal values for the geometric parameters which make Equation 4.58 converge to zero.

In practice, if the initial values of the nominal parameters are not close to actual, the deviation estimate has substantial error ("close" and "substantial" are elucidated in

Section 5.2.4). Each estimate is however, the gradient or Hessian at a nominal point in Euclidean space spanned by α and as such, supports an iterative process which should converge to the correct solution. In alternative usage, for most surfaces a single computation is sufficient to estimate the difference in known distance from the camera to one pixel, and the unknown distance from the camera to an adjacent pixel. Following this procedure generates an estimate of surface shape.

Prior to solving Equation 4.58 it is apparent from Equation 4.54 that **G**, as defined in Equation 4.50 is singular and therefore cannot be inverted. Even with the singularity removed, Equations 4.53 and 4.55 generate columns that are scalar multiples ($\cos(\gamma)$ is constant across the spectrum) hence **G** still has reduced rank and is therefore ill conditioned for pseudo-inverting. To mitigate this problem Columns 3 and 4 (Eqns. 4.54 and 4.55) are omitted from **G**. No information is lost by their removal and the resulting number of computations is reduced. The implementation and performance of this algorithm in noise is presented in Section 5.2.4.

Chapter 5

Recovering Range from Images: Results and Analysis

5.0 Introduction

The technology being advanced here is a novel approach to one aspect of underwater imaging that provides previously unavailable capabilities within an envelope of operating conditions. It is the purpose of this research to begin development of that technology and examine that envelope. To this end, the machine vision "system" is viewed as comprising three subsystems: the light source and camera; the medium; and the target. In practice we have little control over the medium or target so the only recourse is to develop a camera and light system that functions over the widest range, or most probable operating conditions. Hopefully both. The centre of the envelope is described by the ideal case of no noise, a non-scattering well defined medium, and a target of known reflectance. Analysis of system response to deviations from this centre will be helpful for further development of the technology .

This Chapter implements and tests in a variety of conditions, the intensity–range transformation developed and presented in Chapters 3 and 4. Investigating the performance of this underwater machine vision technique requires that its response to

variations of several parameters be quantified. These are divided into three categories as follows:

sensor parameters:	sensor/system noise
	spectral bands available
medium parameters:	attenuation coefficients
	point spread function
	backscattering coefficient
scene parameters:	reflection coefficients

The introduction of scattering in this Chapter gives rise to several new considerations in implementation of the intensity-range algorithm.

There are so many environment and system parameters affecting the accuracy of the intensity-range transformation that one is challenged to present results that are meaningful, clear, and concise while also giving the true and complete picture of algorithm performance and limitations. In this same vein, it is prudent to display "raw" results from the intensity-range transformation so that the actual algorithm performance without enhancement by filtering or surface fitting can be assessed. Notwithstanding this need for reporting accuracy, in practice the transformation will in all likelihood be followed (or preceded) by some form of filtering; therefore, results with median filtering and smoothing will also be provided with the unenhanced results.

Section 5.1 introduces the simulator used in this Chapter. Section 5.2 builds on the work in Chapter 4 and looks at estimation accuracy as a function of noise using 2 or more optical channels. This results are compared with the performance predicted in Chapter 4. The final section includes all medium and system perturbations and uncertainties to assess performance of the vision system.

5.1 Simulator Output

Considerable time and care was invested in identifying the computer simulation model must appropriate for use in this dissertation. The selected model is based on a formulation by McGlamery and a team at the Scripps Institute of Visibility Laboratory [37, 38]. In addition to being a powerful research tool it is also used in a commercially available simulation package to test the effects of varying the configuration of underwater lighting/imaging systems [39, 40, 41]. Originally written for monochromatic light, it was extended to color images and further validated [44]. Thus far in this dissertation, all computer modelling and analysis, and processing of actual images have been executed in the Matlab® environment. McGlamery's computer model was also rewritten in Matlab® executable code for this dissertation. This Section provides a basic discription of the simulator and illustrates a typical set of simulator output images. Details of the model are found in the above cited references, particularly [37].

The images that follow are 64 × 64 pixels. Figure 5.1 is a plot of the scene to be imaged. It is a brick partially buried in a flat seafloor. It protrudes 10 cm above the background and is 5.9m from the camera at the closest point. Using the source intesity distribution function, the reflectance of the surface being imaged, and the IOPs of water, the simulator generates the following image plane irradiance components:

1. $E_P(x_s,y_s, z_s)$: irradiance at the surface being imaged. The subscript P denote general space coordinates;
2. $E_d(x,y)$: image plane irradiance due to direct, or non-scattered light reflected from the surface. In this case x and y are image plane coordinates with $z = fl$ implied;
3. $E_f(x,y)$: image plane irradiance due to scattered light reflected from the surface (often called the *glow field*);
4. $E_b(x,y)$: image plane irradiance due to light backscattered from the medium.

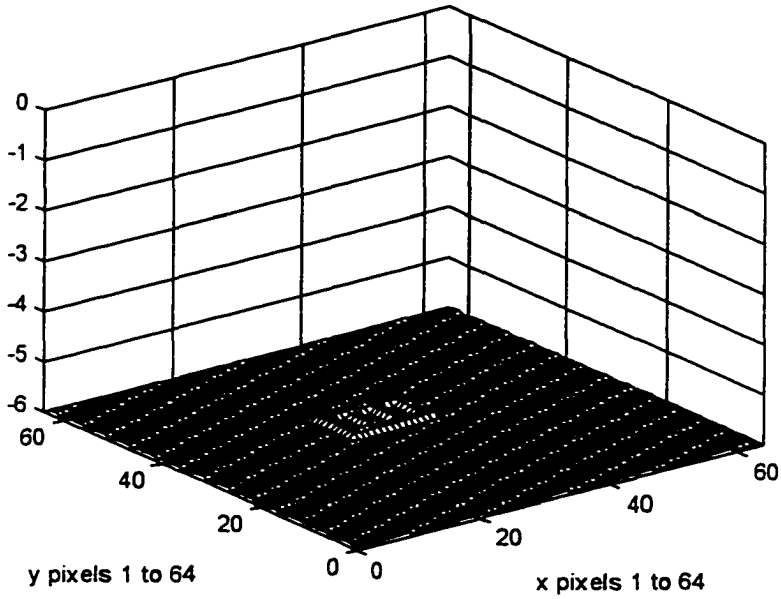

Figure 5.1: Plot of surface by imaged

The irradiance at the surface is given by

$$E_P(\lambda, x_P, y_P, z_P) = \frac{I(\lambda) BP(x_P, y_P, z_P)}{\pi d_s^2} e^{-c(\lambda) d_s} \rho(\lambda) \cos(\gamma) \quad \text{W/m}^2 \tag{5.1}$$

where BP is the beam pattern of the source and includes spreading loss and scattering by water. The effects of water on irradiance reflected from the surface to the image can be incorporated through the convolution integral

$$\iint E_P(\lambda, x_P, y_P, z_P) S(\lambda, x, y, x_P, y_P, z_P), \tag{5.2}$$

where S is the point spread function of water in the image plane for a surface point at (x_P, y_P, z_P). Multiplying the Fourier Transforms of E_P and S would require that S be shift invariant across the surface which is not the case. However, researchers at the Scripps Institute of Oceanography have from emperical data derived the following form of the Fourier Transform of S:

$$S(f,\lambda) = \left(e^{-G(\lambda)d_c} - e^{-c(\lambda)d_c}\right)e^{-Bd_c f} + e^{-c(\lambda)d_c}, \tag{5.3}$$

which is the optical transfer function. In Eqn 5.3

G is an emperical attenuation coefficient;

B is an emperical coefficient related to the scattering coefficients;

f is angular spatial frequency, cycles/radian; $f = \sqrt{f_x^2 + f_y^2}$.

The effects of G and B on image formation is examined in Section 5.3.1.

The final term in Equation 5.3 generates the direct component of the final image. The inverse Fourier Transform is

$$\mathcal{F}^{-1}\{S(f,\lambda)\} = \mathcal{F}^{-1}\left\{e^{-c(\lambda)d_c}\right\} = e^{-c(\lambda)d_c}\delta(0,0); \tag{5.4}$$

hence,

$$E_d(x,y) = E_P(x_P, y_P, z_P)e^{-c(\lambda)d_c} \tag{5.5}$$

which is consistent with the equations in Chapter 3. Figure 5.2a is the direct irradiance component of the final image. Figure 5.2b is similar but with the data scaled to enhance contrast. The concentric "rings" in the enhance image is due to both beam pattern and increased attenuation (because range increases with distance from the centre of the image).

Now the effects of the water are introduced to the light reflected from the surface by effectively convolving the remaining components of S in Eqn. 5.3 with E_P.as described by Eqn. 5.6.

$$E_f(x,y,\lambda) = F^{-1}\left\{F\left\{\left(e^{-G(\lambda)d_c} - e^{-c(\lambda)d_c}\right)E_P(x,y,\lambda)\right\}e^{-Bd_c f}\right\} \tag{5.6}$$

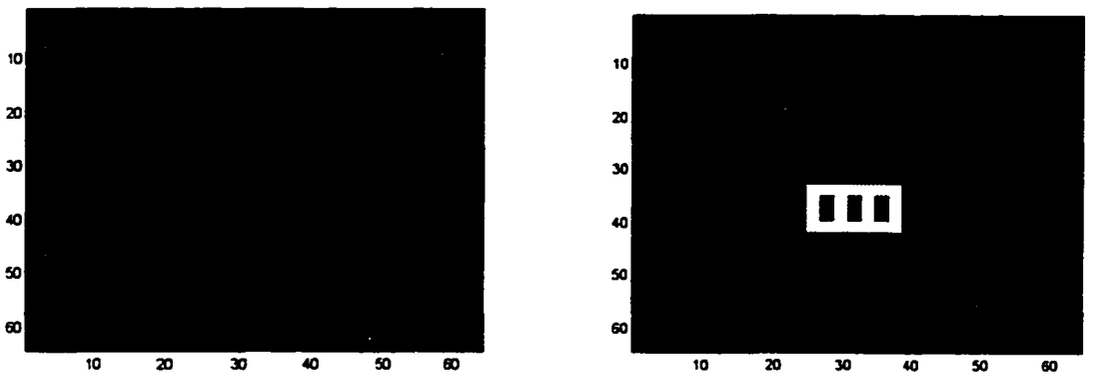

(a) (b)

Figure 5.2: Direct radiance

In practice the E_P irradiance array is first weighted by $e^{-G(\lambda)d_c} - e^{-c(\lambda)d_c}$. The result is Fourier Transformed, multiplied by $e^{-Bd_c f}$, and that product is inverse transformed to yield the forward scattered component of the image. Figure 5.3 is the point spread function used in this example. It is sharply forward peaked so, in terms of forward scatter, small angle scattering is dominant. Figure 5.4a is the image component resulting from light forward scattered from the surface to the camera. Figure 5.4b is the same image with the data scaled and clearly illustrates the blurring effect of forward scatter.

Backscatter image generation is the most computationally intensive portion of the simulation. For this calculation the medium is "cut" into a series of "slabs" parallel to the image plane. In the case of no other scattering or attenuation, the irradiance in the image plane from light scattered back from an elemental slab volume centred at (x_P, y_P, z_P) is

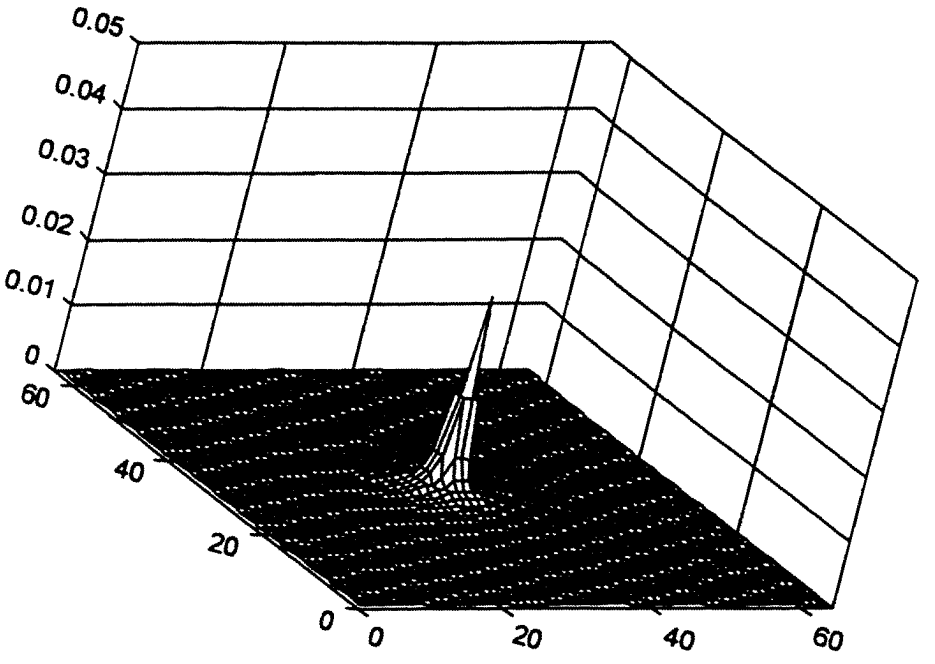

Figure 5.3: Point Spread Function

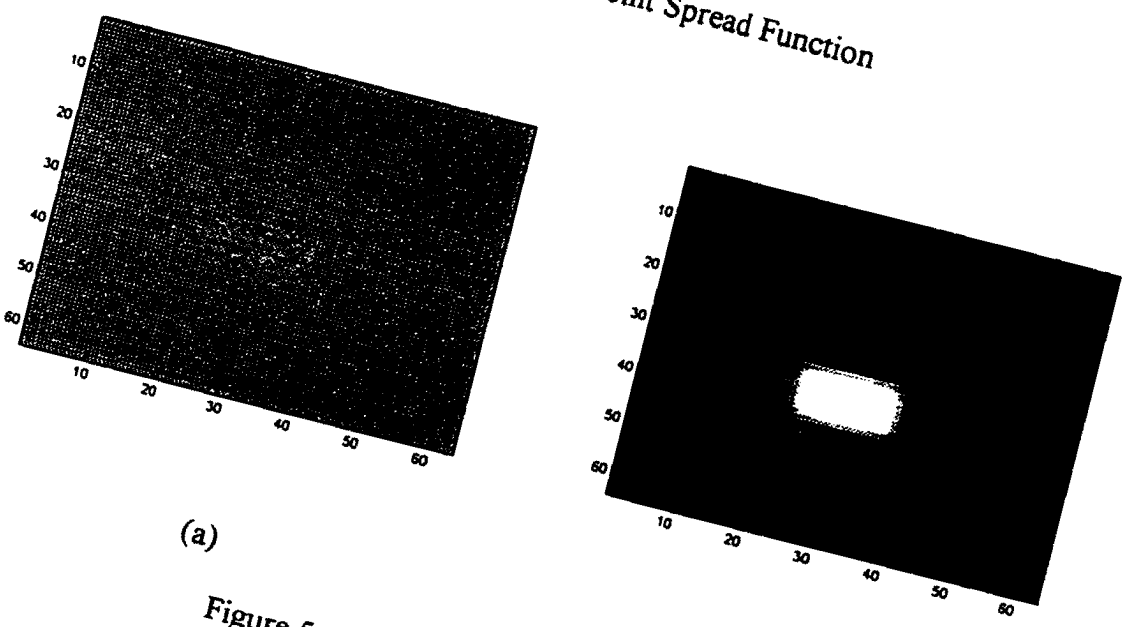

Figure 5.4: Forward scattered component

$$E'_P(x,y) = \beta(\alpha)E_P(x_p, y_p, z_p)\Delta z \ , \tag{5.7}$$

where $\beta(\alpha)$ is the volume scattering function described in Chapter 2;

Δz is slab thickness.

The attenuation and scattering effects of the medium on light reflected back from the slab is found by convolving Eqn. 5.7 with the PSF. As with the actual surfaced being imaged, this is done by breaking the PSF into a direct and a forward scattered component. The backscattered component of the image from one slab of light is therefore given by

$$\begin{aligned} E_{b_1}(x,y,\lambda) = F^{-1}\left\{ F\left\{\left(e^{-G(\lambda)d_c} - e^{-c(\lambda)d_c}\right)E'_{P_1}(x_P, y_P, z_P, \lambda)\right\}e^{-Bd_c f}\right\} \\ + E'_{P_1}(x_P, y_P, z_P, \lambda)e^{-c(\lambda)d_c} \end{aligned} \tag{5.8}$$

The total back scatter irradiance due to the entire volume of water between the surface being imaged and the camera is found by adding the back scatter from each slab as in Eqn. 5.9 where N is the total number of slabs.

$$E_b = \sum_{n=1}^{N} E_{b_i} \tag{5.9}$$

Figure 5.5a illustrates the backscattered component of the image. Figure 5.5b is the enhance view.

Figure 5.6 is the final image including the contributions of direct, forward scattered, and backscattered irradiance. A 3d plot of the total irradiance is given in Figure 5.7.

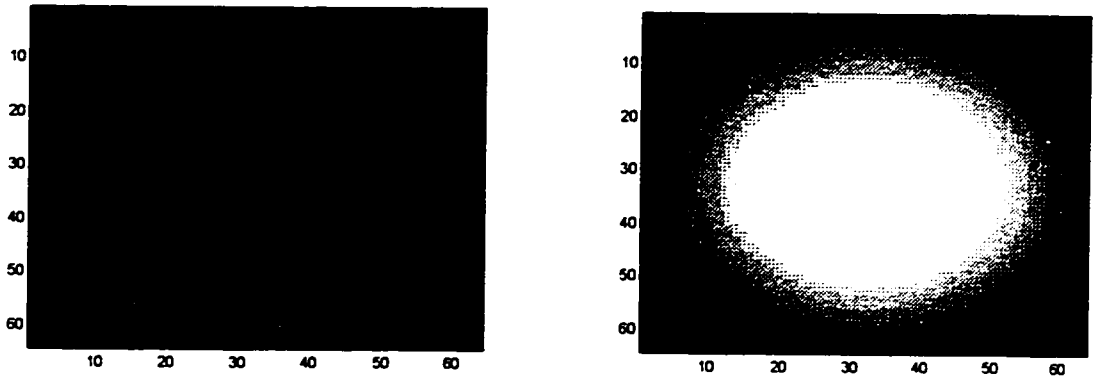

(a) (b)

Figure 5.5: Backscattered light

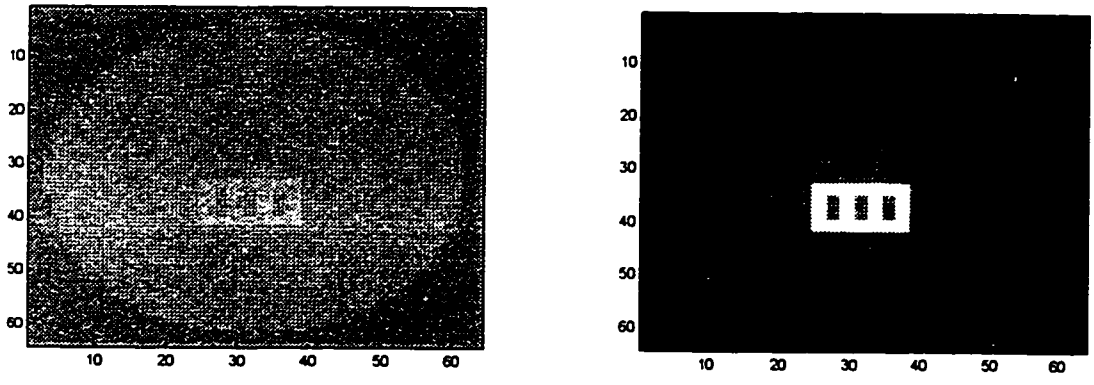

(a) (b)

Figure 5.6: Actual image

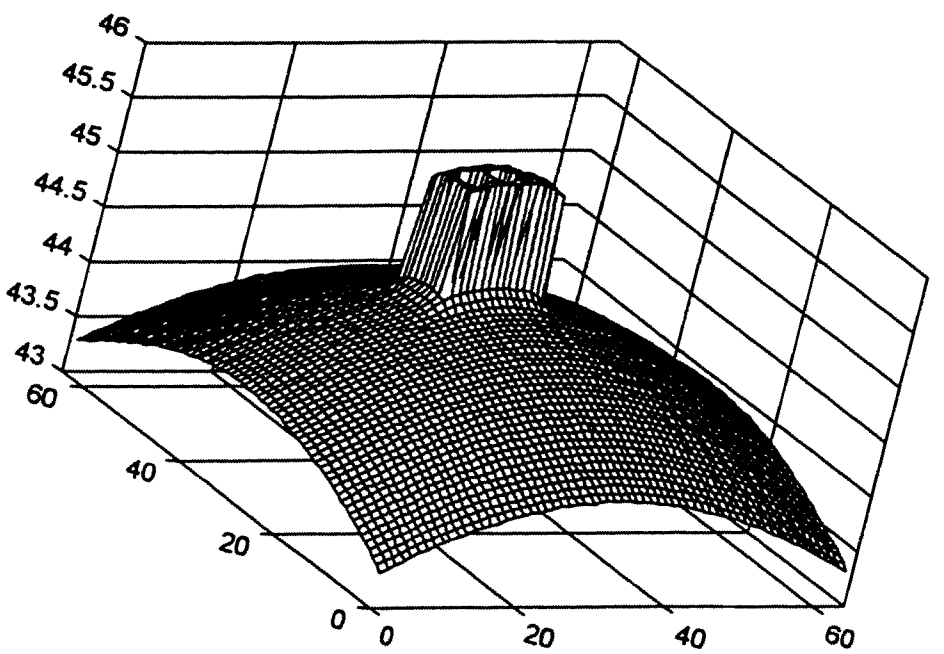

Figure 5.7: Irradiance plot

5.2 Accuracy versus Noise with No Scattering

5.2.1 Two Channel Estimation

In the absence of scattering (which is considered in the next section), actual range to the scene is not the most significant parameter since the maximum range at which the surface is visible can be increased, almost without bound, by increasing intensity of the source illumination. Therefore, results in this section are presented in terms of rms error as a function of SNR. RMS error is calculated over the entire scene as:

$$\text{rms error in } \hat{d} = \sqrt{\frac{\sum_{y=1}^{Y}\sum_{x=1}^{X}\left(\hat{d}_{xy} - d_{xy}\right)^2}{X \cdot Y}} \quad m. \tag{5.1}$$

where d_{xy} and $\hat{d}_{xy}$ are the actual and recovered ranges respectively for pixel xy, X is the total number of rows, and Y is the total number of columns.

Several approaches to computing image SNR are present in the literature. The formulation used here is:

$$SNR = 10\log\left(\frac{\sum_{y=1}^{Y}\sum_{x=1}^{X}\left(image\_pixel_{xy}\right)^2}{\sum_{y=1}^{Y}\sum_{x=1}^{X}\left(noise\_pixel_{xy}\right)^2}\right) \quad dB \tag{5.2}$$

where: $image\_pixel_{xy}$ is the scene irradiance with no noise as measured by pixel xy in the image plane; and $noise\_pixel_{xy}$ is the magnitude of the noise component added to pixel xy.

Figure 5.8 illustrates the effects of zero mean Gaussian noise on images at various SNRs. In each image, shutter speed is set to yield a maximum intensity image without saturating pixels.

The intensity-range transformation was tested for SNRs ranging from 0 dB to 10 dB and error is calculated over the entire scene as in Eqn. 5.1. In these trials spectral bands from the red, green, and blue regions of the spectrum were used with wavelengths centered at 675 nm, 575 nm, and 475 nm respectively. For Jerlov Type II water, as discussed in Chapter 2, corresponding attenuation coefficients are $c_{675} = 0.46$, $c_{575} = 0.11$, $c_{475} = 0.06$.

The results plotted in Figure 5.9 illustrate that the intensity-range transformation is an effective subsea machine vision technique for extracting range data. With a SNR of 2 dB (which from Figure 5.8 is rather low) the intensity-range transform recovered range data with an rms error of less than 6 cm. At 4 dB, error dropped to less than 1 cm. The reconstructed three dimensional scene retrieved by the intensity-range transformation with image SNR of 4 dB is plotted in Figure 5.10a. The actual surface is juxtaposed in Figure 5.10b for comparison.

The results thus far support the intensity–range transformation as a new subsea machine vision tool for reconstructing three dimensional environments from multispectral images. At "reasonable" SNRs of 3 dB or greater, environments can be reconstructed to accuracies of a few (< 3) cm. With an SNR of 5 dB, accuracy is improved to better than 1 cm. Also evident in the results, is the advantage that can be gained by employing image enhancement techniques, particularly when the received images are noisy (SNR < 4 dB). Figure 5.9 plots the results when no filtering is used, when the intensity images are pre-processed by a 3×3 median filter, when the images are transformed directly and the result is processed by a 3×3 median filter, when they are pre-processed by a 3×3 neighborhood averaging filter, and when the result is post-processed by a 3×3 neighborhood averaging filter.

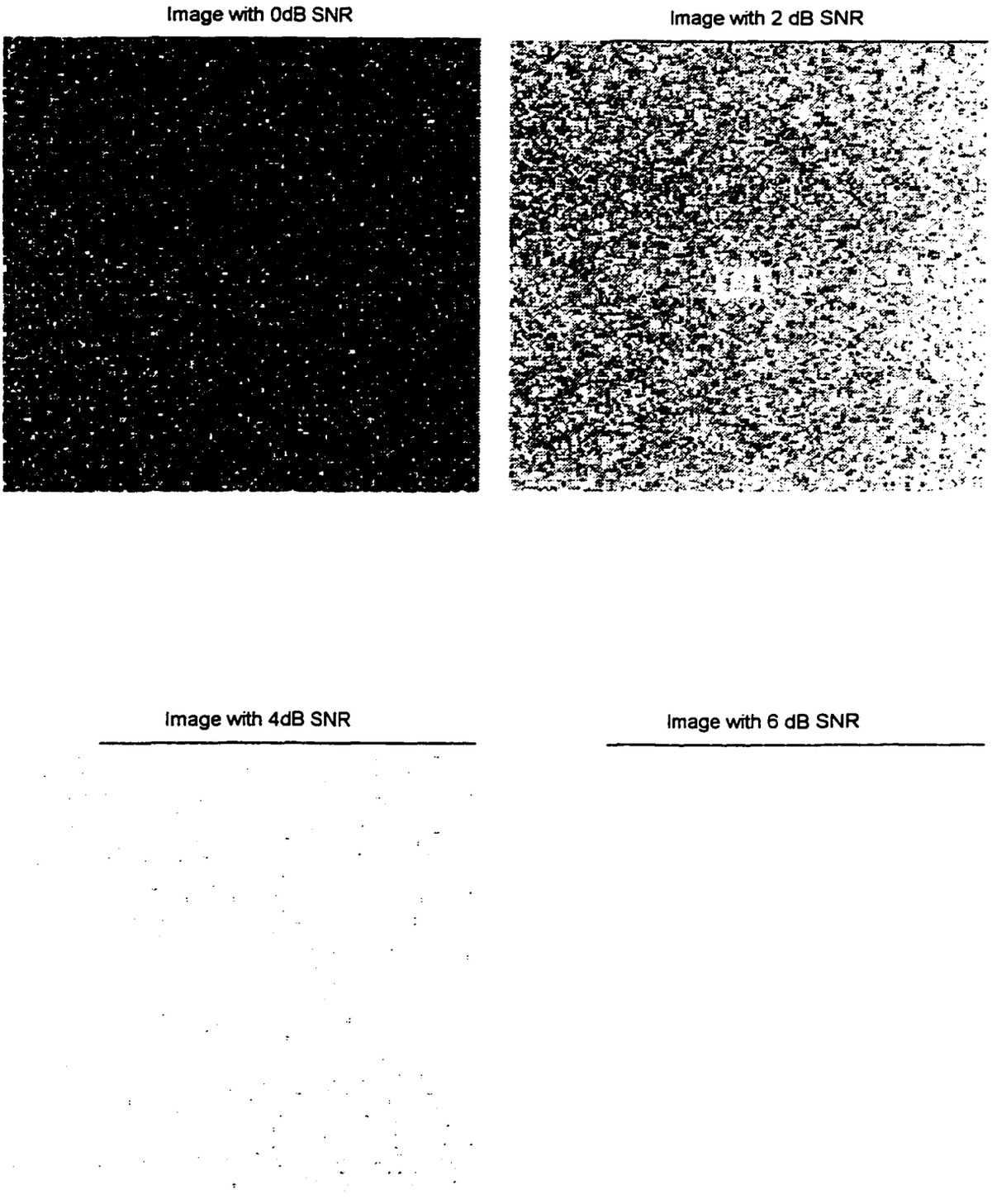

Figure 5.8: Examples of test images at 0.0, 2.0, 4.0 and 6.0 dB SNR

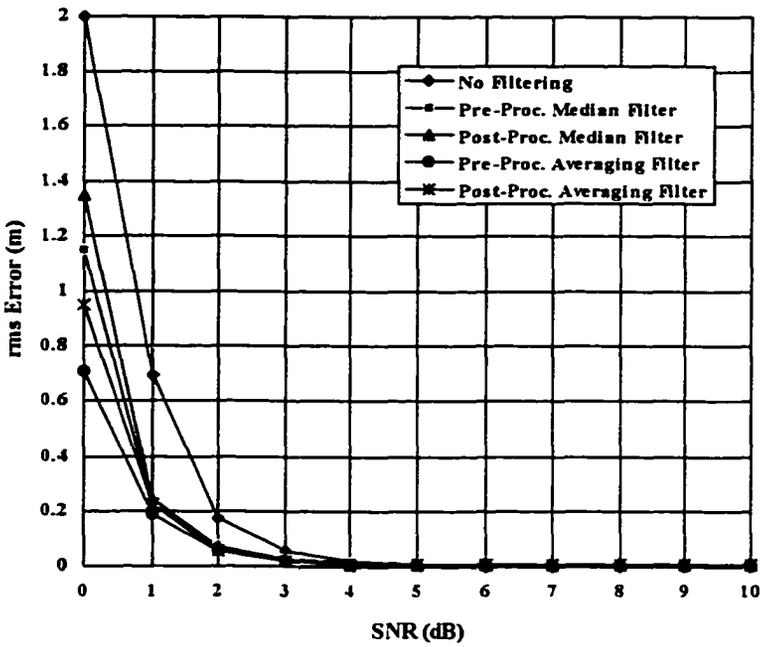

Fig. 5.9a: rms error for scene in Figure 5.8 with $\Delta c = 0.40$

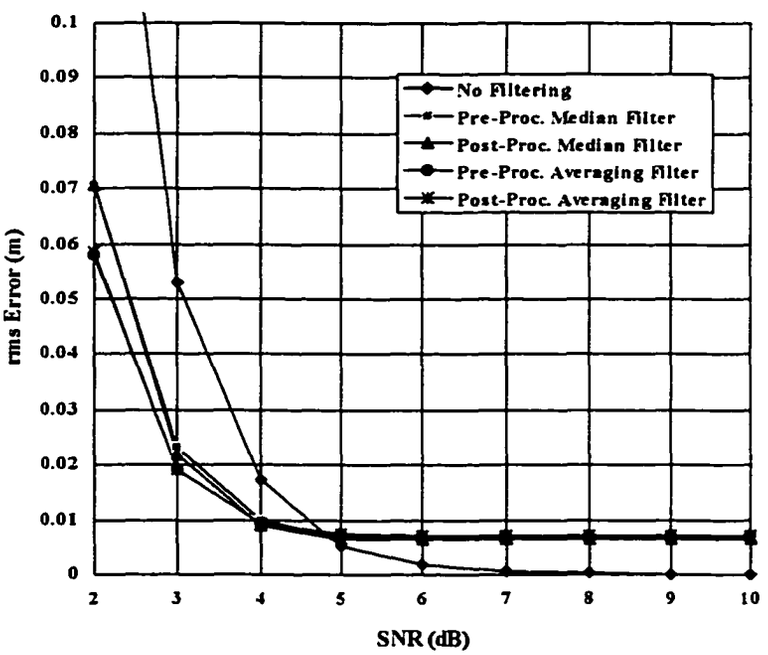

Fig. 5.9b: Expanded ordinate view of rms error for scene in Fig. 5.8 with $\Delta c = 0.40$

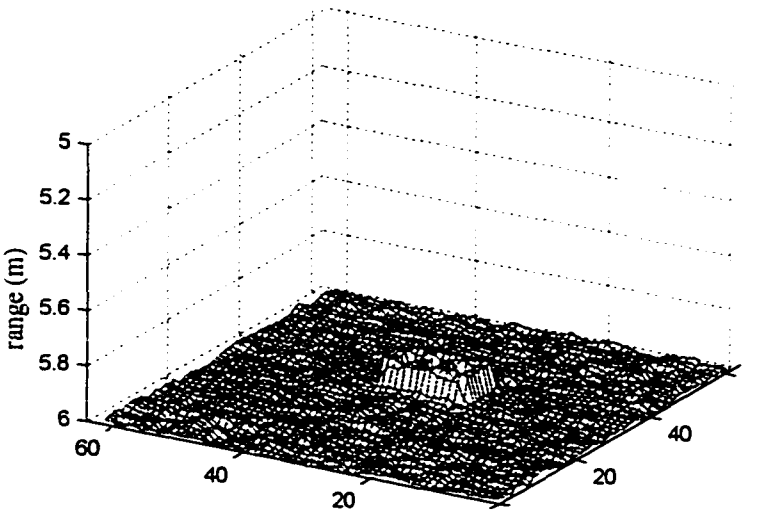

Fig. 5.10a: Recovered surface with 4 dB SNR

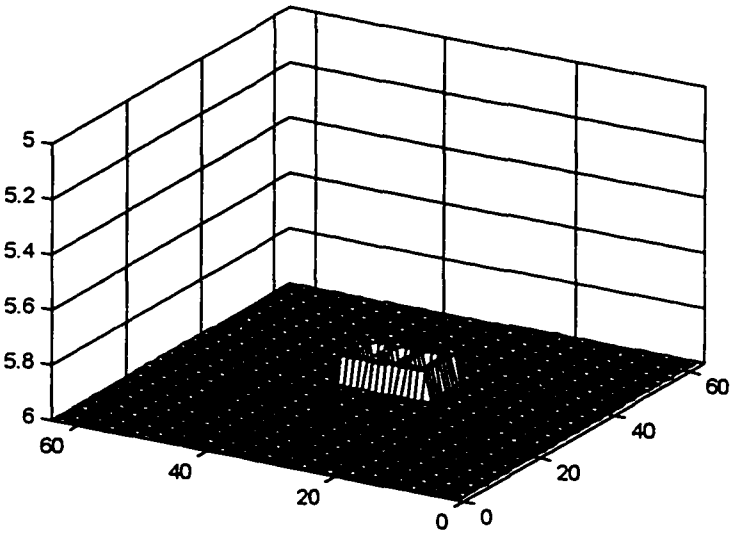

Fig. 5.10b: Actual surface as in Figure 5.1

For the surface under consideration, neighborhood averaging provides on the most accurate results at low SNRs. As SNR increases, the improvement from supplementary processing diminishes. As illustrated in Figure 5.9b, when SNR reaches 5 dB all results

are within 0.01 m and the most accurate results are achieved with no additional processing. The neighborhood averaging and median filters inherently cause distortions at discontinuities in images, and at the higher SNRs these distortions become significant. The test surface used here has 5 distinct surfaces with 0.010 m step changes between them. Erroneous artifacts from the filtering process at these discontinuities, or edges, places a lower bound on the transformation accuracy when these processes are employed. For this test surface that bound appears to be $6.4 \cdot 10^{-3}$ m for 3 × 3 median filtering and $7.1 \cdot 10^{-3}$ m for 3 × 3 neighborhood averaging.

5.2.2 Comparison with Probability Theory

Analysis in Chapter 4 showed that improved range results are achieved by maximizing the difference in attenuation coefficients for the spectral bands used in the intensity–range transformation. In the previous tests attenuation coefficients of 0.46, 0.11 and 0.06 m^{-1} were available. Figure 5.11 is a plot of the results obtained with the three possible combinations. These data, which demonstrate up to an 65% decrease in error (when SNR = 0 dB) for an increase in attenuation coefficient difference of 0.35 substantiates that conclusion. As SNR increases, estimation becomes more accurate and the improvement realized from increase attenuation coefficient difference becomes less salient. Nonetheless, even with a SNR of 10 dB the rms error for $\Delta c = 0.05$ is 1.5×10^{-4} m compared to almost an order of magnitude smaller error of 1.9×10^{-5} m when $\Delta c = 0.40$.

These results bode well for application of the intensity–range transformation since the attenuation coefficients chosen for these tests were not overly optimistic or exaggerated in their spectral variation. On the contrary, Smith and Baker [20] determined that for pure sea water, attenuation coefficients in similar spectral bands to those used here are: c_{690} =

0.500, c_{580} = 0.109, and c_{450} = 0.0168 yielding a maximum coefficient difference of c_{690} - c_{450} = 0.4832. Of course even greater differences are possible by extending into the infrared or ultraviolet spectrums, but there is a practical limit on the magnitude of the attenuation coefficient one wishes to exploit. Returning to the concept of attenuation length defined in Chapter 2, a $c(\lambda) = 0.500$ yields an attenuation length of

$$\pounds_c(\lambda) = 1/0.500 = 2 \text{ m},$$

thus light in a collimated beam is reduced by approximately 36.8 % every 2m.

Chapter 4 (Section 4.1) contained probability analysis of the intensity–range transformation when the intensity measurements are corrupted by zero mean Gaussian noise. The result was that the transformation provides an unbiased estimated with a mean of:

$$\mu_{\hat{d}} = \frac{\ln\left(\frac{\mu_{\hat{E}(\lambda_1)}}{\mu_{\hat{E}(\lambda_2)}} \cdot \frac{I(\lambda_2)\,filter(\lambda_2)}{I(\lambda_1)\,filter(\lambda_1)} \cdot \frac{\rho(\lambda_2)}{\rho(\lambda_1)}\right)}{2\left(c(\lambda_2) - c(\lambda_1)\right)} \tag{5.3}$$

and a variance of:

$$\sigma^2_{\hat{d}} = \frac{e^{-2\ln\left(\mu_{\hat{E}(\lambda_1)}\right)}\sigma^2_{\hat{E}(\lambda_1)} + e^{-2\ln\left(\mu_{\hat{E}(\lambda_2)}\right)}\sigma^2_{\hat{E}(\lambda_2)}}{4\left(c(\lambda_2) - c(\lambda_1)\right)^2}. \tag{5.4}$$

Considering the case where SNR = 4 dB, statistics for intensities measured by the red (λ = 675 nm), green (λ = 575 nm), and blue (λ = 475 nm) channels are substituted into Eqns. 5.3 and 5.4 to compute an expected estimate mean and variance. These statisitcs are as follows:

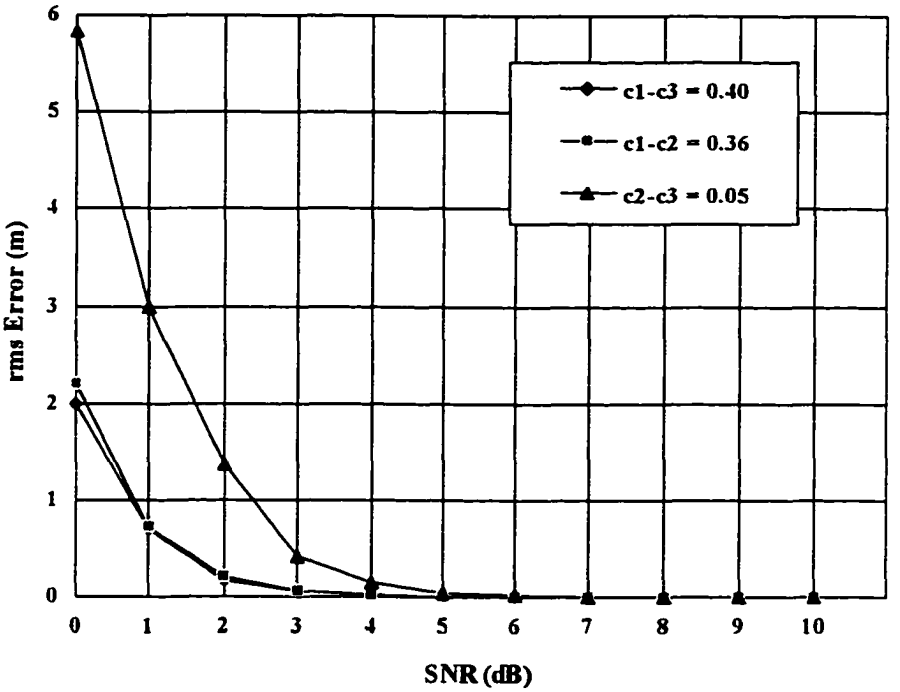

Fig. 5.11a: Estimate error for Δc = 0.40, 0.36 and 0.05

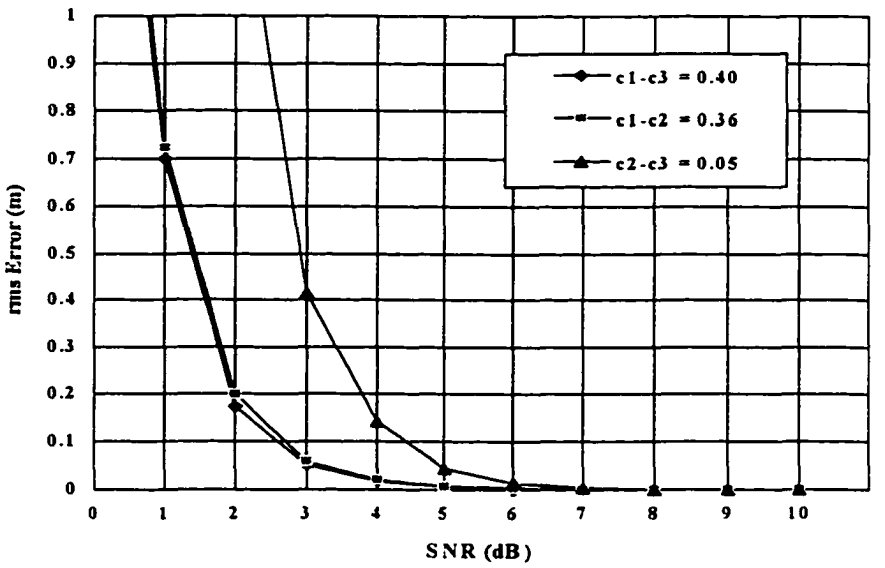

Fig. 5.11b: Figure 5.11a with expanded ordinate

$$\mu_{\hat{E}(\lambda=475)} = 40.624 \qquad \sigma^2_{\hat{E}(\lambda=475)} = 0.179$$
$$\mu_{\hat{E}(\lambda=575)} = 35.496 \qquad \sigma^2_{\hat{E}(\lambda=575)} = 0.136$$
$$\mu_{\hat{E}(\lambda=675)} = 9.295 \qquad \sigma^2_{\hat{E}(\lambda=675)} = 0.007$$

Density functions for the measured irradiance from three channel are plotted in Figures 5.12 to 5.14.

Using, for example the blue and green channel statistics to compute the expected mean and variance of the range estimate yields:

$$\mu_{\hat{d}_{bg}} = \frac{\ln\left(\frac{40.624}{35.496}\cdot\frac{0.800}{0.750}\right)}{2(0.050)} = \frac{\ln(1.221)}{0.100} = 1.997 \text{ m};$$

$$\sigma^2_{\hat{d}_{bg}} = \frac{e^{-2\ln(40.624)}0.179 + e^{-2\ln(35.496)}0.136}{4(0.050)^2} = 0.022.$$

where the 0.800/0.750 term is a calibration constant. The actual statistics for the 4096 estimates from a 64×64 pixel image are

$$\mu_{\hat{d}}\,(\text{actual}) = 1.998 \text{ m},$$

$$\sigma^2_{\hat{d}}\,(\text{actual}) = 0.022,$$

which is consistent with the theoretical results. The standard deviation of estimate error is 0.148 which is consistent with the results plotted in Figure 5.11. The distributions of all three series of range estimates are plotted in Figures 5.15 to 5.17 and approximate Gaussian distributions as predicted by the analysis in Chapter 4..

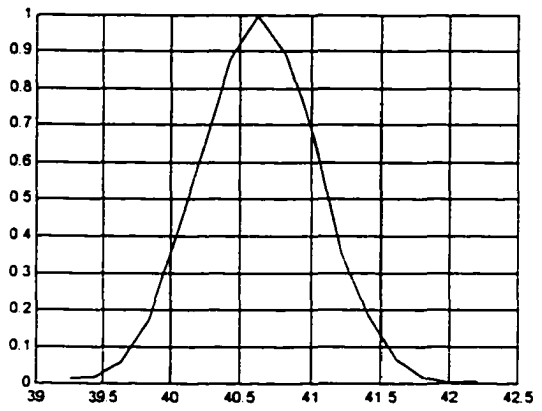

Figure 5.12: Irradiance distribution for λ = 475 nm (blue) channel

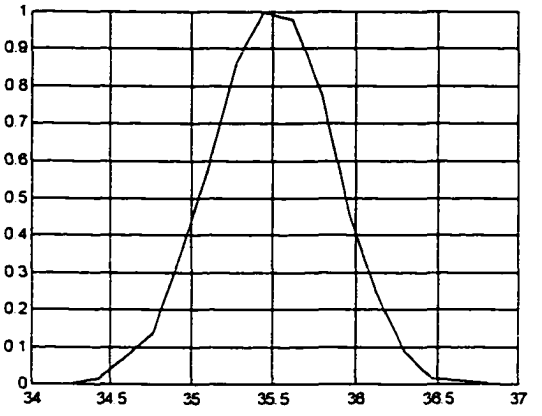

Figure 5.13: Irradiance distribution for λ = 575 nm (green) channel

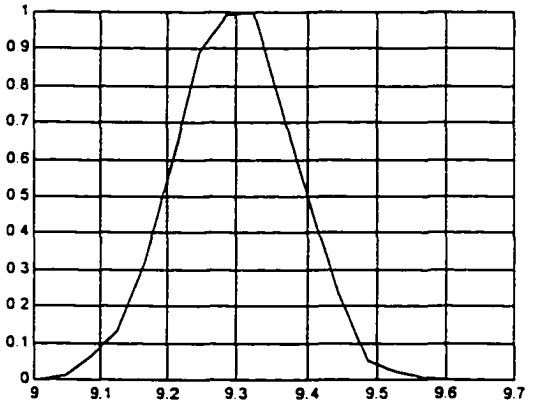

Figure 5.14: Irradiance distribution for λ = 675 nm (red) channel

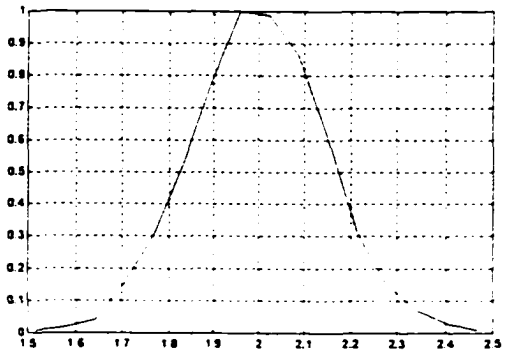

Figure 5.15: Probability density of range estimates with the blue and green channels for a 4.0 dB SNR (μ = 1.998, σ^2 = 0.022)

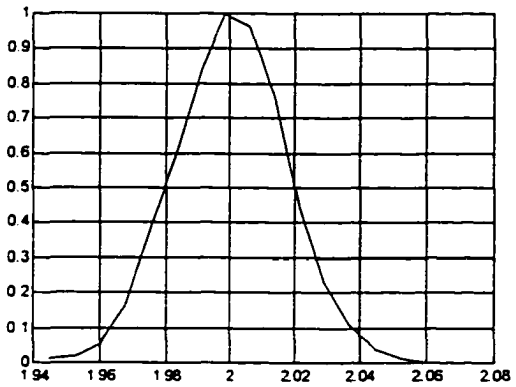

Figure 5.16: Probability density of range estimates with the blue and red channels for a 4.0 dB SNR (μ = 2.00, σ^2 = 0.0004)

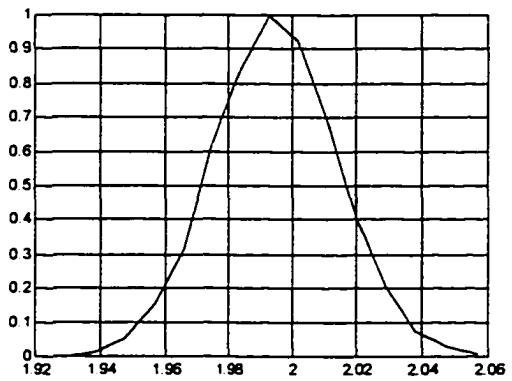

Figure 5.17: Probability density of range estimates with the green and red channels for a 4.0 dB SNR (μ = 1.992, σ^2 = 0.0004)

As discussed in Chapter 4, there will likely be scenarios where it is not practical to acquire a series of stationary images from each channel and estimate means. In such cases an improved estimate may be computed by weighting an combining the individual estimates. For example, in the previous system with 4 dB SNR the next range estimates are as follows:

$$d_{bg} = 1.8397\text{m} ; \qquad d_{br} = 1.9791 \text{ m}; \qquad d_{gr} = 1.9935 \text{ m}.$$

Taking the mean of the three estimates gives a final estimate of 1.9374 m yielding an error of 3.13 %. An improved estimate is obtained by weighting the individual estimates by channel variance as in Equation 5.3:

$$\hat{d} = d_{bg}\frac{\sigma_{br}^2+\sigma_{gr}^2}{2\left(\sigma_{bg}^2+\sigma_{br}^2+\sigma_{gr}^2\right)} + d_{br}\frac{\sigma_{bg}^2+\sigma_{gr}^2}{2\left(\sigma_{bg}^2+\sigma_{br}^2+\sigma_{gr}^2\right)} + d_{gr}\frac{\sigma_{bg}^2+\sigma_{br}^2}{2\left(\sigma_{bg}^2+\sigma_{br}^2+\sigma_{gr}^2\right)} \text{ m.} \qquad (5.5)$$

This yields a final estimate of 1.9837 m reducing error to only 0.82%.

5.2.3 Results Using the Kirlin Algorithm

This Section presents results using the parameter estimation algorithm developed by Kirlin and adapted in Section 4.3.2. The parameter of primary interest is d, however in the transfer function for propagation of light through water, γ is also a geometric parameter that must be estimated. Two modes of application for this algorithm are envisaged: the first is to employ it to estimate the shape of a surface relative to a point (pixel) of known distance from the camera; the second is to use it in an iterative fashion to generate the "optimal" parameter estimates from an objective function. The intent in this dissertation is not to conduct a comparison and analysis of optimization techniques, but rather to study the suitability of this gradient type to the multi-channel, multi-parameter estimation of related functions. In this case we optimize (minimize)

$$\hat{\delta}_\alpha = \left(\mathbf{G}^T\mathbf{G}\right)^{-1}\mathbf{G}^T\mathbf{D}_I^{-1}\delta_E \tag{5.6}$$

where $\hat{\delta}_\alpha$ is the estimated difference between a vector of nominal parameter values and the actual values, and is defined as

$$\hat{\delta}_\alpha = \begin{bmatrix} \cos(\gamma) - \cos(\gamma_o) \\ d - d_o \\ (d - d_o)^2 \end{bmatrix}. \tag{5.7}$$

The matrix **G**, derived from derivatives of the transfer function with respect to the unknown parameters is

$$\mathbf{G} = \begin{bmatrix} \frac{e^{-2c(\lambda_1)d_o}\rho(\lambda_1)}{d_o^2} & -2e^{-2c(\lambda_1)d_o}\cos(\gamma_o)\rho(\lambda_1)\left(\frac{1}{d_o^3} + \frac{c(\lambda_1)}{d_o^2}\right) & e^{-2c(\lambda_1)d_o}\cos(\gamma_o)\rho(\lambda_1)\left(\frac{3}{d_o^4} + \frac{4c(\lambda_1)}{d_o^3} + \frac{2c(\lambda_1)^2}{d_o^2}\right) \\ \mathbf{M} & \mathbf{M} & \mathbf{M} \\ \frac{e^{-2c(\lambda_N)d_o}\rho(\lambda_N)}{d_o^2} & -2e^{-2c(\lambda_N)d_o}\cos(\gamma_o)\rho(\lambda_N)\left(\frac{1}{d_o^3} + \frac{c(\lambda_N)}{d_o^2}\right) & e^{-2c(\lambda_N)d_o}\cos(\gamma_o)\rho(\lambda_N)\left(\frac{3}{d_o^4} + \frac{4c(\lambda_N)}{d_o^3} + \frac{2c(\lambda_N)^2}{d_o^2}\right) \end{bmatrix} \tag{5.8}$$

It is instructive to look at the behavior of the algorithm's parameter estimates independently: first when d is unknown and γ is known; then when d is known and γ is not; finally when neither d nor γ are known. If d actual is 2 m and γ actual is 60°, the irradiances measured in five spectral bands in the absence of noise are:

$$\mathbf{E} = \begin{bmatrix} 83.790 \\ 56.166 \\ 37.649 \\ 25.237 \\ 16.917 \end{bmatrix} \ \mathrm{W/m^2}.$$

Assuming nominal parameter values of d_o = 1 m and γ_o = 60° yields an irradiance estimate of:

$$\mathbf{E_0} = \begin{bmatrix} 409.365 \\ 335.160 \\ 274.406 \\ 224.665 \\ 183.940 \end{bmatrix} \text{ W/m}^2 .$$

The resulting computed deviation using Eqn. 5.6 (or equivalently Eqn. 4.72) is

$$\hat{\delta}_\alpha = \begin{bmatrix} -0.079 \\ 0.512 \\ 0.143 \end{bmatrix}.$$

From which final parameter estimates using Eqn 4.71 are

$$\hat{\gamma} = \cos^{-1}\left(\alpha_{\cos(\gamma_o)} + \cos(\gamma_o)\right) = \cos^{-1}(-0.079 + \cos(60)) = 65.102°;$$

$$\hat{d} = \alpha_{d_o} + d_o = 0.512 + 1.000 = 1.512\,m .$$

Clearly there is a 25.6% improvement in the estimate of d, but at the expense of an 8.5% error in the estimate of γ.

Setting nominal parameter values d_o = 2 m, the correct value, and γ_o = 50° yields an estimated irradiance of:

$$\mathbf{E_0} = \begin{bmatrix} 107.718 \\ 72.206 \\ 48.401 \\ 32.444 \\ 21.748 \end{bmatrix} \text{ W/m}^2 ,$$

and the resulting estimated deviation using Eqn. 5.6 is

$$\hat{\delta}_{\alpha} = \begin{bmatrix} -0.143 \\ 0.000 \\ 0.000 \end{bmatrix}.$$

In this case, when the nominal estimate for d was correct, the computed deviation of d_o is zero, even though $\gamma_0 \neq \gamma$. This characteristic, which is true for all γ_0 makes Kirlin's algorithm a very useful supplement to the intensity–range transformation. Using the range extracted by the intensity–range transformation, Kirlin's algorithm can be used to check the accuracy of the estimate (if $\hat{d} = d$, rows 2 and 3 of $\hat{\delta}_{\alpha}$ are 0) and return information on the orientation of the surface "pixels". The final parameter estimates in this case are:

$$\hat{\gamma} = \cos^{-1}\left(\alpha_{\cos(\gamma_o)} + \cos(\gamma_o)\right) = \cos^{-1}\left(-0.143 + \cos(50)\right) = 60.000^{o};$$

$$\hat{d} = \alpha_{d_o} + d_o = 0.000 + 2.000 = 2.000\,m,$$

which are the actual values. When d is known precisely, convergence to the correct value of γ is expected in one iteration since the quadratic Taylor expansion in Equation 4.45, and subsequent algorithm development is exact for $\cos(\gamma)$. Figure 5.18 is a plot of the computed deviation of γ_o as a function of actual deviation when $d_o = d$.

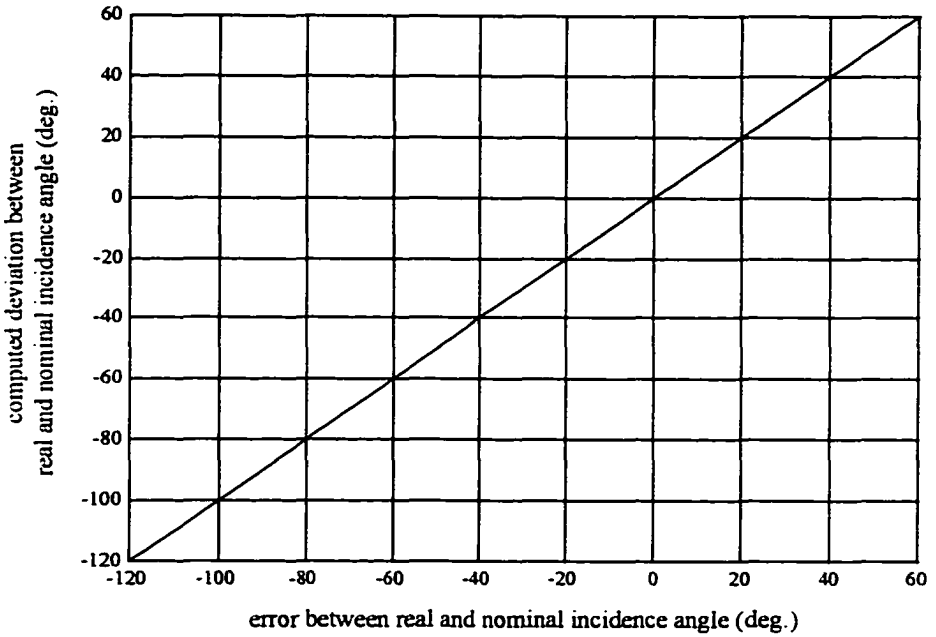

Figure 5.18: Estimated versus actual orientation deviation using Kirlin's algorithm with known range

Examining further the utility of using this approach to test, and perhaps improve estimates of d, we examine the response to very small nominal range deviations, on the order of 10^{-3}m. Starting with nominal parameter values $d_o = d \pm 10^{-3}$m and $\gamma_o = 50^\circ$ (recall $\gamma = 60^\circ$), the computed deviation vectors are:

$$\hat{\delta}_\alpha\big|_{d_o=1.999} = \begin{bmatrix} -0.143 \\ 0.001 \\ 0.000 \end{bmatrix} \text{ and } \hat{\delta}_\alpha\big|_{d_o=2.001} = \begin{bmatrix} -0.143 \\ -0.001 \\ 0.000 \end{bmatrix},$$

which indicate that d_o is not correct and returns the correct deviation. Figures 5.19 and 5.20 plot the computed range deviation for the nominal values of $\gamma_o = 50^\circ$ and d_o in the neighborhood of d. Figure 5.21 plots the error in computed deviation in $\cos(\gamma)$. Figures 5.19 and 5.21 demonstrate how, for nominal range deviations within ± 0.5 m, convergence

convergence to the actual solution is achievable. Over larger intervals convergence is still possible but requires consideration of all parameters.

With an actual range d = 2.0 m and $\gamma = 60^{o}$, d_o is varied from 0 to 10 m with γ_o set to 30^{o}. The resulting error in computed deviation is plotted in Figure 5.22. Figure 5.23 is the same data as in Figure 5.22 but expanded in the range $-2.00 \le (d_o - d) \le 2.00$. This Figure shows that the range deviation estimate is not a monotonic function and returns at least two values of d_o for which the computed error is zero. A similar result is encountered at longer actual ranges as illustrated in Figure 5.24 for d = 8.0 m. The correct d_o estimate becomes evident by considering the remaining data returned by this algorithm, namely $\{\cos(\gamma) - \cos(\gamma_0)\}$ and $\{(d - d_o)^2\}$. Figure 5.25 illustrates how the inflection in $\{\cos(\gamma) - \cos(\gamma_0)\}$ and the minima in $\{(d - d_o)^2\}$ both occur when the nominal estimate of range is equivalent to the actual range regardless of γ_0. It should also be noted in Figure 5.25 that the estimate of $d - d_o$ is made independently (in a non-statistical sense) from the estimate of $(d - d_o)^2$. This explains why there can be two zero crossings of the $(d - d_o)$ parameter but only one zero (a minima) in the estimates of $(d - d_o)^2$. Hence there are, in effect three range estimates, $\hat{d}_i$.

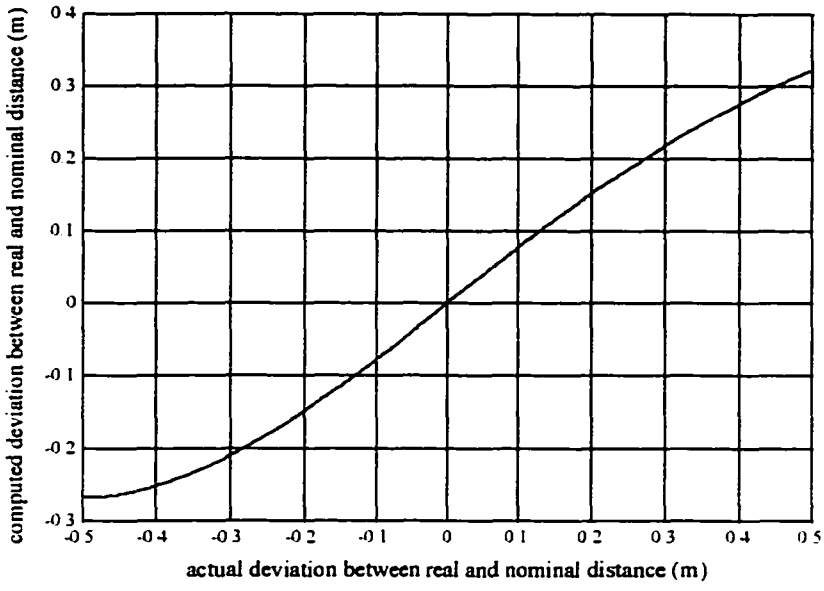

Figure 5.19: Estimated versus actual range deviation using Kirlin's algorithm with a 10^{o} error in γ_o

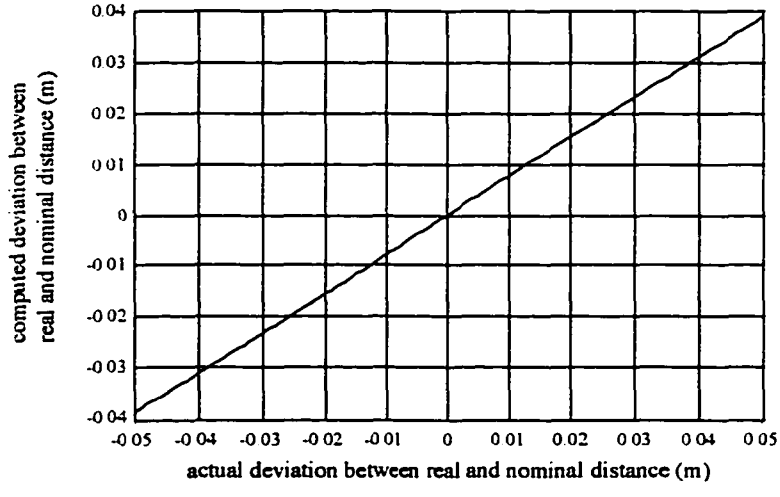

Figure 5.20: Figure 5.19 expanded about $d - d_o = 0$

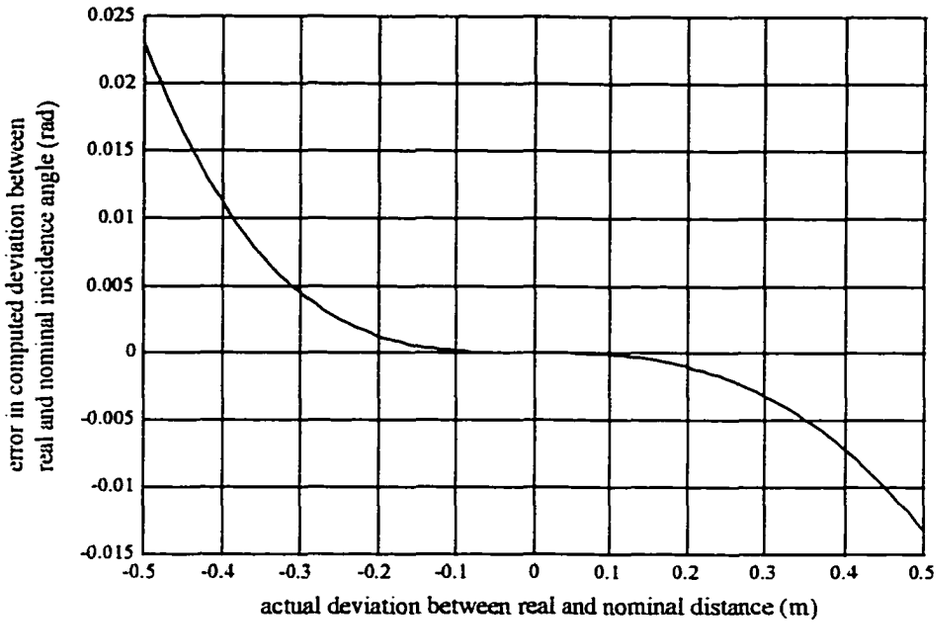

Figure 5.21: *Error* in computed deviation of cos(γ) as a function of error in d_o.

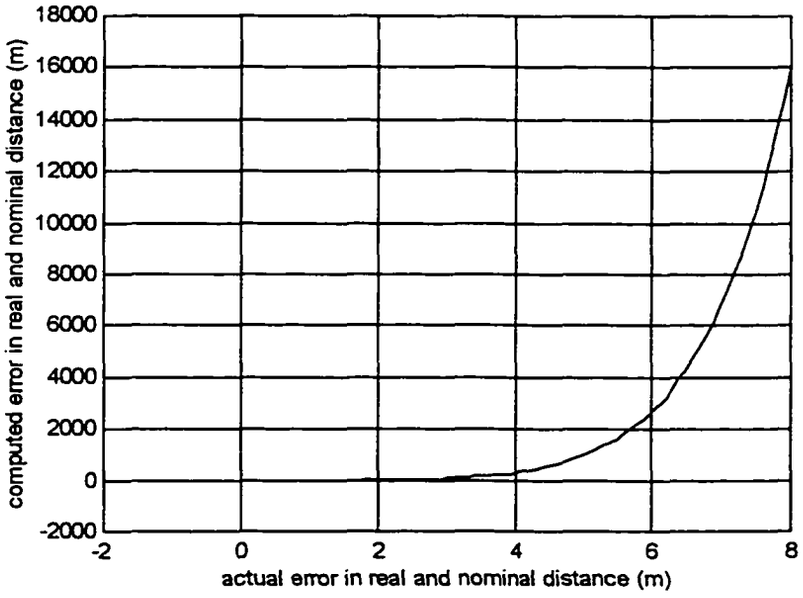

Figure 5.22: Computed deviation in d_o as a function of d_o - d

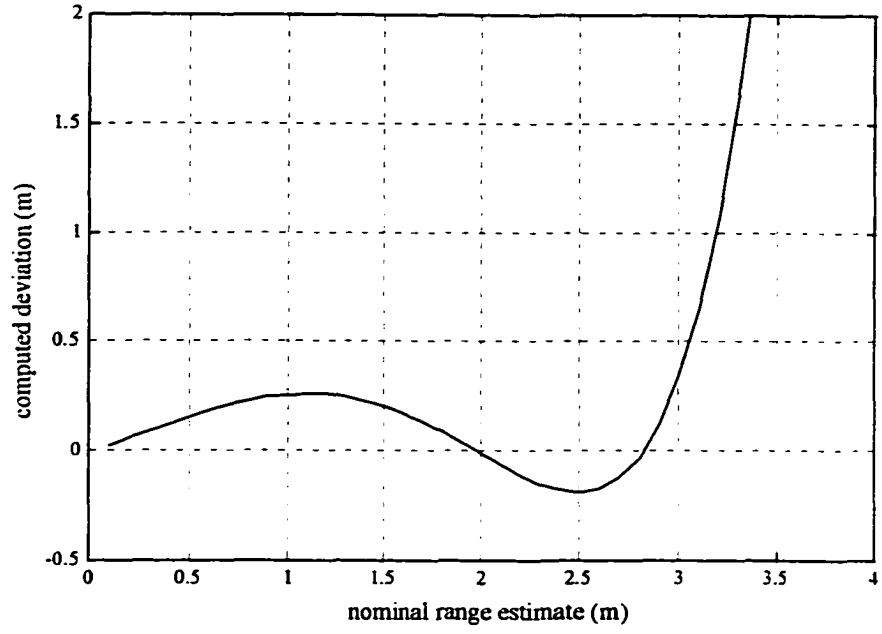

Figure 5.23: Computed deviation (d - d_o) as a function of d_o with d = 2m

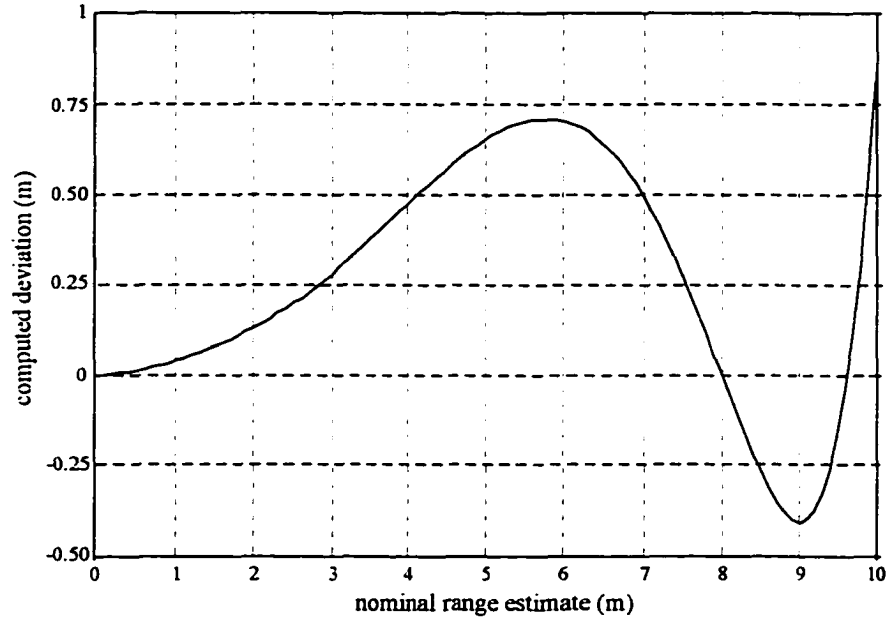

Figure 5.24: Computed deviation d - d_o as a function of d_o with d = 8m

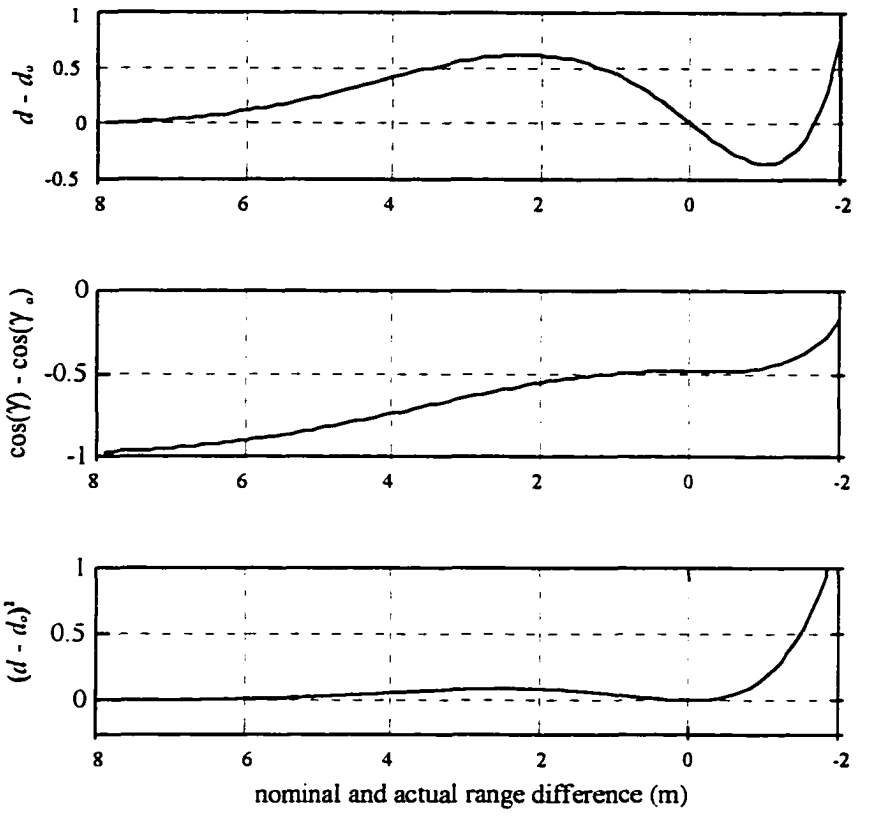

Figure 5.25: Computed deviation $d - d_o$, $\cos(\gamma) - \cos(\gamma_0)$, and $(d - d_o)^2$ as a function of $d - d_o$ with $d = 8$m

The performance of this algorithm should also be considered in noise. In doing so, effective operation required restricting the search for critical points to a truncated interval. In the following case, actual range was 2.0 m and the search interval extended over 1.0 m $\leq d_o \leq$ 3.0 m. By using the algorithm in conjunction with other sensors or estimation techniques like the intensity–range transformation such "shepparding" is practical and improves computational efficiency. Figure 5.26 illustrates the distribution of estimates using five spectral channels, each with an SNR of 4.0 dB. Figure 5.27 plots parameter estimation error for SNR from 0 to 10 dB. At SNR < 4.0 dB instances were noted when critical points were not detected and a range of 0 m was assigned.

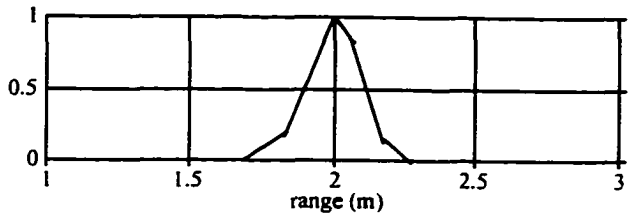

Figure 5.26a: Distribution of range estimates based on cos(γ) inflection

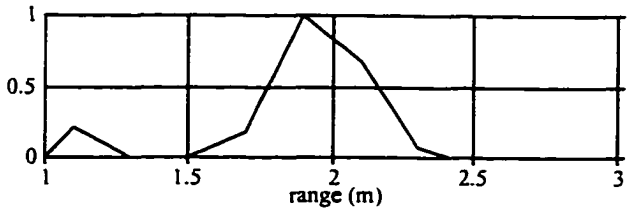

Figure 5.26b: Distribution of range estimates based on *d* zero crossing

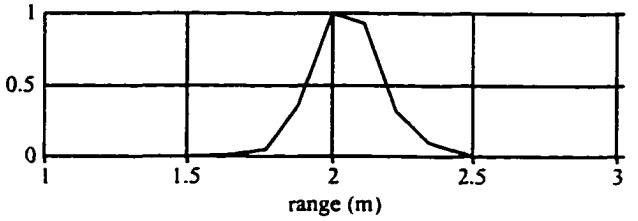

Figure 5.26c: Distribution of range estimates based on d^2 minima

Figure 5.26: Distribution of range estimates for 4.0 dB SNR

Figure 5.27 illustrates the effectiveness of this algorithm for moderate and high SNRs. As noise increases and SNR decreases below 5 dB, estimation error increases rapidly. The apparant "flattening" at SNRs of 2 dB and less is due to the artificial bound on error imposed by the truncated search region and default to an estimate of 0 m if no critical point was found (the actual range was 2 m).

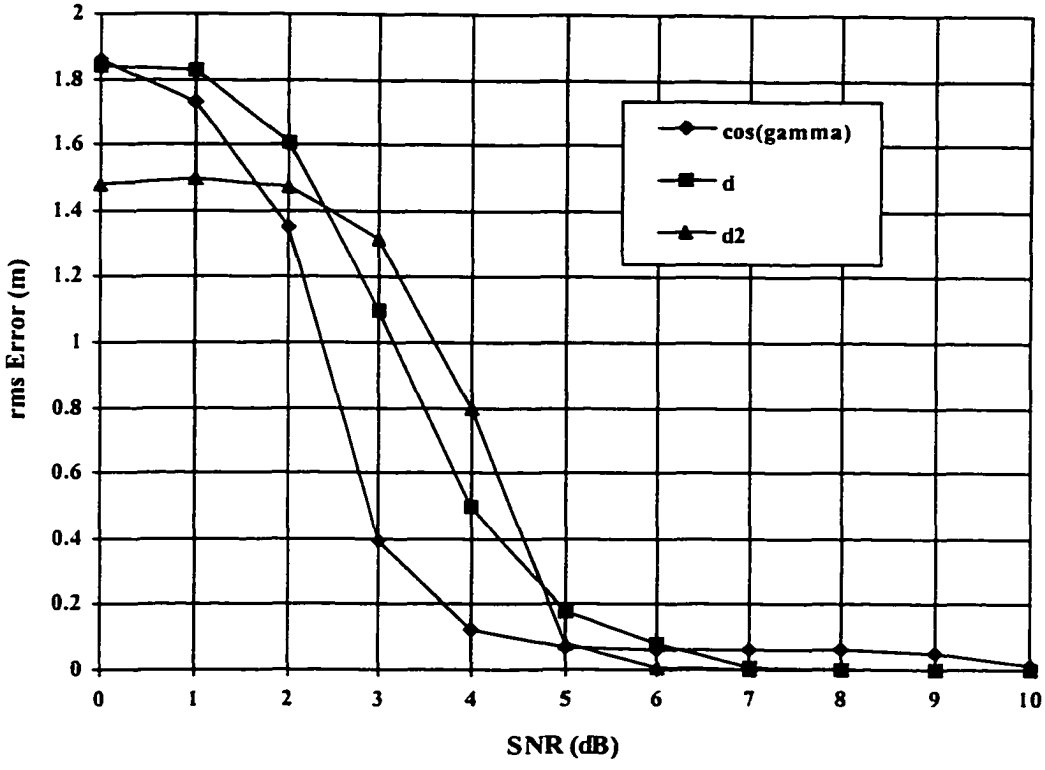

Figure 5.27: RMS error as a function of SNR using Kirlin's algorithm with 5 spectral channels

A final range estimate is computed from the three estimates returned by the Kirlin algorithm. The variance of each estimate is similar, as shown by Figure 5.27, hence each estimate is weighted equally. This final range estimate is plotted in Figure 5.28 as a function of SNR. The characteristics described for the individual estimates plotted in Figure 5.27 are also evident in this plot but with the expected overall decrease in error.

The significant increase in error with decrease in SNR is not unprecedented when using derivative-based methods in underwater machine vision applications. Yu, in developing a technique to extract orientation of planar surfaces using a monochromatic light source, reported a similar effect [70]. Nonetheless, this algorithm does return

additional and independent information from the intensity–range transformation and is considered a complementary process for future developments.

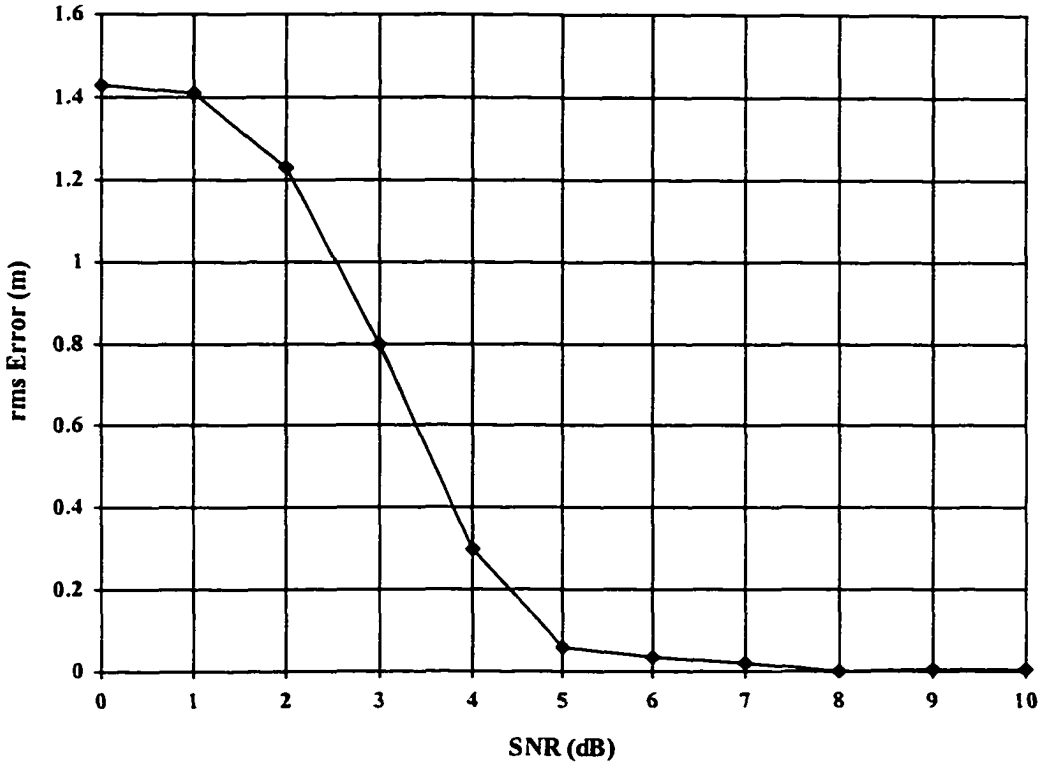

Figure 5.28: RMS error as a function of SNR of final range estimate using Kirlin's algorithm with 5 spectral channels

5.3 Performance in a Scattering Medium

5.3.1 Scattering Parameters and Effects on Image Formation

In terms of describing the transmission of light in water, there are no "correct" parameter values for sea water. They vary with region, season, depth, and prevailing environmental conditions. The simulator model uses empirical constants to generate forward and backscatter irradiance for complete image formation. The three constants are:

B which determines the width of the PSF, or the amount of blurring. As B increases, so does the width of the PSF.

G which determines the attenuation of the scattered irradiance (in addition to the attenuation coefficients). As G increases, overall magnitude of scattered irradiance decreases.

β which specifies the amount of light scattered back from the medium.

The magnitude of these constants have little intuitive correspondence with image appearance and, as in nature, the effects vary as a function of range. This Section therefore, presents a series of plots and images illustrating changes in image appearance due to variations in B, G, and β. Again the scene is a brick protruding 0.10 m above the seabed. Both the brick and the seabed have the same reflectance – as if both were covered in silt.

Figures 5.29 to 5.33 are a series of plots and images with G = 0.01 and constant while B varies from 0.000 to 0.015. Range to the nearest point on the seabed was 10 m. To elucidate the changes in forward scatter, backscatter irradiance is omitted from this series of figures; the image contains the direct and forward scattered components only. In each

Figure, (a) is the unenhanced image, (b) is the same data with contrast enhancement[1], (c) is a plot of the irradiance data.

The contrast enhanced image is somewhat misleading in that it implies the brick is visible under most of these scattering conditions. However, in the unenhanced images the brick is visible only in Figures 5.29 and 5.30, and becomes indistinguishable as scattering is further increased in Figure 5.31 and beyond.

The smearing due to increased scattering is also evident from the irradiance levels on the z axis in plot (a) of each figure. The lowest pixel irradiance is approximately 37 W/m^2 for each plot but as scattering increases and the salient component (the brick) of the image becomes increasingly smeared, the irradiance scale peak decreases from 39.5 W/m^2 to 37.8 W/m^2. The most obvious indication of scattering in the plots is the increasing blurring of the interface between the brick and the seabed, and the "peaks" developing on the top side of the brick.

Figure 5.34 illustrates the increase in forward scattering as a function of range. In this series of images B = 0.010 and they again consist of direct and forward scattered irradiance. As range increases the glow field, or scattered components of light become increasingly predominant in image formation [29]. This phenomena is evident here as the brick appears increasingly blurred due to the increasing contribution of forward scattering.

---

[1] contrast enhancement intensity scaling provided by the "imagesc.m" function in Matlab®

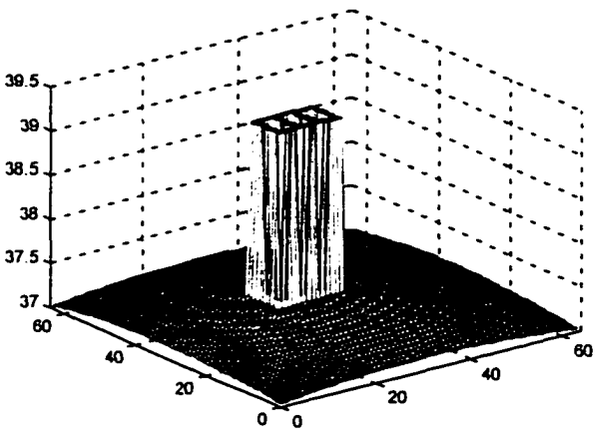

(a)

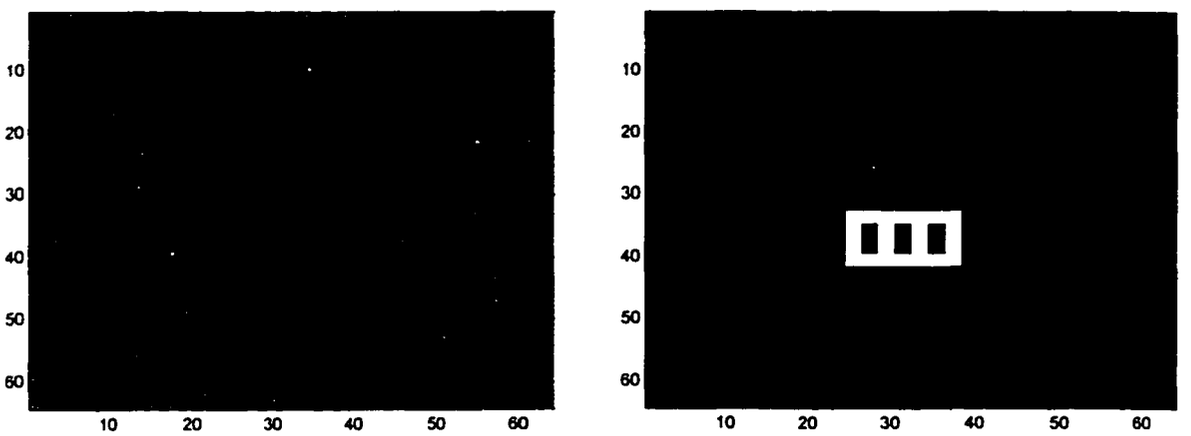

(b) (c)

Figure 5.29: Irradiance plot and image with B = 0.000

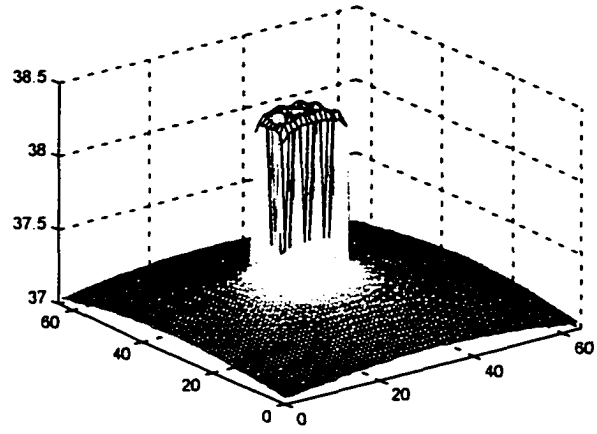

(a)

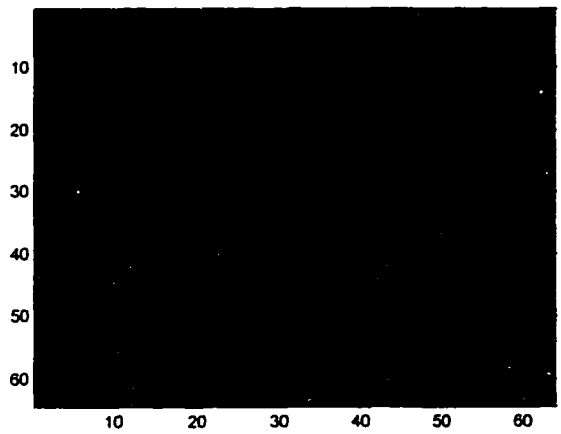

(b)

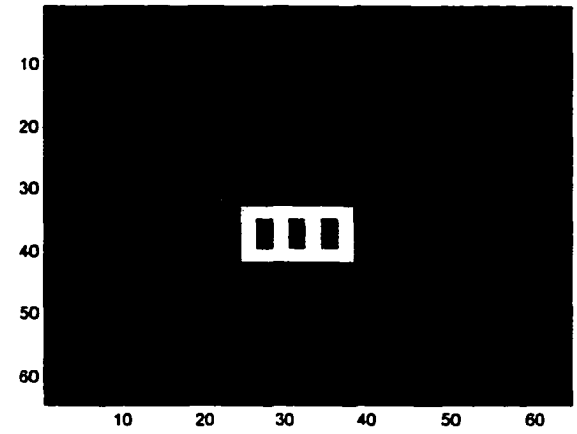

(c)

Figure 5.30: Irradiance plot and image with B = 0.001

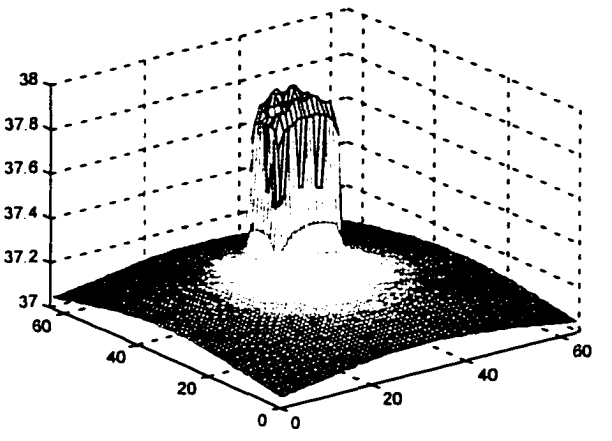

(a)

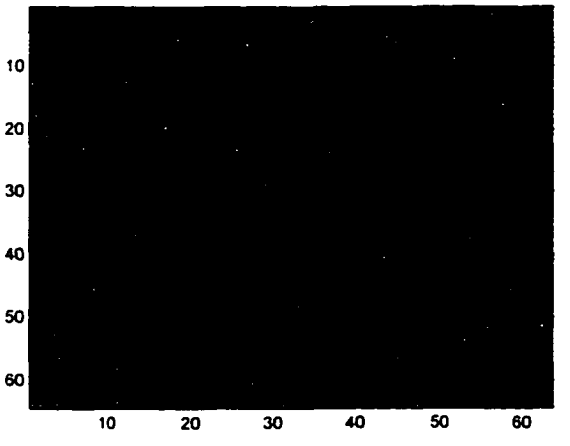

(b)

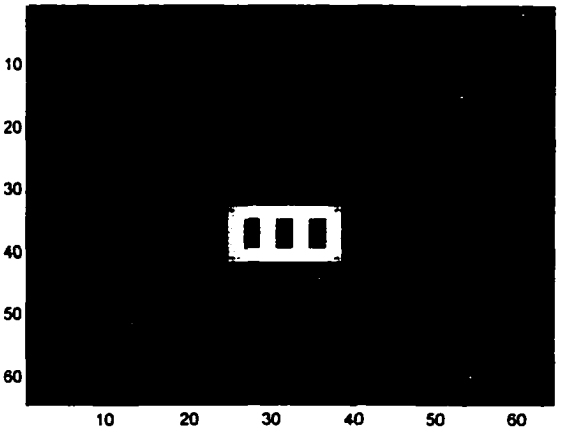

(c)

Figure 5.31: Irradiance plot and image with B = 0.005

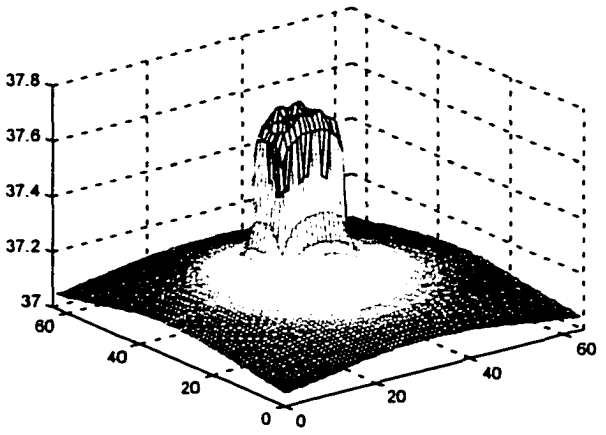

(a)

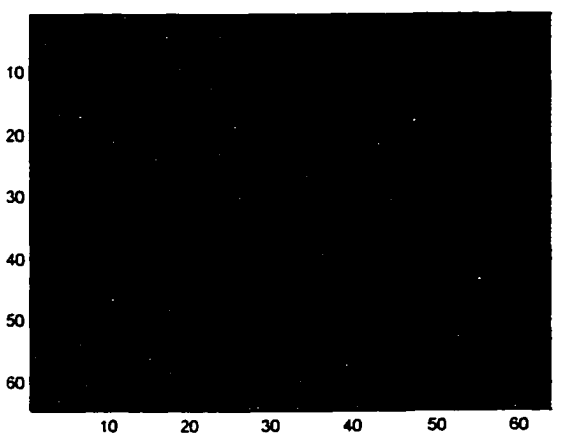

(b)

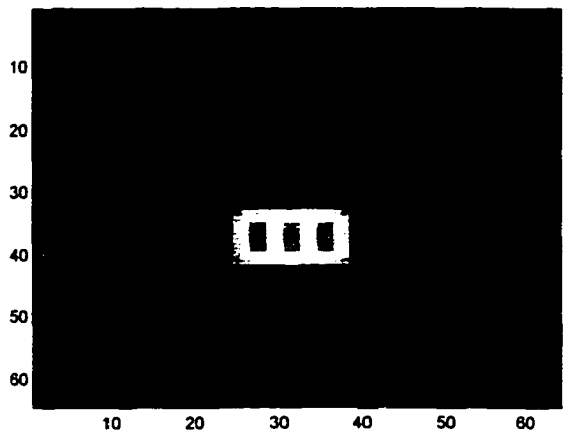

(c)

Figure 5.32: Irradiance plot and image with B = 0.010

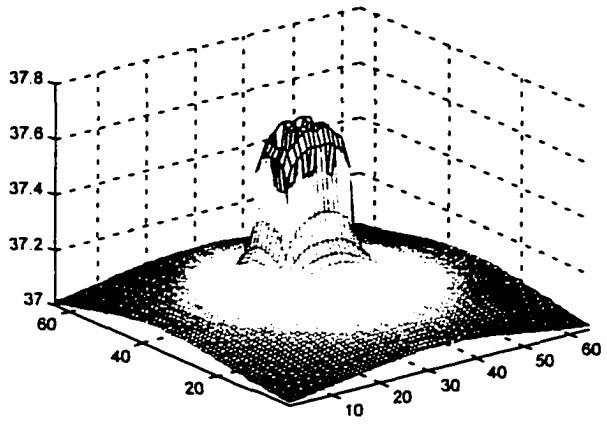

(a)

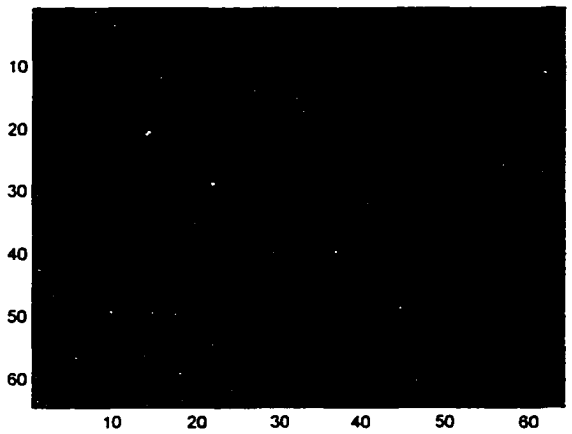

(b)

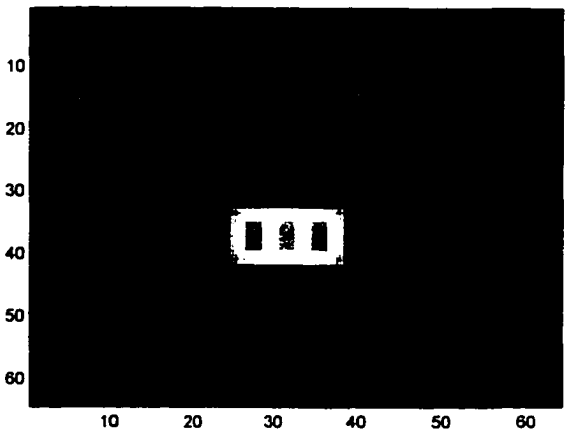

(c)

Figure 5.33: Irradiance plot and image with B = 0.015

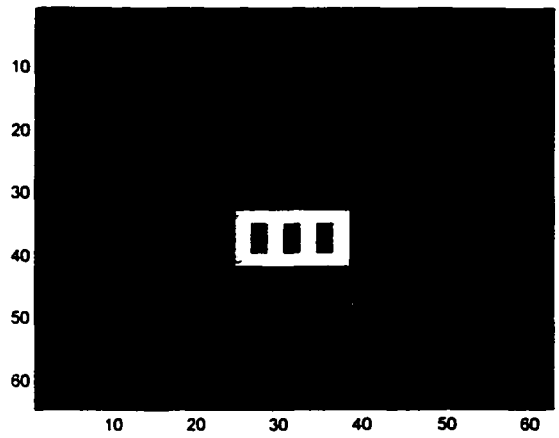

(a) range = 5 m

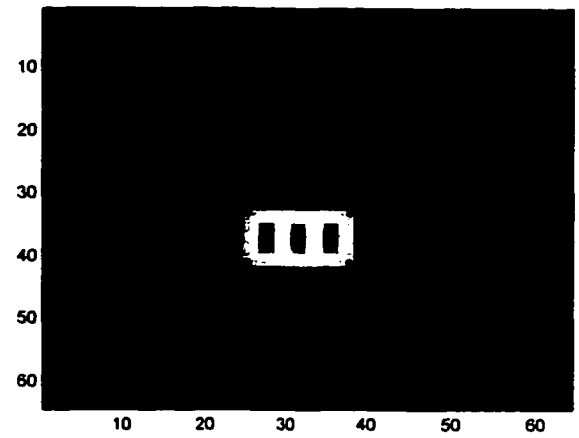

(b) range = 10 m

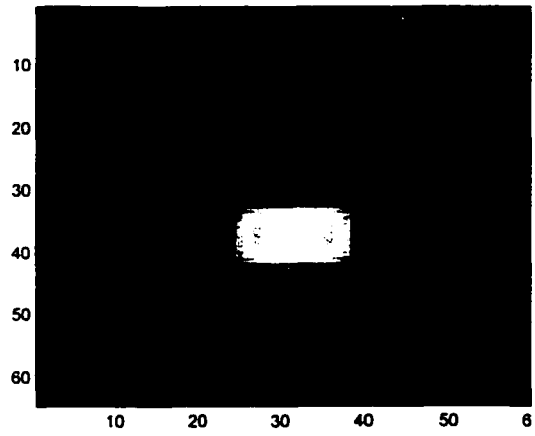

(a) range = 5 m

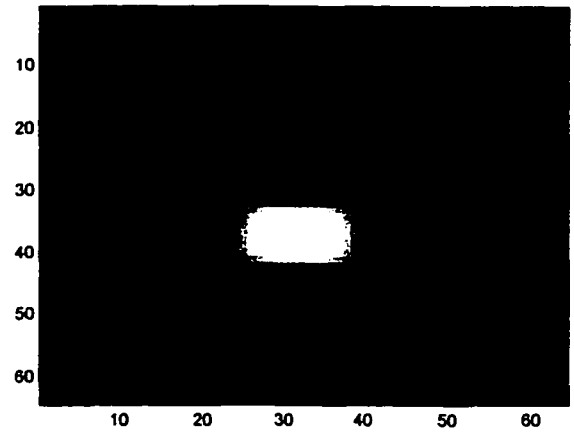

(b) range = 10 m

Figure 5.34: Images formed from direct and forward scattered light at 5, 10, 15, and 20 m

Now backscatter is introduced to form the total image. Figures 5.35 to 5.38 are images resulting from increasing amounts of backscatter. Again the apparent and enhanced images are shown. The range for this series of images was reduced to 6 m. With $\beta = 0$, the image in Figure 5.35 contains only direct and forward scattered irradiance and the contrast in the enhanced image is high. The brick can also be seen in the unenhaced image. As backscatter is introduced the brick is masked or "washed out" as contrast decreases. In Figure 5.38, with $\beta = 0.010$ the brick is even fading in the enhanced image.

Backscattered light has two effects; it reduces the contrast in the image as described, and it increases the overall intensity of the image as can be seen from the increased brightness of the unenhanced images and from the irradiance plots. The enhanced images show that well after unenhanced images appear to show nothing other than backscatter, details about object contours are still available. Further, results in the next section show that even after the object is completely "buried" by scattered light, information about overall surface range can still be extracted.

Finally, Figures 5.39 to 5.42 are apparent and enhanced images for a surface at 2, 4, 6, and 8 m respectively. Scattering is high and constant with $B = 0.010$ and $\beta = 0.010$. (These are the scattering levels that will be most often used in the next section.) Focal length was adjusted to maintain a constant brick size in each image. Relative irradiance levels between the unenhanced images is not significant since effective shutter speed was reduced to avoid saturation at the near ranges. Nonetheless, it is interesting to note that the brick is visible in the 2m unenhanced image but not at greater ranges. Most significant in these images is the obvious increase in the effects of scattering with increased range. Beyond 8 m the brick is indistinguishable in both the apparent and enhanced images.

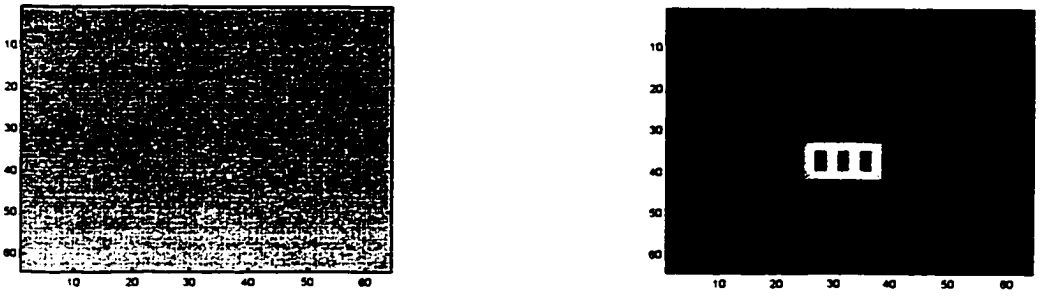

Figure 5.35: Apparent and enhanced images for B = 0.010, β = 0, range = 6 m

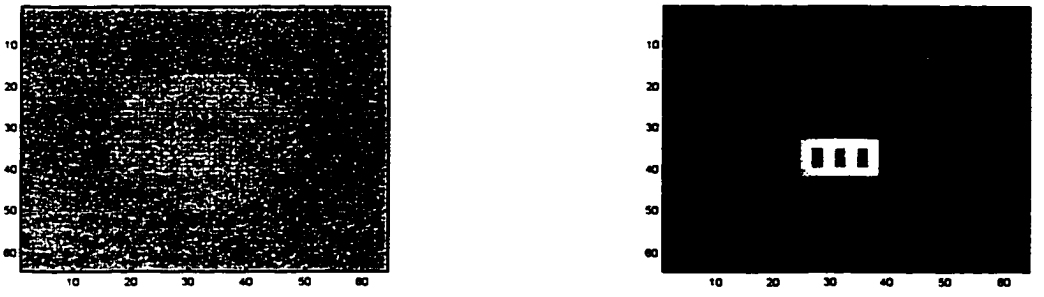

Figure 5.36: Apparent and enhanced images for B = 0.010, β = 0.001, range = 6 m

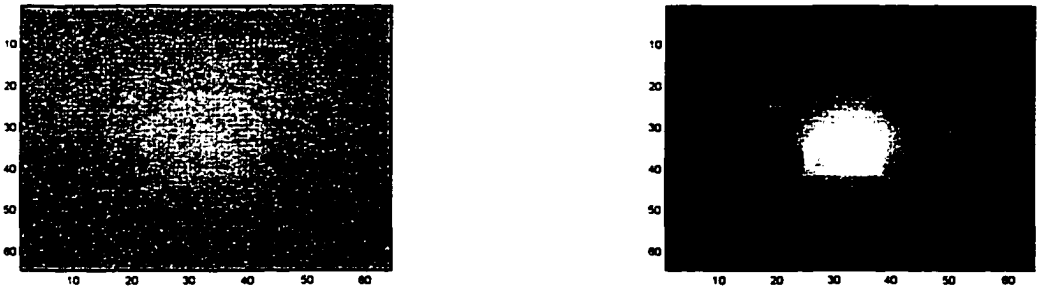

Figure 5.37: Apparent and enhanced images for B = 0.010, β = 0.005, range = 6 m

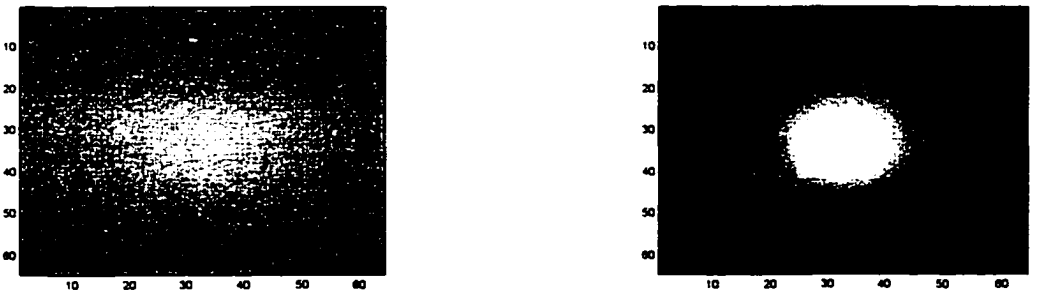

Figure 5.38: Apparent and enhanced images for B = 0.010, β = 0.010, range = 6 m

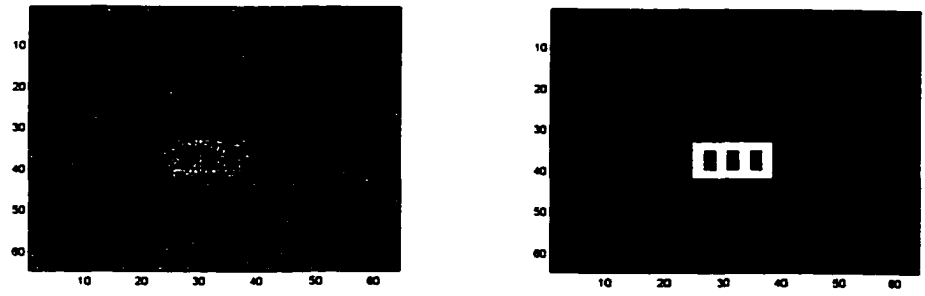

Figure 5.39: Apparent and enhanced images for B=0.010, $\beta = 0.010$, d =2 m

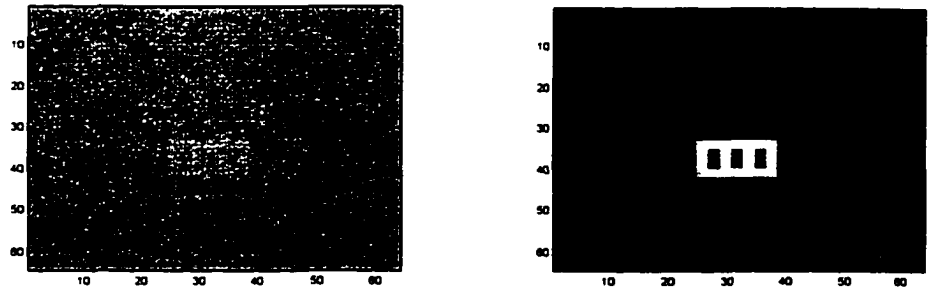

Figure 5.40: Apparent and enhanced images for B=0.010, $\beta = 0.010$, d =4 m

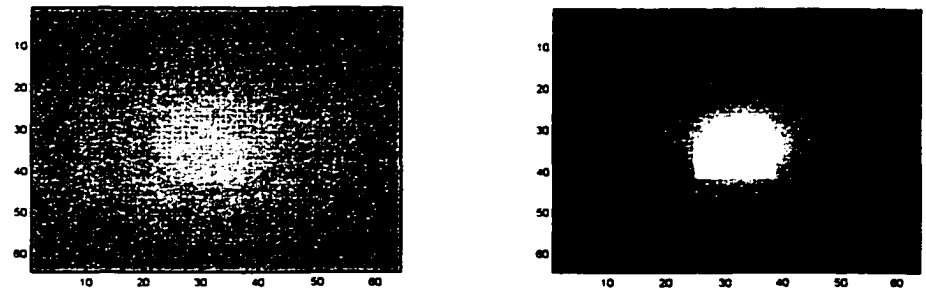

Figure 5.41: Apparent and enhanced images for B=0.010, $\beta = 0.010$, d =6 m

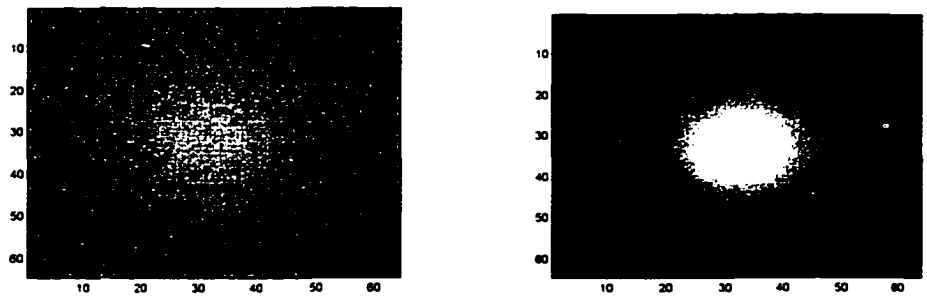

Figure 5.42: Apparent and enhanced images for B=0.010, $\beta = 0.010$, d =8 m

5.3.2 Results from a Scattering Medium

Section 5.3.1 presented images acquired over a range of medium conditions to provide an appreciation for the effect of medium parameter values on image formation. In this section, the response of the intensity–range transformation to systematic variation of those parameters are studied. Initially, results generated by the transformation under a variety of scattering conditions in the absence of other noise are presented. Various noise types and levels are then introduced.

Calibration data for this section is acquired from *in situ* calibration prior to each new test – as it would be in a working system. Because of scattering, the computed difference in attenuation coefficients typically differ from those specified as the IOPs in the simulator; the latter being:

c(blue) - c(green)	0.35;
c(blue) - c(red)	0.40;
c(green) - c(red)	0.05.

Analysis in Chapter 4 derived the importance of attenuation coefficient difference. That importance again manifests in this Chapter. Error is rms error computed over the entire range map as given in Equation 5.1. Using only direct irradiance (i.e. no scattering) with no additional noise added, rms error is consistently less than 10^{-16} m.

Figure 5.43 is a graph of rms error as a function of range with B = 0.010 and β ranging from 0.000 (no backscatter) to 0.010. Calibration was performed at 1 m and 2 m. For light backscatter (β = 0.000 to β = 0.001) the results are quite encouraging with the rms error in estimated range remaining to within 1 % of actual range, out to 10 m. Beyond 10 m estimate error increases more rapidly as a function of range and is 5.7 % at 20 m. Severe backscatter yields an rms error of 4.45 % at 10 m increasing to 8.2 % at 20 m. At a range of 10 m and further there is no evidence of the brick in the reconstructed range map and estimates primarily represent an "average" distance between the camera

and the surface. For ranges up to 6m the rms error is less than 1 % for all scattering conditions.

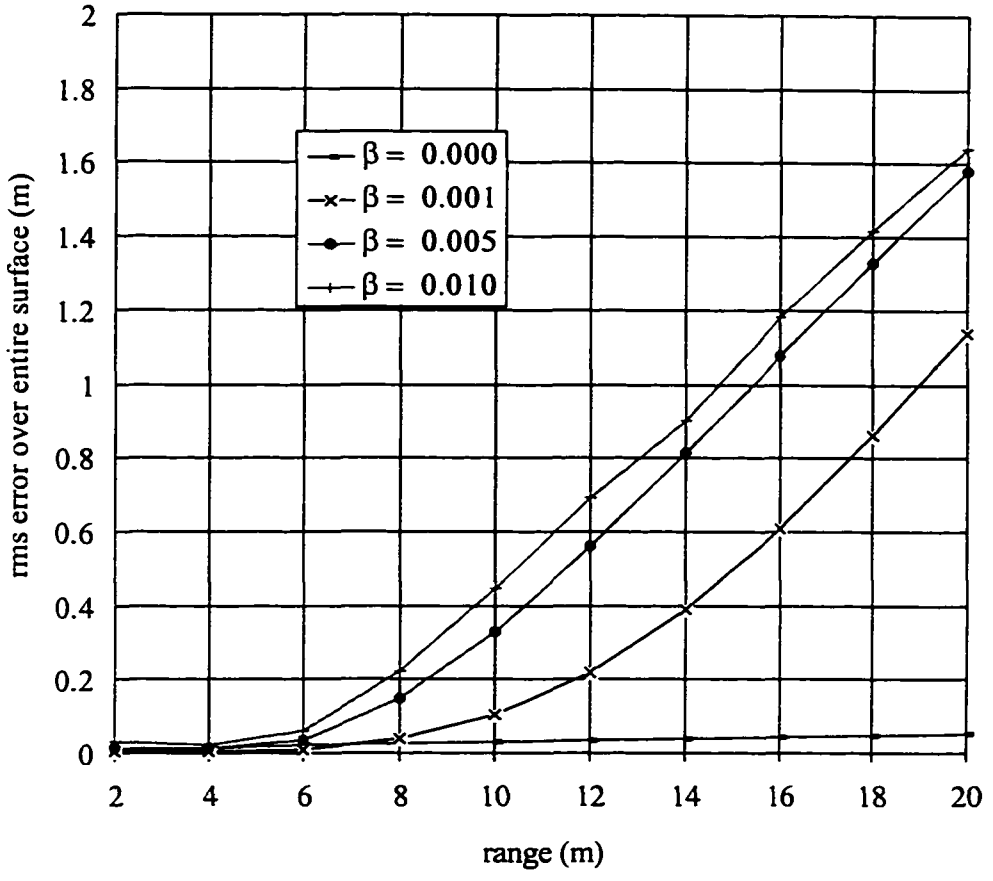

Figure 5.43: RMS error as a function of range under various backscatter conditions

The results in Figure 5.43 are from data acquired with the direct, forward scattered, and backscattered light. Recalling from Figure 5.42 in the previous section that the visibility limit for the most severe scattering modelled here is surpassed at 8 m, the results demonstrate that within the limits of visibility, rms error is on the order of 1 % of range or less. Also within this limit, there is little difference between results obtained with forward scattering only, and with both forward and backscattered light.

Machine vision systems are useful within the limits of their visibility. In practice, many underwater machine vision systems increase this visibility limit by reducing backscatter through range gating [50, 51, 53, 109, 110]. The intensity–range transformation will likely be used in a similar fashion. The following results are from a range gated system with backscatter only from the region extending a few cm in front of the surface being imaged.

Figures 5.44 and 5.45 illustrate the effects of scattering on range estimation for B ranging from 0.001 to 0.015. (The effect on image irradiance and appearance for this range of scattering was presented in Figures 5.29 to 5.33 in the previous section.) Three different rates of change in rms error as a function of range are evident in the figures. Water with B = 0.001 to 0.005 would, from the previous section, be considered to have good visibility and, in this case rms error increases gradually and almost linearly with range to a maximum of 2.17 cm at 20 m for B = 0.005. For moderate to severe scattering, B = 0.007 to 0.015, the rate of change in error as a function of range increases as range increases and is a maximum of 10.41 cm at 20 m. Results for B = 0.010 are mid-range in this category and this scattering condition will be maintained in future tests when other parameters are varied.

Within a 1 m range, Figure 5.44 illustrates that estimation error drops significantly as range decreases and at a range on 25 cm the maximum rms error less than 1.25 cm. This trend bodes well for a vision system using intensity–range transformed data in robotic applications such as manipulation and docking.

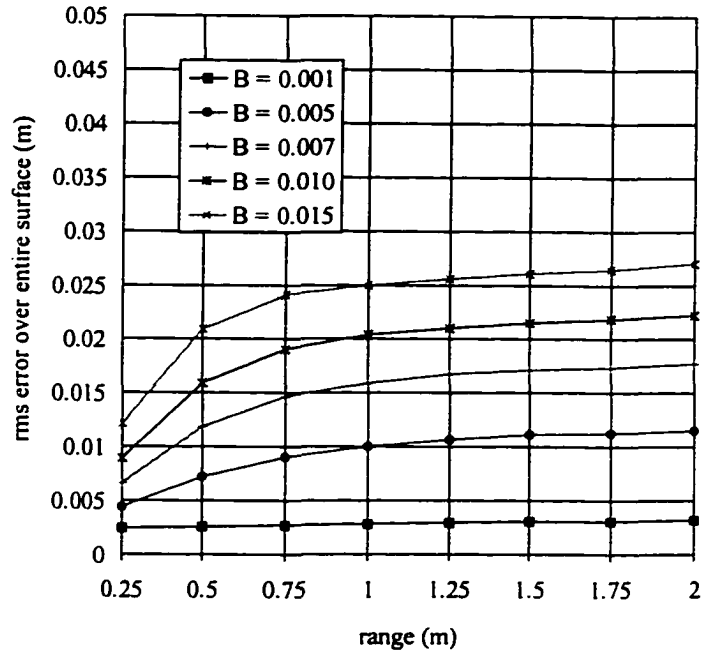

Figure 5.44: RMS error vs. range (0.25 to 2 m)with range gating and B = 0.001 to 0.015

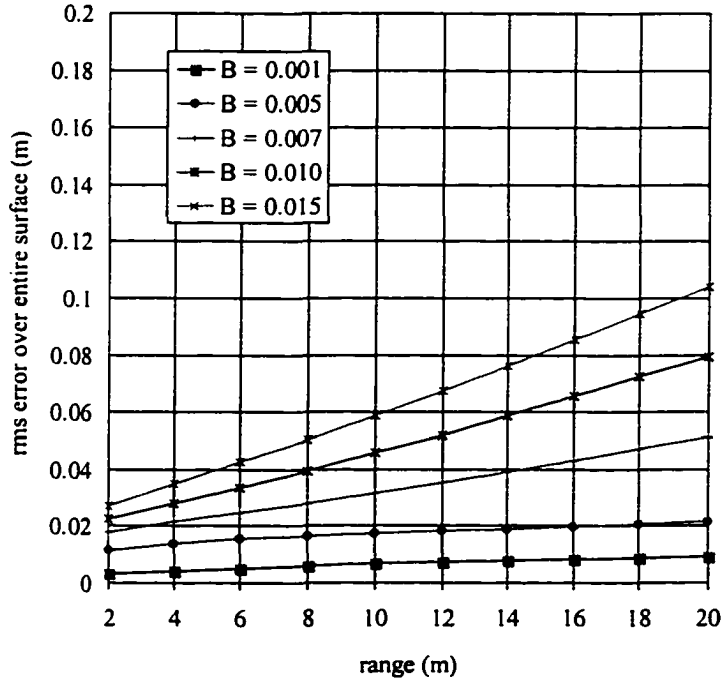

Figure 5.45: Fig. 5.44 with expanded ordinate

Figures 5.46 to 5.50 are intensity–range transformed plots for the brick embedded in the seabed at a range of 2 m, with B = 0 (no scattering) to B = 0.015. Part (a) of each figure is the transformed range map. The increased range with increased radius from the map centre is due to the perspective projection. Part (b) is the reconstructed scene with the perspective corrected. For values of B = 0.005 and greater, the edges of the corrected scene increasingly map to "curl up". This is an artifact of the simulator resulting from the finite area over which the PSF is convolved. The figures also show that as scattering increases, not only does the computed shape of the brick increasingly spread out, but the computed height above the seabed decreases. This is an inherent error due to the scattering within the medium.

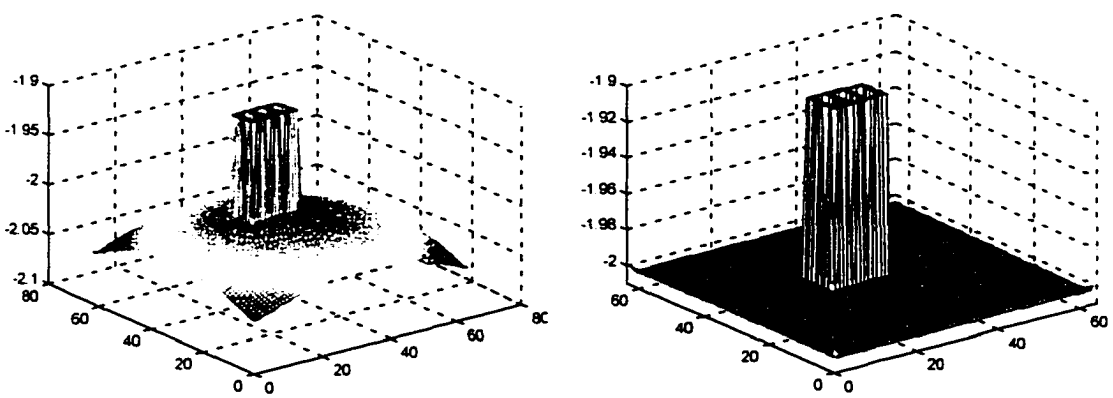

(a) range map (b) corrected scene

Figure 5.46: Intensity–range generated range map and reconstructed scene for B = 0

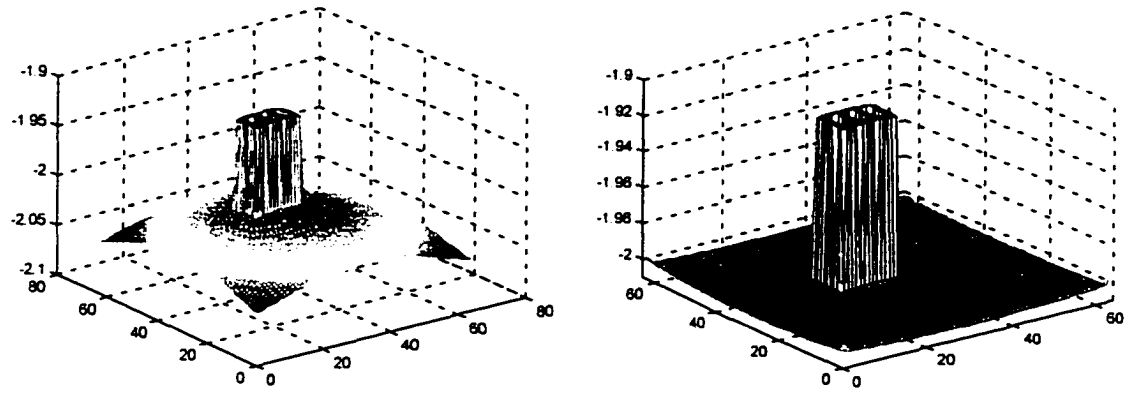

(a) range map (b) corrected scene

Figure 5.47: Intensity–range generated range map and reconstructed scene for B = 0.001

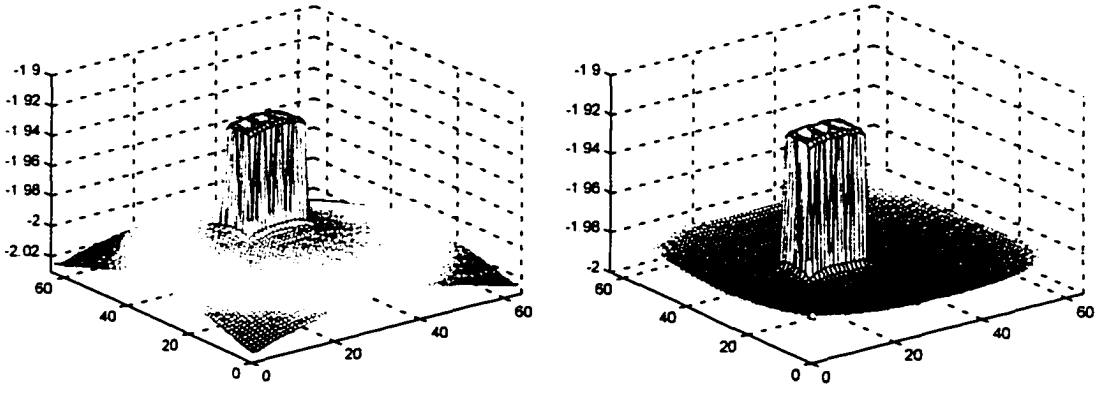

(a) range map (b) corrected scene

Figure 5.48: Intensity–range generated range map and reconstructed scene for B = 0.005

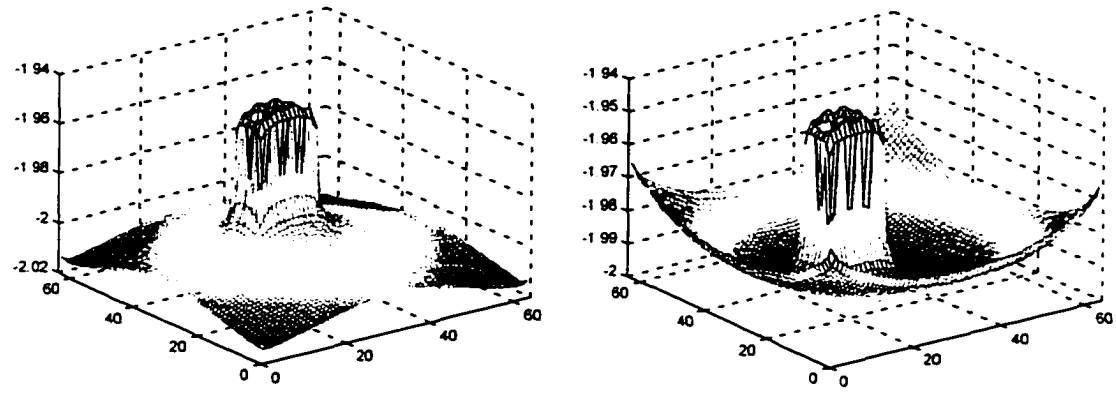

(a) range map (b) corrected scene

Figure 5.49: Intensity–range generated range map and reconstructed scene for B = 0.010

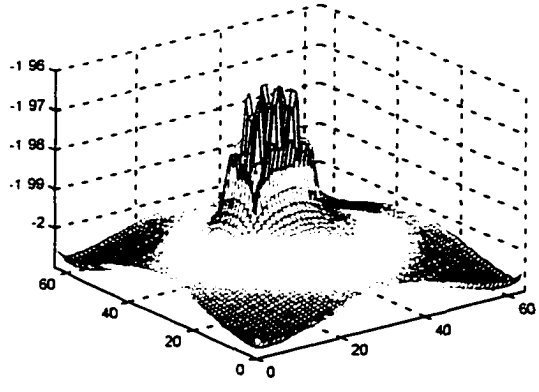

Figure 5.50: Intensity–range generated range map for B = 0.015

The results thus far in this section have been for a scattering medium with no additional system noise. For the next set of results a noise "floor" is added to the camera and the received irradiance is quantized to 8 or 16 bits. Shutter control is emulated by scaling irradiance such that the maximum irradiance is in the 226 quantile level for 8 bits or the 65250 quantile level for 16 bit digitization. Figure 5.51 plots the distribution of noise for 8 bit digitization.

Figure 5.52 is a plot of mean irradiance level at the camera as a function of range for the blue, green, and red channels with B = 0.10. From this plot it is apparent that distance computations using red irradiance will likely demonstrate significant error at ranges beyond a few meters. The corresponding SNR for each channel is listed in Table 5.1.

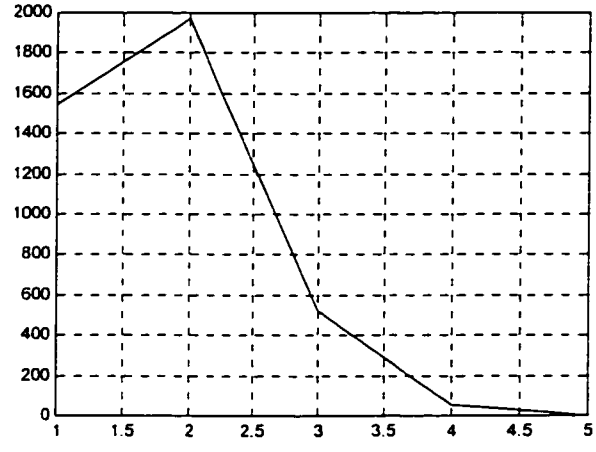

Figure 5.51: Noise floor added in addition to 8 bit quantization; mean = 0.736

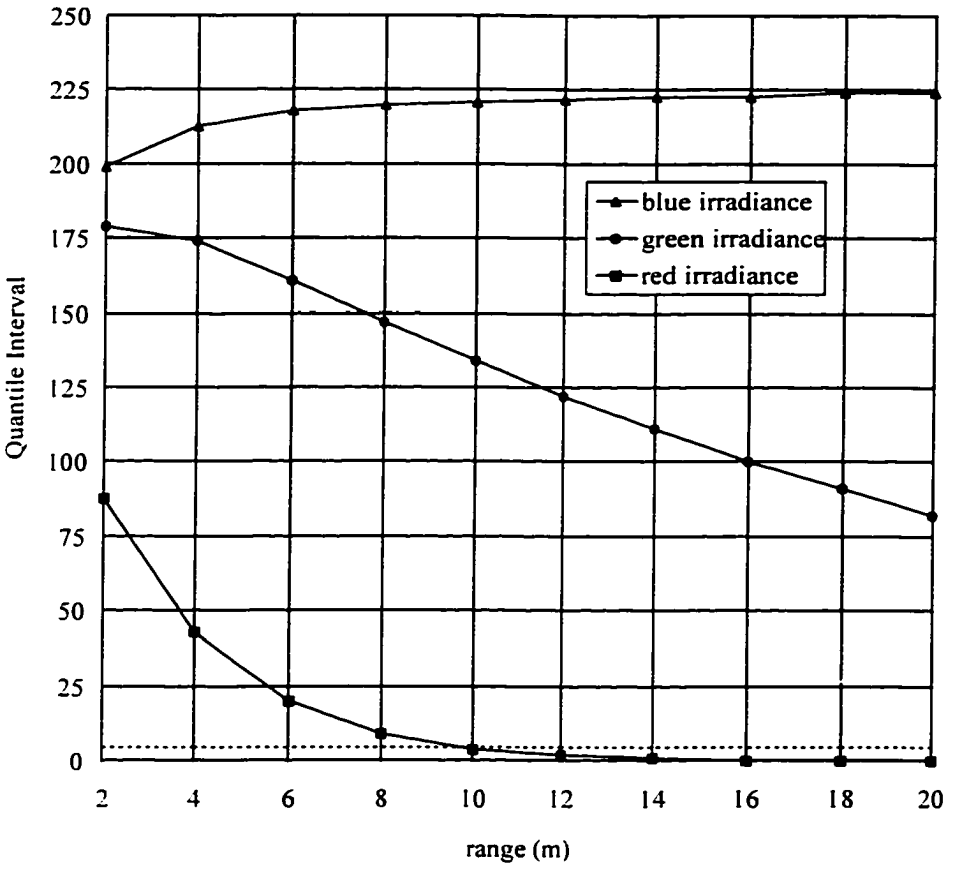

Figure 5.52: Mean irradiance levels as a function of range with B = 0.010

	SNR (dB)		
Range (m)	Red Channel	Green Channel	Blue Channel
2	3.85	4.47	4.56
6	2.58	4.38	4.65
10	1.16	4.22	4.65
14	-0.05	4.04	4.65
20	- inf	3.79	4.66

Table 5.1: Channel SNR as a function of range

Figure 5.53 plots rms estimation error as a function of range with 8 bit quantization, B=0.010 and noise as described previously. No smoothing or averaging is used. At

ranges of 5 m and less, range estimation using the blue and green channels exhibit the greatest sensitivity to noise. This is due to the small difference in the blue and green attenuation coefficients ($\Delta c = 0.050$). At 6 m and beyond the red irradiance drops to a level where the combined noise floor and quantization noise begin introducing significant estimation errors using red channel data . Range estimates using blue and green channel data maintain an rms error below 20 cm.

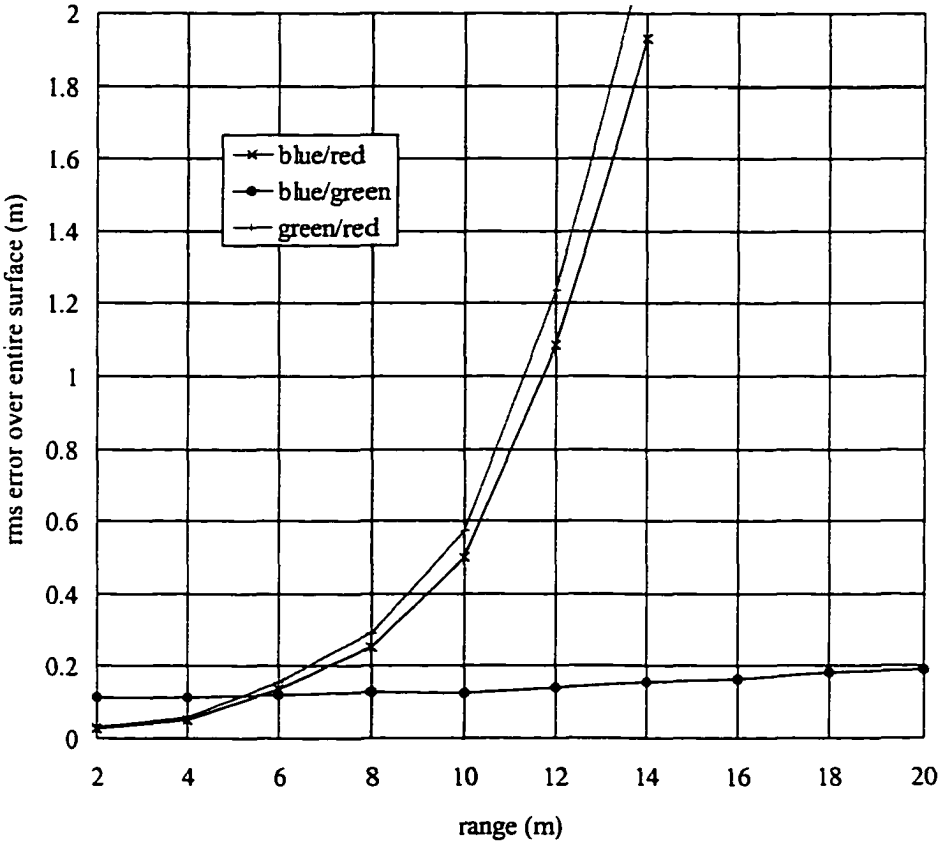

Figure 5.53: Range estimation error with 8 bit quantization and additional noise as in Fig. 5.51

Digitizing received irradiance to 16 bits and adding noise with the density function in Figure 5.54 yields the results plotted in Figures 5.55 and 5.56. As before, at the near ranges with reasonable SNR for all channels, ranges computed from irradiance data with the greatest differences in attenuation coefficients yield the most accurate results with rms error less than 7 cm for ranges up to 6 m. Further increase in range, hence decrease in received irradiance from the red channel again results in rapid increases in error from computations exploiting red channel data. Also in Figures 5.55 and 5.56 are the results obtained by smoothing the estimated range map with a 3×3 neighborhood averaging filter. The improvement realized by this simple and efficient technique is substantial – demonstrating up to a 50% reduction in estimation error. With neighborhood averaging, rms error using blue and green channel data remained below 10 cm out to a range of 20 m with a forward scattering of B = 0.010.

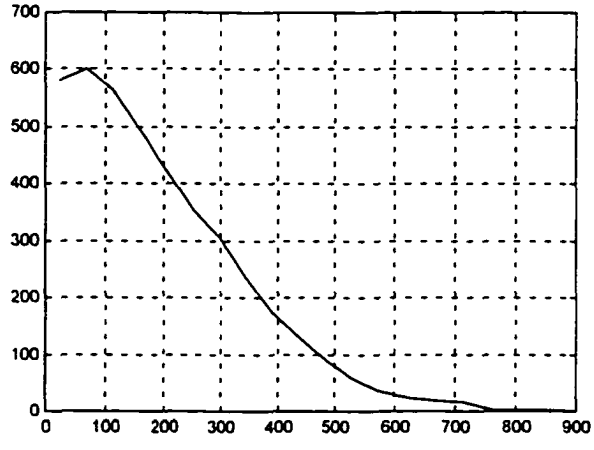

Figure 5.54: Noise distribution for the 16 bit quantization; mean = 198

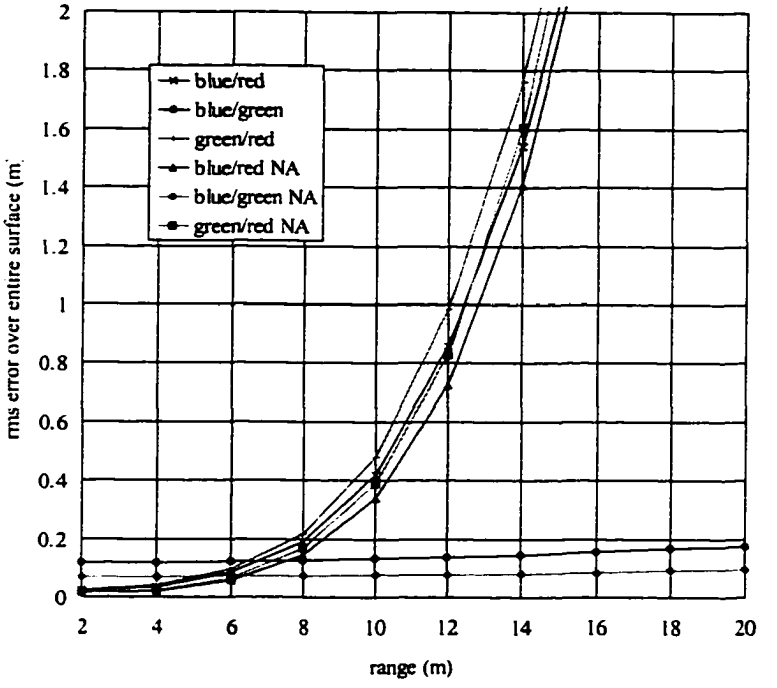

Figure 5.55: Range estimation error with 16 bit quantization and noise as in Fig. 5.54

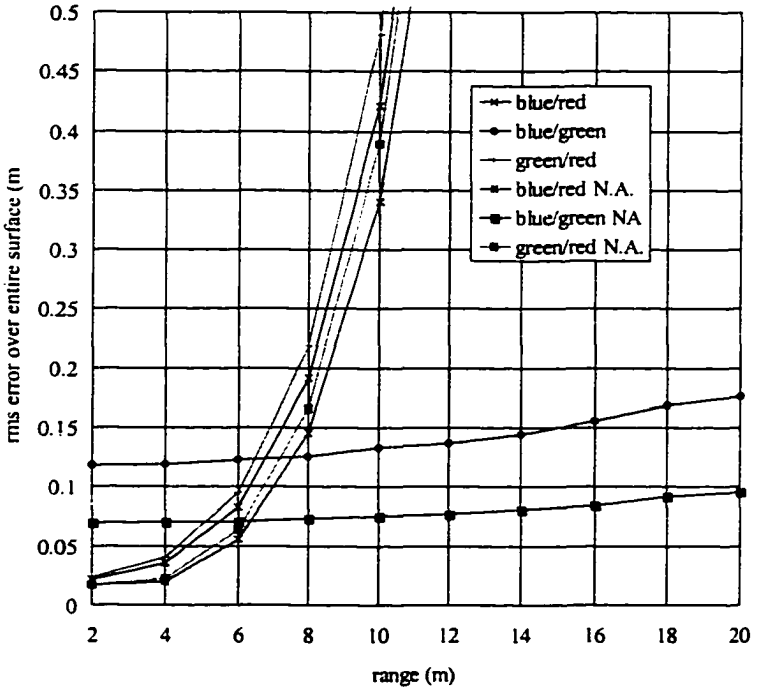

Figure 5.56: Figure 5.55 with expanded ordinate

To represent components of CCD camera noise that are proportional to received irradiance, the density function of the camera dark noise was changed as plotted in Figure 5.57 and zero mean Gaussian noise with a variance proportional to received irradiance level was added to each channel. Figures 5.58 to 5.61 plot the density function of received irradiances (Part (a)) and the density function of subsequent range estimates (Part (b)) at 2, 6, 12, and 20 m. To avoid skewing the density functions, these data are for a scene with a surface curved to maintain a constant range. RMS error as a function of range is plotted in Figure 5.62.

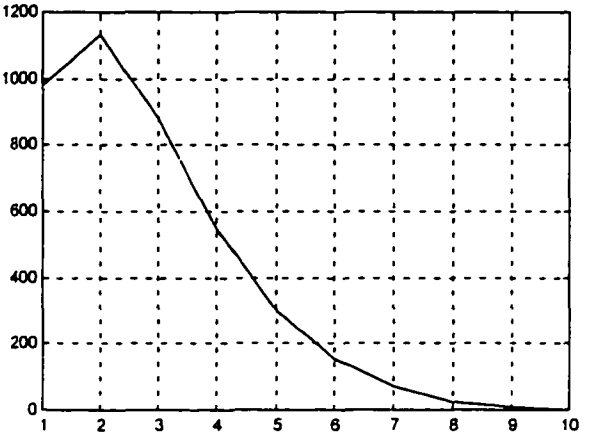

Figure 5.57: Noise distribution for reduced noise floor

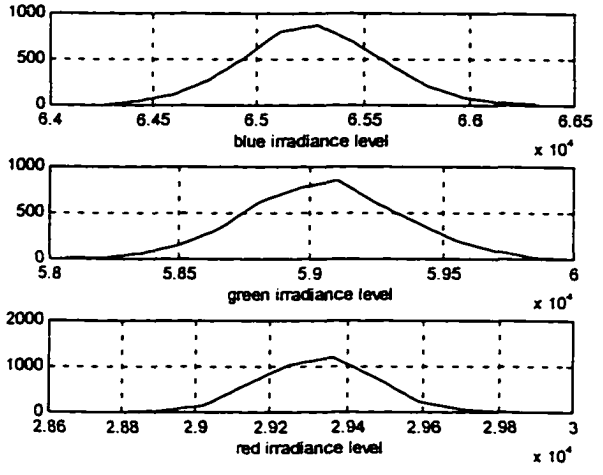

(a)

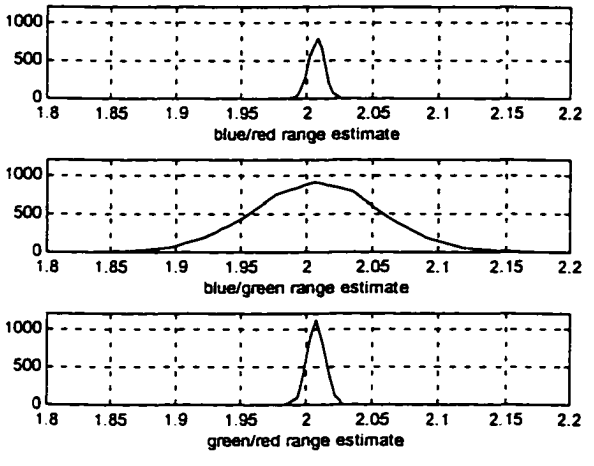

(b)

Figure 5.58: Irradiance and estimate density functions for a range of 2 m;

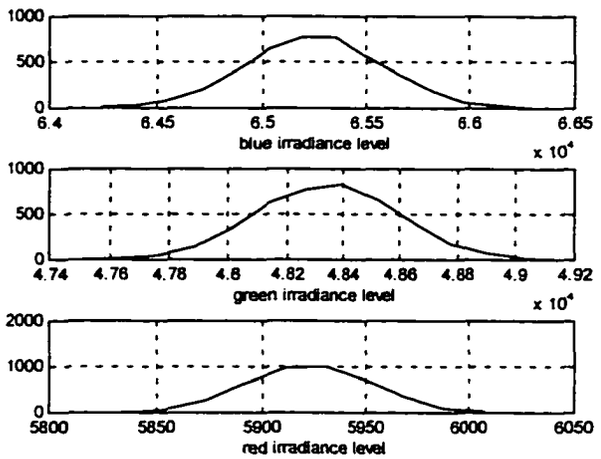

(a)

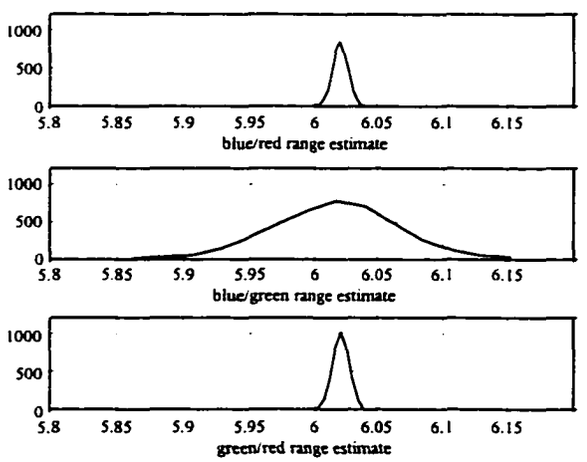

(b)

Figure 5.59: Irradiance and estimate density functions for a range of 6 m;

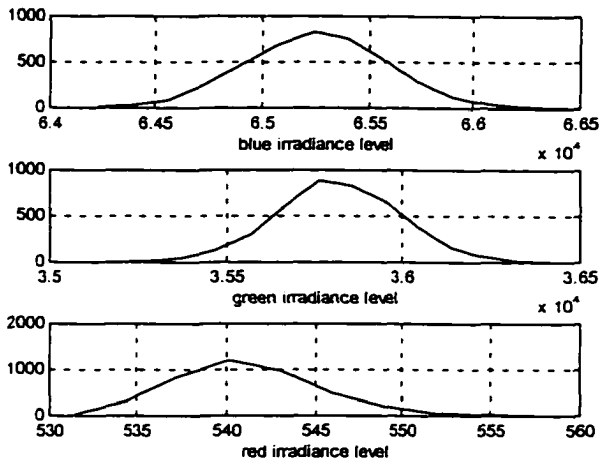

(a)

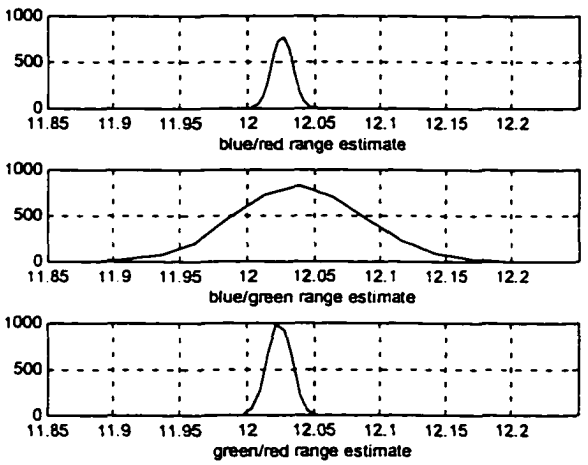

(b)

Figure 5.60: Irradiance and estimate density functions for a range of 12 m;

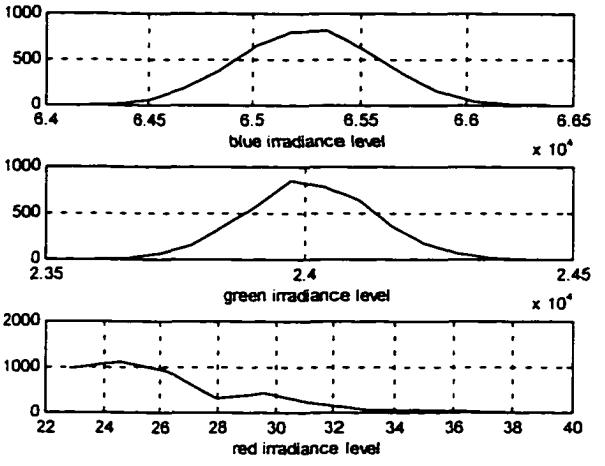

(a)

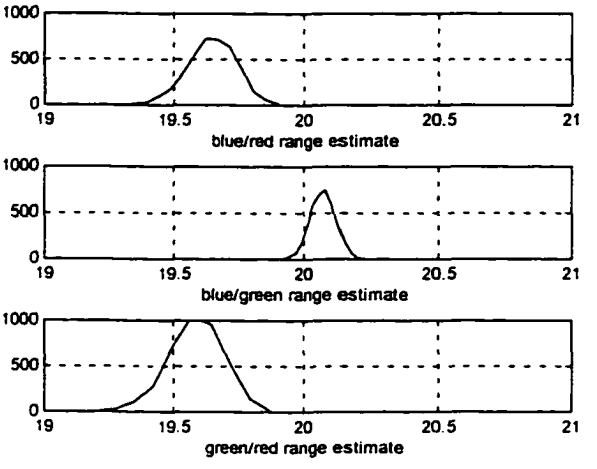

(b)

Figure 5.61: Irradiance and estimate density functions for a range of 20 m;

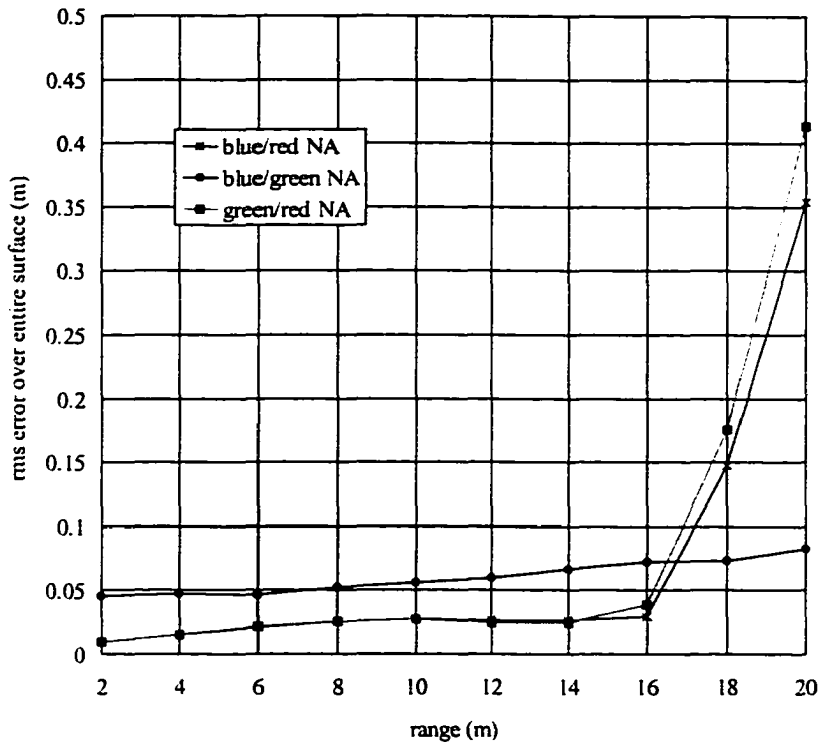

Figure 5.62: RMS error vs. range for equi-distant surface

The previous test was repeated with the scene containing the brick extending 0.10 m above the seabed. Mean SNR, plotted as a function of range for all three channels in Figure 5.63, is relatively consistent for ranges out to 8 m. Beyond this range red channel SNR begins dropping off.

Figure 5.64 plots estimate rms error versus range. Out to 16 m, estimate error increases very gradually as a function of range and estimates exploiting blue and green channel data have a higher error (though always below 0.10 m) than the green/red and blue/red estimates. The latter benefiting from a larger attenuation coefficient difference. At 16 m, with red channel SNR below 3 dB, estimate error using green and red channel data shows signs of increased rate of change. Beyond 16 m, error with estimates using red channel data increases exponentially with range. RMS error for estimates using blue and green channel data remains low and reaches a maximum of 0.0901 m at 20 m range.

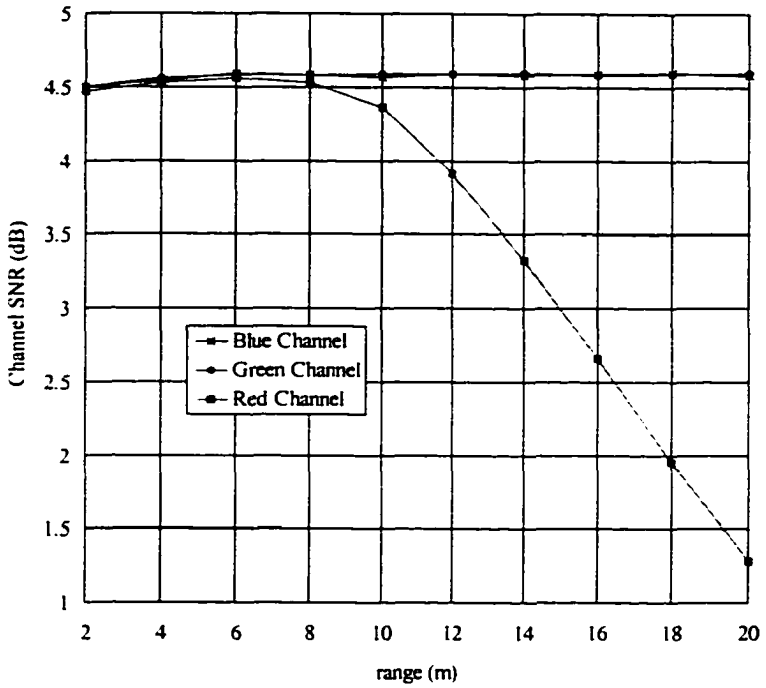

Figure 5.63: SNR vs. range for the blue, green, and red channels

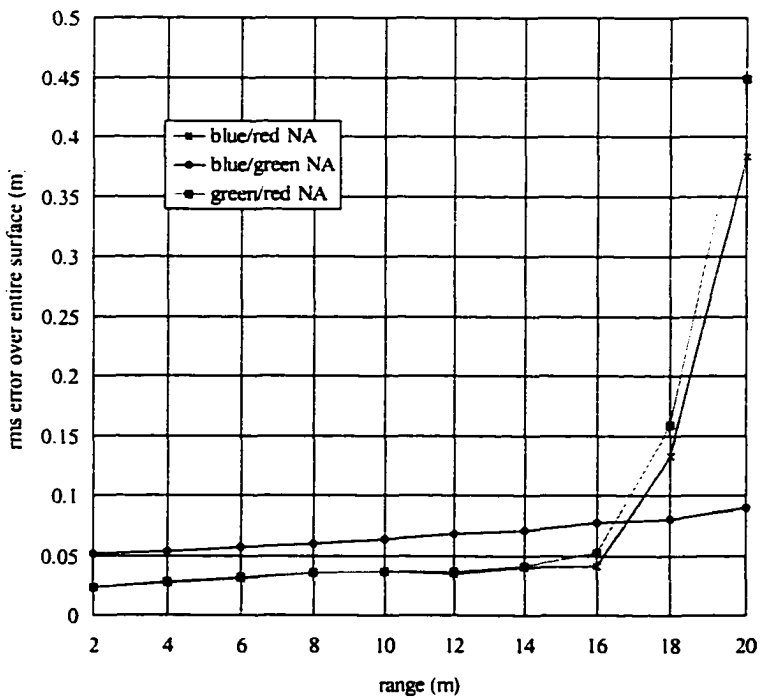

Figure 5.64: RMS error vs. range for scene with brick

Figures 5.65 to 5.67 are plots of range maps computed with the intensity range transformation using the data represented in the previous Figures 5.63 and 5.64. As in Figures 5.58 to 5.61 the mean estimate is biased up to 0.04 m by the effects of scattering and the non-zero-mean dark noise. Figure 5.65 is the range map at 2 m and the brick can easily be seen protruding above the seabed. In Figure 5.66, the range map at 8 m, an obstacle can still be seen protruding above the seabed but is poorly defined. At 18 m (Figure 5.67) the combined effects of scattering and noise mask the brick but the intensity–range transformation still returns an estimate of overall surface range with an rms error of only 0.13 m or 0.72 % of range. This reduces to 0.08 m or 0.44 % for blue and green channel data.

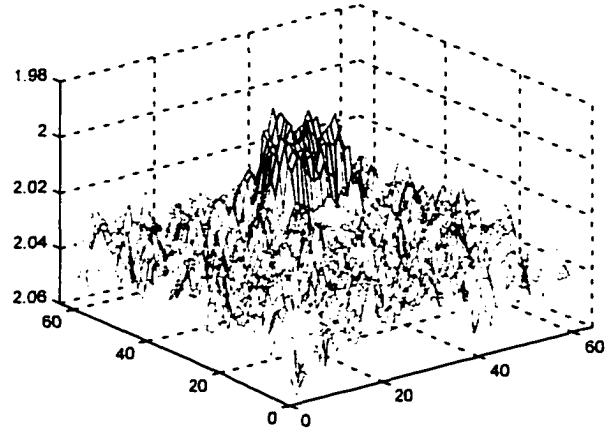

Figure 5.65: Range plot at 2 m; rms error = 0.024 m using blue and red channel data

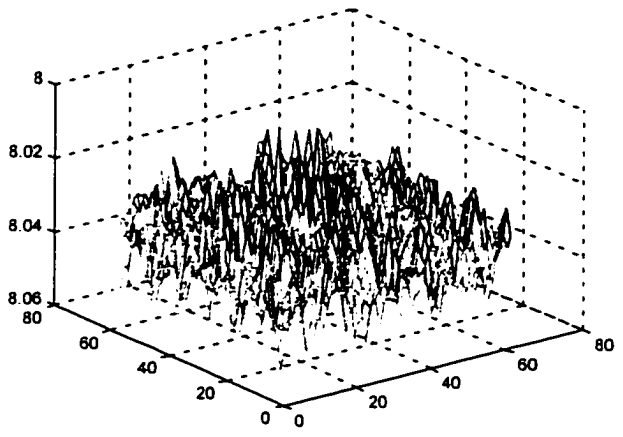

Figure 5.66: Range plot at 8 m; rms error = 0.035 m using blue and red channel data

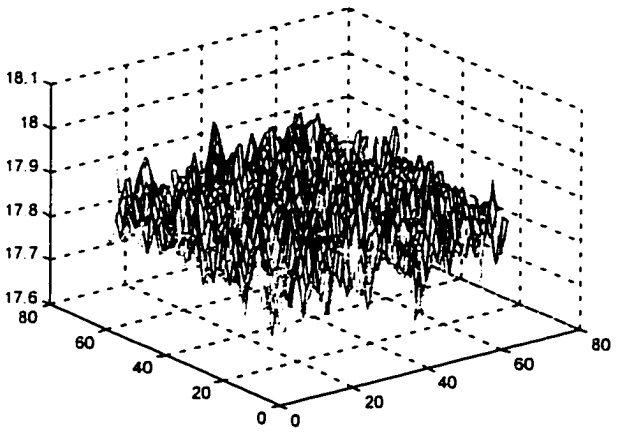

Figure 5.67: Range plot at 18 m; rms error = 0.133 m using blue and red channel data

Chapter 6

Conclusions

6.0 Introduction

This dissertation develops, analyzes, and presents the performance of an intensity–range transformation that exploits spectral irradiance differences to predict how far light has propagated underwater. This is, to the best of our knowledge, the first time the spectrally dependent nature of the attenuation of light in water has been used to facilitate underwater three dimensional machine vision. Presented in this Chapter are a summary of the results of this work and recommendations for future research.

6.1 Summary and Results of this Dissertation

In this dissertation, a novel technique for in-situ, underwater 3D machine vision is developed, a calibration procedure is derived, and overall performance is analyzed mathematically and through simulation. Results from actual underwater images are also presented.

Chapter 1 of this dissertation provides a review of underpinning and related work in the area of underwater light propagation and machine vision. It also discusses the novel approach and significance of the work herein. The intensity–range transformation is a technique that can be used in relatively low cost monocular vision systems to provide 3D

capability. It is computationally efficient, does not require mechanical scanning mechanisms, does not require structured or specialized lighting, and does not require contrasting features to be present in an image. Additional advantages and a number of potential applications are discussed in Chapter 1.

The work herein began from a "bottom-up" approach to underwater machine vision, studying first the optical properties of water. These properties were presented in Chapter 2; first the inherent optical properties based on propagation of a collimated beam, then in terms of apparent optical properties when non-collimated light and multi-order scattering are considered. For the latter it was found that one must rely on simulation techniques to study the propagation of light in water. Perhaps the most important fact presented in Chapter 2 in relation to this dissertation was that attenuation of light underwater, which is the combined effect of absorption and scattering, varies strongly as a function of light wavelength.

Chapters 3, 4, and 5 represent the main contributions of this dissertation. In Chapter 3 the spectrally dependent nature of light attenuation underwater was exploited to derive a transformation for determining how far light has propagated underwater based on relative irradiance levels in various spectral bands. A calibration technique was also developed so the transformation can be used in a practical underwater vision system. A numerical example illustrated that intensity images can be transformed into a range map with only two division operations, one multiplication, and a transcendental function call for each pixel. Chapter 3 concludes with range maps generated from actual images taken underwater, proving the utility of the intensity–range transformation.

Chapter 4 contains analytical analysis of the developed machine vision system. By studying the effects of noise on the distribution of range estimates, and the sensitivity of the system to calibration constants, further insight was gained into system implementation and performance. One parameter that may not be available from calibration is spectral

reflectivity of the surface being imaged. Various approaches to extracting that information with existing machine vision and other in situ sensing techniques were discussed. Based on the expression derived for estimate variance it is determined that maximum range accuracy is achieved by maximizing the difference in attenuation coefficients associated with spectral data used in the range estimate, and by using channels with the lowest valid signal variance. It can be expected that range estimates using different spectral channels will have different variances. The approach in this dissertation is to present a baseline performance of the vision system under a variety of conditions. Results are therefore presented using only two channels for each estimate and observing the accuracy and changes for different channel combinations. A short example is given to illustrate how multiple estimates can be combined by weighting the individual estimates on the basis of relative variance. Chapter 4 concludes with a technique suggested by Dr. R. L. Kirlin for extracting shape and range information. It is based on expanding the medium's transfer function about parameters of interest and using these terms in sensitivity vectors or objective functions. This technique inherently combines data from several channels.

Chapter 5 presents performance and results from the intensity–range transformation while systematically varying operating conditions. The results are too numerous to review individually but it should be noted that, in the author's opinion, an acceptable level of performance was realized. To study performance of the vision system in a scattering medium a simulator was coded in Matlab® based on a modelled formulated and validated by McGlamery et. al.. Chapter 5 begins with examples of the output from the simulator. Tests of the system in noise with no scattering were conducted and the results were consistent with analysis in Chapter 4. They illustrated that, for data with an SNR of 3 dB or more, rms error is on the order of 10^{-2} m. Results using Dr. Kirlin's technique illustrate

that it is also an effective technique for extracting both range data and other parameters such as surface orientation for each pixel.

Section 5.3 was dedicated to analyzing the intensity–range transformation in a scattering medium. It was found that for moderate scattering centimeter accuracies can be achieved to a range of 20 m. Another important result was that error due to scattering decreases significantly with decreased range below 1 m. This bodes well for using a suitable equipped vision system as a control sensor in underwater robotic operations.

6.2 Recommendations for Future Work

Developed in this dissertation is a new approach to underwater machine vision. The utility of the intensity–range transformation has been demonstrated and analyzed, and the work herein lays the foundation on which further development can build. This section gives recommendations for future work.

Future work that will be beneficial in enhancing the intensity–range transformation and associated developments fall into two categories: currently active research in related areas - the results of which may be exploited here; and research focused on furthering the work herein but which may be useful in other applications. Research in related areas that should be exploited include work on image segmentation, sensor fusion, and adaptive image processing. Optimal processing requires different filtering techniques for different types of images (or in this case surfaces). Adaptive processing of images formed underwater must also include an additional dimension – the effects of the medium itself. For example, additional blurring from averaging filters may not be so pronounced when the image is already being smoothed by the medium itself through scattering. This is a subject of current research in autonomous and semi-autonomous machine vision applications.

Another investigation that would aid practical implementation of the work in this dissertation is a quantifiable study of the variation in iceberg and sea ice colour. As stated previously, it is generally accepted by experts in the field that iceberg colour does not vary significantly within a region but no published evidence was found to support this.

Recommendations for future work specific to the developments of this dissertation are as follows.

- Development of a spectrum management scheme to identify which spectral channels will provide the best range estimates. It has been shown that there is considerable variation in the accuracy of range estimates using data from different spectral channels, and that the channels which provide the best estimate in one case will not necessarily provide the best estimate as conditions change. Multiple estimates from a number of channels can be weighted and combined but, as seen in Chapter 5, some of these can detract from the optimal estimate. Autonomous operation would be greatly enhanced if a system were capable of analyzing the medium, the received irradiance, and the hardware, to select the optimal channels to be used in the transformation.
- Most of the present applications envisaged for a machine vision system using the developments in this dissertation are at depths below 25 m where ambient light will not be a significant concern. Closer to the surface, ambient solar irradiance may introduce range errors and techniques should be developed to mitigate this. Three approaches are suggested for further study: (i) polarization discrimination using polarizing lenses on the luminaire and the camera. This has been successfully used on underwater laser systems. (ii) subtracting the ambient irradiance received from the irradiance received with the luminaire turned on. (iii) model measured upwelling and downwelling irradiance and either subtract it from the received irradiance or include it in the transformation computation.

- Several techniques were presented to extract the required reflection coefficient information for the surface being modelled using information from complementary sensors. Operation may be enhanced if this information could be extracted directly from the irradiance data. A few techniques have been developed through the course of this work but are susceptible to noise and a more robust solution is required.
- An advantage of the vision system developed here is that it does not require uniform or structured lighting. It should also work with multiple light sources but this has yet to be proven.
- An algorithm should be developed for combining the intensity–range transformation and Kirlin's approach to yield optimal range and shape (surface patch orientation) estimates.
- Finally, new applications and configurations for the intensity–range transformation and associated developments should be identified. Interest has been expressed in using it for a number of applications as discussed in Chapter 1 and additional applications for the technology will be sought.

References

[1] Various, *The Polar Oceans and Their Role in Shaping the Global Environment*, Geophysical Monograph 85, American Geophysical Union, 1994

[2] Bellingham, J.G., "Capabilities of autonomous underwater vehicles", *Proc. Scientific and Environmental Data Collection with Autonomous Underwater Vehicles*, MIT Sea Grant College Report No. MITSG 92-2, Cambridge, MA, pp. 7 - 14, 1992.

[3] Doyle, P. "Subsea technology is vital for developing Hibernia - area fields", (quotes from oil industry executives) *The Evening Telegram*, p. 28, Dec. 4, 1994.

[4] Stevenson, P., "The potential of robotic systems in the seas and offshore (matching research effort to the offshore industry and science needs)", *Underwater Technology*, Vol. 21, No. 2, pp. 44 - 46, 1995.

[5] Marine System Engineering Lab, UNH, *Systems/Subsystems Investigation for a Multi-sensor Autonomous Underwater Vehicle Search System*, NAVEODTECHCEN Tech. Report No. TR-301, 1990.

[6] Stewart, W.K., *Multisensor Modeling Underwater with Uncertain Information*, Ph.D. Thesis, Woods Hole Oceanographic Institute, Massachusetts Intstitute of Technology, 172 pp, 1988.

[7] Freeman, H. ed. "The state-of-the-art in real-time range mapping - a panel discussion", *Machine Vision for Three Dimensional Scenes*, Academic Press, 1990.

[8] Stewart, D.J., ""Conventional" underwater camera systems - the state of the art", *Underwater Systems Design International*, Vol. 17, No. 2, pp 5 - 9, 1995.

[9] Tusting, R.F. and F.M. Caimi, "Systems for improving the effectiveness of cameras on undersea vehicles", *Proc. ROV 85*, pp 25 - 31, 1985.

[10] Caimi, F.M., "A review of recent underwater imaging methods and advancements", *Proc. IEEE/MTS OCEANS 96*, 1996.

[11] Santos-Victor, J., & J. Sentiero, "The role of vision for underwater vehicles", *Proc. IEEE 1994 Symposium on Autonomous Underwater Vehicle Technology*, pp. 28 - 35, 1994.

[12] Trimble, G.M., J. Vilaro, D. Okamura, R. Lum & K. Dutta, "Underwater object recognition and automatic positioning to support dynamic classification", *Proc. Seventh Int. Symp. Unmanned Untethered Submersible Technology*, pp. 273 - 279, 1991.

[13] Negahdaripour, S., "Optical Sensing for Autonomous Subsea Vehicles", *Preception, Scene Reconstruction and World Modeling for Unmanned Underwater Vehicles*, MIT Sea Grant College Report No. MITSG 92-24, Cambridge, MA, 1993.

[14] Caimi, F.M. "Spatial coherence methods in undersea image formation and detection", *IEEE/MTS OCEANS '96*, supplement, 1996.

[15] Chantler, M.J.. "Optical and Acoustic Range Sensing for Underwater Robotics," *Proc. IEEE/MTS Oceans 94*, Vol. 1, pp205-210, 1994.

[16] Jerlov, N.G. *Optical Oceanography, Elssevier Oceanographic Series*, vol. 5, Elsevier Publishing Company, Amsterdam, London, New York; 1968.

[17] Williams, J., *Optical Properties of the Sea*, United States Navel Institute series in oceanography, United States Navel Institue, Annapolis, Maryland, 1970.

[18] Jerlov, N.G., *Marine Optics*, Elsevier Scientific Publishing Company, New York, 1976.

[19] Spinrad, R.W., K.L. Carder & M.J. Perry, *Ocean Optics*, Oxford Monographs on Geology and Geophysics No 25, Oxford University Press, New York, 1994.

[20] Mobley, C.D. *Light and Water; Radiative Transfer in Natural Waters*, Academic Press, 1994.

[21] James, H.R. & E.A. Birge, "A laboratory study of the absorption of light by lake waters," *Transactions Wisconsin Acadamy of Sciences*, No 31, 1938.

[22] Clerke, G.J. & H.R. James, "Laboratory analysis of the selective absorbtion of light by sea water," *Journal of the Optical Society of America*, No 29, 1939.

[23] Jerlov, N.G., "Optical Classification of Ocean Water" in *Physical Aspects of Light in the Sea*, J. E. Tyler, ed., University of Hawaii Press, pp. 45 - 49, 1964.

[24] Duntley, S.Q.. "Light in the sea" *Journal of the Optical Society of America*, Vol 53, pp 214-233, February 1963.

[25] Blizard, M.A. "Ocean optics: Introduction and overview," *Ocean Optics VIII, Proceedings of SPIE*, April 1986.

[26] Gordon, H.R, "Practical approaches to underwater multiple-scattering problems" *Ocean Opticis*, SPIE Vol. 64, pp 85 - 93, 1975.

[27] Preisendorfer, R.W. *Hydrologic Optics vol. 1: Introduction*, National Technical Information Service NTIS PB-259 793/8ST, Springfield, Ill, 1976.

[28] Zaneveld, J.R.V., "Optical closure: From theory to measurement," *Ocean Optics*, Oxford Monographs on Geology and Geophysics No 25, Spinrad, R.W., K.L. Carder & M.J. Perry, eds., Oxford University Press, New York, 1994.

[29] Mertens, L.E., *In Water Photography Theory and Practice*, Wiley-Interscience, New York, N.Y., 1970.

[30] Gordon, H.R, "Modeling and simulation of radiative transfer in the ocean," *Ocean Optics*, Oxford Monographs on Geology and Geophysics No 25, Spinrad, R.W., K.L. Carder & M.J. Perry, eds., Oxford University Press, New York, 1994.

[31] Duntley, S.Q.. *Underwater Lighting by Submerged Lasers and Incandescent Sources*, SIO Ref. 71-1, Scripps Institute of Oceanography, San Diego, Ca, June 1971.

[32] Chilton, F., D.D. Jones & W.K. Talley, "Imaging properties of light scattered by the sea", *Jour. Opt. Soc. Amer.*, Vol. 59, No. 8, pp 891 -898, August 1969.

[33] Wells, W.H. "Loss of resolution in water as a result of multiple small-angle scattering" *Jour. Opt. Soc. Amer.*, Vol. 59, No. 6, pp 686 -691, June 1969.

[34] Yura, H.T. "Small-angle scattering of light by ocean water", *Applied Optics*, Vol. 10, 1971.

[35] Arnush, D., "Underwater light-beam propagation in the small-angle scattering approximation", *Jour. Opt. Soc. Amer.*, Vol. 62, pp 1109 -1116, June 1972.

[36] Del Grosso, V.A., "Modulation transfer function of water", *Ocean Opticis*, SPIE Vol. 64, pp 34 - 49, 1975.

[37] McGlamary, B.L. *Computer Analysis and Simulation of Underwater Camera System Performance*, SIO Ref. 75-2, Scripps Institute of Oceanography, San Diego, Ca, January 1975.

[38] McGlamary, B.L. "A computer model for Underwater Camera Systems", *Ocean Optics VI*, SPIE Vol. 208, pp 221 - 231, 1979.

[39] Jaffe, J.S., "Computer modeling and the design of optimal underwater imaging systems" *IEEE J. Oceanic Engineering*, Vol. 15, No. 2, pp 101 - 111, April 1990.

[40] Jaffe, J.S., S.E. Harris & R. Squires "A computer model for the prediction of underwater images" *Proc. ROV '85*, pp 12 - 15, 1985.

[41] Jaffe, J.S., *Underwater Imaging Systems Performance Characterization*, WHOI Ref. 88-33, Woods Hole Oceanographic Institue, Woods Hole, MA, August 1988.

[42] Jaffe, J.S., "Monte carlo modeling of underwater imaging formation: Validity of linear and small angle approximations", *Applied Optics*, Vol. 34 No. 24, pp 5413 - 5421, August 1995.

[43] Harries, S.E. & R.D. Ballard, "ARGO capabilities and deep ocean explorations", *Proc. IEEE OCEANS '86*, pp. 6 - 9, 1986.

[44] Palowitch, A.W. & J.S. Jaffe, "Computer model for predicting underwater color images", *Underwater Imaging, Photography, and Visibility*, SPIE 1537, pp 128 - 139, 1991.

[45] Angelbeck, A.W., "Application of a laser scanning and imaging system to underwater viewing," *Underwater Photo- Optics, Proceedings of SPIE*, October 1966.

[46] Caimi, F.M. & D.M Kocak "Laser/light imaging for underwater use", *Sea Technology*, pp. 22-27, December 1993.

[47]. Stewart, D. "Vision systems--industry comments", *International Underwater Systems Design*, Vol 6, No 2, April 1994

[48] Science Applications International Corp., "Laser line scanning system: TWA Flight 800", *IEEE/MTS Oceans 96 Video Proceedings*, 1996.

[49] Lenz, R. & U. Lenz, "New developments in high resolution acquisition with CCD area sensors", *Proc. SPIE 2252, Optical 3D Measurement techniques II: Applications in Inspection, Quality Control & Robotics*, pp. 53 - 62, 1993.

[50] Gilligan, L., "gated photocathode ICCD cameras for underwater imaging", *Advanced Imaging*, pp. 38 - 64, 1989.

[51] Yin, Z., S.X. Zhang, X.M. Guo & B.Q. Xi, "A pixel range gated imaging system for underwater viewing and range finding", *IEEE 1990 Symposium on Autonomous Underwater Vehicle Technology*, pp. 280 - 285, 1990.

[52] Anon., *Underwater Imaging Using a Laser-Illuminated Range-Gated Iccd Camera System.* Technical Briefing, SPARTA Laser Systems Laboratory, San Diego, CA, 1994.

[53] Swartz, Barry, SPARTA Laser Systems Laboratory,Personnal communication, 1994.

[54] Swartz, B., & J.D. Cummings, "Laser range gated underwater imaging including polarization discrimination", *Underwater Imaging, Photography, and Visibility,* SPIE 1537, pp 42 - 56, 1991.

[55] Blatt, J.H., S.C. Cahall, B. Gilbert, J.A. Hooker, & G.L. Wallace, "Generation of surface shape from variable resolution video Moiré contours", *Proc. SPIE: Industrial Applications of Optical Inspection, Metrology, and Sensing,* Vol. 1821, pp. 304 - 311, 1992.

[56] Hans-Gerd, M., "Automated photogrammetric surface reconstruction with structured light", *Industrial Vision Metrology,* SPIE 1526, pp 70 - 77, 1991.

[57] Swanson, N.L. & D. Van Winkle, "Tempoal coherence loss due to dynamic scattering of laser light", *Proc. IEEE OCEANS '93*, Vol. III, pp. 171 - 175, 1993.

[58] Swanson, N.L., "Coherence loss of laser light propagated through simulated coastal waters", *Proc. Ocean Optics XI*, pp. 1750 - 1755, 1992.

[59] Pien, H.H., & D.E. Gustafson, "An AUV vision system for target detection and precise positioning", *Proc. IEEE 1994 Symposium on Autonomous Underwater Vehicle Technology*, pp. 36 - 43, 1994.

[60] Amat, V., "Vision Based Underwater Robot Stabilization", *Proc. IARP Workshop on Mobile Robots for Subsea Environments*, 1994.

[61] Marks, R., M. Lee & S. Rock, "Using visual sensing for control of an underwater robotic vehicle", *Proc. IARP Workshop on Mobile Robots for Subsea Environments*, 1994.

[62] Smith, J. & J. Lucas, "The sensing and control systems of a demonstrator underwater vehicle", ", *Proc. IARP Workshop on Mobile Robots for Subsea Environments*, 1994.

[63] Lagstad, P., "Detecting Linear Motion of an Object in a Sequence of Monocular Underwater Images", *Proc. IEEE 1996 Symposium on Autonomous Underwater Vehicle Technology*, pp. 343 - 353, 1996.

[64] Marks, S., H.H. Wang, S.M. Rock, & M. Lee, "Automativ visual station keeping of an underwater robotic vehicle", *Proc. IEEE OCEANS '94*, Vol. II, pp. 137 - 142, 1994.

[65] Volden, R. & J.G. Volden, "Determining 3-D object coordinates from a sequence of 2-D images", *Proc. Eigth Int. Symp. Unmanned Untethered Submersible Technology*, pp. 359 - 369, 1993.

[66] Smith, J.S., R. Yu, I. Sarafis, & J. Lucas, "Computer vision control of an underwater manipulator", *Proc. IEEE/MTS OCEANS '94*, Vol. I, pp. 187 - 192, 1994.

[67] Fairweather, A.J.R, A. Greig, & A. Allnut, "Object recognition and machine vision to enhance scene interpretation in an underwater application", *Proc. IEEE OCEANS '95*, pp. 1865 - 1870, 1995.

[68] Stewart, D.J., Simrad Osprey Ltd., Personnel Communication, 1994.

[69] Tusting, R.F., F.M. Caimi & L.D. Taylor, "Special-purpose illumination systems for remotely operated vehicles," *Proc ROV '89*, pp 170-175, 1989.

[70] Yu, C.H., *Underwater machine vision: Recovering orientation and motion of Lambertian planar surfaces in light attenuating media*, Ph.D. Thesis, University of Hawaii, 130 pp, 1990.

[71] Negahdaripour, S., C.H. Yu & A. Shokrollahi, "Recovering shape and motion from undersea images," *IEEE Journal of Oceanic Engineering*, Vol 15, No 3, pp 189-198, 1990.

[72] Yu, C.H. & S. Negahdaripour, "Orientation and distance recovery of Lambertian planar surfaces in light-attenuating media from optical images," *Journal of the Optical Society of America*, Vol 8, No 1, pp 217-228, 1991.

[73] Yu, C.H. & S. Negahdaripour, "Motion recovery in light-attenuating media from image shading variations," *Journal of the Optical Society of America*, Vol 9, No 7, 1992.

[74] Yu, C.H. & S. Negahdaripour, "Underwater experiments for orientation and motion recovery from video images," *Proc. IEEE Robotics and Automation Conf*, pp 93-98, 1993.

[75] Yu, C.H. & F. Caimi, "Determinations of Horizontal Motion Through Optical Flow Computations", *Proc. IEEE OCEANS '93*, Vol. II, pp. 475 - 480, 1993.

[76] Negahdaripour, S., & C.H. Yu, "A generalized brightness change model for computing optical flow", *Proc. Fourth ICCV*, Berlin, Germany, May 1003.

[77] Yu, C.H. & C. Wang, "Shape from underwater image shading," *Proc. Oceans '94*, Vol 1, pp 181-186, 1994

[78] Paschos, G., "Color and Texture Based Image Analysis: Segmentation and Classification", *PhD Thesis*, University of Southwestern Louisiana, Spring 1996.

[79] Bierwirth, P.N., T.J. Lee, and R.V. Burne, "Shallow sea-floor reflectance and water depth derived by unmixing multispectral imagery", *Photogrammetric Engineering & Remote Sensing*, Vol. 59, No. 3, pp. 331-338, March 1993.

[80] Lyzenga, D.R. "Passive remote sensing techniques for mapping water depth and bottom features", *Applied Optics*, Vol. 17, No. 3, pp. 379-383, February 1978.

[81] Lyzenga, D.R. "Remote sensing of bottom reflectance and water attenuation parameters in shallow water using aircraft and Landsat data", *Int. J. Remote Sensing*, Vol. 2, No. 1, pp. 71-82, February 1981.

[82] Tassan, S., "Modified Lyzenga's method for microalgae detection in water with non-uniform composition", *Int. J. Remote Sensing*, Vol. 17, No. 8, pp. 1601-1607, 1996.

[83] Jupp, D.L.B., "Background and extensions to depth of penetration (DOP) mapping in shallow coastal water", *Symposium on Remote Sensing of the Coastal Zone*, Queensland, AU. Session 4, Paper 2, 1988.

[84] Nordman, M.E., L. Wood, J.L. Michalek, & J.J. Christy, "Water depth extraction from Landsat-5 imagery", *Proc. 23rd Int. Symposium on Rem. Sensing of the Environment*, pp. 1129-1139, 1990.

[85] Paschos, G., & K.P. Valavanis, "A color texture based visual monitoring system for automated surveillance", *Proc. IEEE 1996 Symposium on Autonomous Underwater Vehicle Technology*, pp. 354 - 361, 1996.

[86] Anon., *SM2000 sales information*, Westinghouse Underwater Light and Laser Division, 1995.

[87] Carder, K.L. (co-author of [19]), personal communication, 1994.

[88] Lever, J., *Subsea Options for Canada's East Coast*, Presented at NOIA Conference on Offshore Technology, 1995.

[89] Personnel Communication with a President and two VPs Frontier Development from three major Canadian oil companies, August & October 1996.

[90] Kirlin, R.L., "Estimation of Transfer Function Parameters Using Fourier Transform Sensitivity Vectors", personal communication and submission to *IEEE Intl. Conf. Acoustics Speech and Signal Processing; ICASSP 97*, Munich, April, 1997.

[91] Hulbert, E.O., "Optics of distilled and natural water", *Journal of the Optical Society of America*, Vol 35, No. 11, pp 698-705, Nov. 1945.

[92] Matlack, D., *The Deep Ocean Optical Measurement (DOOM) Project*, Navel Ordnance Laboratory, NOLTR 70-165, 1971.

[93] Jerlov, N.G., *Reports of the Swedish Deep Sea Expedition of 1947-48.* vol. 3, p49, 1951.

[94] Shannon, J.G., "Correlation of beam and difuse attenuation coefficients measured in selected ocean waters", SPIE Vol. 64, Ocean Optics, pp. 3 - 11, 1975.

[95] Baker, K.S., and R.C. Smith, "Quazi-inherent characteristics of the diffuse attenuation coefficient for irradiance," Ocean Optics VI, ed. S.Q. Duntley, Proc. SPIE vol. 208, 1979.

[96] Austin, R.W. and T.J. Petzold, "Spectral dependence of the diffuse attenuation coefficient of light in ocean water", Opt. Eng. vol.25, no. 3, 1986.

[97] Spinrad, R.W., J.R.V. Zaneveld and H. Pak, "Volume scattering function of suspended particulate matter at or near-forward angles: a comparison of experimental and theoretical values", Appl. Opt. vol. 17, no. 7, pp. 1125-1130, 1978.

[98] Oppenheim, A., and R. Schafer, *Digital Signal Processing*, Prentice Hall, 1975.

[99] Healey, G., & R. Kondepudy, "Modeling and calibrating CCD cameras for illumination insensitive machine vision," *Optics, Illumination, and Image Sensing for Machine Vision VI, SPIE* Vol. 1614, pp 121-132, 1991.

[100] Peebles, P.Z. *Probability, Random Variables and Random Signal Principles, 2nd ed.*, McGraw-Hill Book Company, 1980.

[101] Larson, H.J. & B.O. Shubert, *Probabilistic Models in Engineering Sciences, Volume I: Random Variables and Stochastic Processes*, John Wiley & Sons Inc., New York Chichester Brisbane Toronto, 1979.

[102] Hogg, R.V, & J. Ledolter, *Engineering Satatistics*, Macmillan Publishing Company, New York, 1987.

[103] Tusting, R.F., "Systems for improving the effectiveness of cameras on undersea vehicles," Proc ROV '85, pp 25-31, 1985.

[104] Trusting, R.F., & F.M. Caimi, "Special-purpose illumination systems for remotely operated vehicles," Proc ROV '89, pp 170-175, 1989.

[105] Negahdaripour, S. & C.H. Yu, "On shape and range recovery from image shading for underwater applications," Book Chapter in *Underwater Robotic Vehicles: Design and control*, J. Yuh (Ed.), TSI Press, Albuquerque, NM, 1995.

[106] Negahdaripour, S., personnel communication, 1995 and 1996.

[107] Reid, C, *Integration of Acoustic and Visual data for Subsea Robotics*, Ph.D. Thesis, Herriot-Watt University, 130 pp, 1990.

[108] Austin, R.W., & T.J. Petzold, "An instrument for the measurement of spectral attenuation coefficient and narrow angle volume scattering function of odean waters," *Ocean Optics, SPIE* Vol. 64, pp 50 - 61, 1975.

[109] Yin, Z., S.X. Zhang, X.M. Guo, Y.J. Zhu, & B.Q. Xi, "A pixel range gated imaging system for underwater viewing and range finding," *Proc AUV 90*, pp 280 - 285, 1990.

[110] Gordon, A., "Use of a laser scanning system on mobile underwater platforms," *Proc AUV 92*, pp 202 - 205, 1992.

Appendix A

Table of Abbreviations

C.I.E.	Commission Internationale de L'Ecairage
CCD	charge coupled device
ICCD	intensified charge coupled device
IOP	inherent optical properties
lhs	left-hand side
LSS	line scanning systemr
MSS	multispectral scanner
MTF	modulation transfer function
pdf	probability density function
PSF	point spread function
RGB	Red, Green, Blue
rhs	right hand side
SNR	signal to noise ratio
UUV	unmanned underwater vehicle
wrt	with respect to